Dynamics and Stability of Passive Dynamic Biped Walking Using an Advanced Mathematical Model

by

Derek Koop

A Thesis submitted to the Faculty of Graduate Studies of
The University of Manitoba
in partial fulfilment of the requirements of the degree of

MASTER OF SCIENCE

Department of Mechanical and Manufacturing Engineering
University of Manitoba
Winnipeg

Abstract

Passive dynamic walking is a manner of walking developed, partially or in whole, by the energy provided by gravity. Studying passive dynamic walking provides insight into human walking and is an invaluable tool for designing energy efficient biped robots. The objective of this research was to develop a new mathematical model of passive dynamic walking that modeled the ground reaction forces. A physical passive walker was built to validate the proposed mathematical model. The stability of the gait was analyzed using the proposed model. A novel method was created to determine the stability region of the model. Using the insights gained from the stability analysis, the relation between the angular momentum and the stability of the gait was examined. The proposed model matched the gait of the physical passive walker exceptionally well, both in trend and magnitude. The angular momentum of the passive walker was not found to correlate to the stability of the gait.

Acknowledgements

I would not have been able to complete the research presented in this thesis without the help of those around me. Dr. Christine Wu, my supervisor, has provided much more than guidance throughout my time with her. She has helped me develop my understanding of how research is completed and how to develop, analyze, evaluate, and interpret ideas. Without her encouragement and enthusiasm through my undergraduate degree I would not have continued onto graduate studies, for that I am sure of. I am indebted to her for the fantastic four years I have had working for her.

I am grateful for those who helped me with setting up and building my experiments. I would like to thank the machinists, Dan and Irwin, for helping me refine my design of the passive walker, HM2L, and for building HM2L. Darrel Koop ordered the ramp materials and got them delivered (and unknowingly lent me tools to build the ramp), for which I am very appreciative. Also, I would like to thank Ehsan Jalayeri for ordering equipment and helping me solve problems with the data acquisition system.

To my colleagues in the lab and in the mechanical engineering department, I am grateful for your help when I needed a second pair of hands or another point of view. I am appreciative of the proof reading by Whitney Reid to make sure it is not too technical. Finally, to my family and friends, thank you for listening to me talk about passive dynamic walking for the past four years.

Contents

List of Tables

List of Figures

Nomenclature

Greek Alphabet

α	–	The angle between the two legs
α_0	–	The minimum inner leg angle before double support
γ	–	The angle of inclination of the ramp
δ	–	The angle that describes the foot center offset
ε	–	The adjustment to the offset for the basin of attraction
θ	–	Angle of the leg of the passive walker with respsect to the normal of the ramp surface
μ_c	–	The Coulomb friction coefficient (Also known as the kinetic friction coefficient)
μ_s	–	The static friction coefficient
ρ	–	The foot radius of the passive dynamic walker

English Alphabet

b	–	The distance from the hip to the center of mass of the leg
c	–	The point on the foot with the lowest y coordinate
F_f	–	Friction force
F_N	–	Normal force
g	–	The acceleration due to gravity
$g_i(v)$	–	Function in the LuGre model
h	–	Inter–penetration of the two surface in the Hunt-Crossly contact model
k_d	–	Contact damping
k_s	–	Contact stiffness
k_v	–	Absolute value approximation term
L	–	Lagrangian
L_{step}	–	Step length
l	–	Length of the leg of the walker
M	–	Hip mass
m	–	Leg mass
N_i	–	Normal force level
n, p, q	–	Hunt-Crossly contact parameters
Q	–	The states of the state-space model
q	–	Generic term for the states of the mathematical model
r_g	–	Radius of gyration of the leg with respect to the center of mass
S_v	–	Approximation to the absolute value
T	–	Kinetic energy
T_{step}	–	Step period
V	–	Potential energy
v	–	Sliding velocity between two surfaces
$\bar{v}_{hip}$	–	Average hip velocity over one step
v_s	–	Stribeck velocity

w	–	Width of the physical walker
x_{hip}	–	Position of the hip of the walker along the ramp
y_{hip}	–	Position of the hip of the walker normal from the ramp
z_i	–	Bristle deflection in the LuGre model

Subscripts

i	–	Identifies which leg
ld	–	Refers to the lead leg
tr	–	Refers to the trail leg
st	–	Refers to the stance leg
sw	–	Refers to the swing leg
x	–	The x coordinate of a value
y	–	The y coordinate of a value

Superscripts

0	–	Identifies the step prior to the current
1	–	Identifies the current step
$+$	–	After impact
$-$	–	Before impact
$*$	–	Equilibrium point or adjusted offset for the BoA
hip	–	Position with respect to the hip

Acronyms

BoA	–	Basin of Attraction
CoM	–	Center of Mass
CMP	–	Centroidal Moment Pivot
DAE	–	Dynamic Algebraic Equation
DS	–	Double Support
FRI	–	Foot Rotation Indicator
FZMP	–	Fictitious Zero Moment Point
HM2L	–	Hip Mass Two Link (Experimental Walker)
LCE	–	Lyapunov Characteristic Exponent
ODE	–	Ordinary Differential Equation
POI	–	Point of Interest
PWM	–	Pulse Width Modulation
SL	–	Stance Leg
ZMP	–	Zero Moment Point

Chapter 1

Introduction

1.1 Motivation

What is passive dynamic biped walking and what is gained by studying passive dynamic biped walking? Passive dynamic biped walking is a manner of walking that utilizes the momentum and potential energy of the legs and body to continue the gait. The knowledge gained from studying passive dynamic biped walking can be useful in two main areas: the development of humanoid robotics and understanding the human gait. The two main goals for producing a biped robot gait are energy efficiency and postural balance (or dynamic balance). Fully passive dynamic biped walkers are very energy efficient, using only the energy provided by gravity to walk down a shallow slope. However, passive dynamic biped walkers are inherently unstable. Understanding what effects the robustness of a passive walker may provide insights on how to control biped robots to maintain postural balance while maintaining an energy efficient gait. Humans use the gravitational potential energy of the body to help develop their gait along with their muscle energy. This type of gait is often referred to as a semi-passive dynamic gait. Understanding how the mechanics of the legs shape the gait can provide insight into how humans develop their gait.

1.2 Background

This section covers a background on the history of passive dynamic walking and current research in the field. As well, an overview of different contact models and friction models for the purpose of dynamic modeling are provided.

1.2.1 Passive Dynamic Walking

Studying anthropomorphic passive dynamic walking machines started in the 1980s with Tad McGeer who was inspired by earlier research completed by Mochon and McMahon [1]. McGeer examined the passive gait through the use of mathematical models and experimental walking machines [2][3]. McGeer's initial researched stimulated an interest in passive dynamic walking. Two notable papers that followed are one by Garcia et al. [4] and the other by Goswami et al. [5], where the effects of the passive walker parameters on the gait and the stability of a passive walker were studied. Research on passive dynamic walking has taken two main forms, experimental studies and analysis through mathematical modeling, with a majority belonging to the latter.

Mathematical modeling is an excellent tool for analyzing passive dynamic walking. A number of passive dynamic walking models have been developed [2][5][6]. However these models are discontinuous. At the heel strike event, another set of equations are used described the impact event. A majority of impact-based passive walking models rely on the assumptions that the heel strike impacts are plastic and no sliding occurs during impact. These assumptions may create artificial gaits that are not representative of reality. A mathematical model with discontinuities is also limited to analysis methods that apply to non-smooth systems or special consideration is needed to apply smooth system analysis methods. In the aforementioned mathematical models, [2] [5][6], the stance foot is assumed to be in pure rolling with the friction between the foot and the ground modeled using basic friction models or neglected all together. The friction between the ground contact can change the resulting gait noticeably and reduces the likelihood of producing artificial gaits [2]. More recently passive walking models that use force–based contact models to describe the ground reaction forces have been developed. A more complex passive walking model is presented in [7] and [8] that uses the Hunt-Crossley contact model. In [7], the effects of the contact model parameters on the gait are examined. In [8], the effects of compliance in the passive walker structure is studied.

To determine if assumptions used to derive a passive dynamic walking model are valid, the model must be compared against a physical passive walker. In McGeer's initial work [2] a comparison between simulations of passive walking and an experimental passive gait are completed. The leg angle[1] of the simulations were in agreement with the physical experiments, when the simulations accounted for rolling resistance. However, the step period of the simulations were unable to match the physical experiments. Following McGeer there have been very limited results on validating mathematical models against experimental passive dynamic walker data. In [9], an experimental passive walker is used to demonstrate that the assumption that angular momentum is conserved during the instance of heel strike, to some degree, is a reasonable assumption. However, the effect the angular momentum assumption has on the gait is not analyzed. Experimental passive walking machines also provide insight in how to build actuated passive walkers. A review of three robots based on passive dynamic walkers are presented in [10].

1.2.2 Contact Dynamics Modeling

There are two basic forms for modeling contact impact events: Impulse–momentum (discrete) based and force–based (continuous) approaches. Impulse–momentum based methods include methods like Newton's coefficient of restitution, and Poision's method, which assume that the impact event occurs instantaneously, such that the position does not change during impact. Utilizing impulse–momentum based methods to describe the motion of a kinematic chain (i.e. a passive dynamic walker) requires special attention to the possible impact outcomes. The outcomes may include single support or double support, with one

[1] Angle between the legs at the instance of heel strike.

or both of the feet sliding after impact. Hurmuzlu and Chang [11] developed a method for determining the outcome of the impact of a planar kinematic chain using a impact–momentum base method. However, most passive walking models simply assume the heel strike is a no slip inelastic impact and angular momentum is conserved through the impact about the contact point.

Force–based methods describe the contact, not just the impact event, and can describe multiple-contact events. Force–based methods are used by simply adding the modeled forces to the equations of motion. The simplest forced–based method is a linear spring and damper model (1.1) referred to as the Kelvin-Voigt model. The contact force is described by the indentation or theoretical penetration, h, of the two contacting bodies. The parameter k_s describes the stiffness of the contact and k_d describes the contact damping.

$$F_N = k_s h + k_d \dot{h} \tag{1.1}$$

The Kelvin-Voigt model can determine a discontinuous contact force during an impact event. If the penetration velocity is sufficiently large, then as the two bodies come into contact, the contact force predicted by the Kelvin-Voigt model takes a discontinuous jump from zero. Hertz conducted research on the contact of elastic solids [12], from which force–based contact models were developed. The Hertz model, (1.2), has a parameter n, which is dependent on the material of the two bodies and geometry of the contact.

$$F_N = k_s h^n \tag{1.2}$$

However, the Hertz contact model does not incorporate any damping, so no energy is loss during an impact. The Hunt-Crossley contact model, (1.3), is a Hertz type contact model that includes contact damping [13]. The Hunt-Crossley contact model adds damping to the Hertz contact model, while overcoming the discontinuous problem of the Kelvin-Voigt model by making the damping term a function of the penetration.

$$F_N = k_s h^n + k_d h^p \dot{h}^q \tag{1.3}$$

There is an added degree of difficulty when it comes to numerically solving force–based contact models. With force based methods the resulting system of equations may become numerically stiff due to the large accelerations induce from impacts. Numerically solving stiff ODEs has become less difficult with the development of methods like [14]. A more comprehensive review of contact dynamics modeling is provided in [15].

1.2.3 Friction Modeling

Friction modeling is an important aspect of any dynamical model. Friction is ever present and neglecting friction may, in some cases, be too large of a simplification. The simplest dynamic friction model is the Coulomb friction model represented by (1.4), where v is the sliding velocity, μ_c is the Coulomb (kinetic) friction coefficient, and F_N is the normal force.

$$F_f = \mu_c F_N \operatorname{sgn}(v) \tag{1.4}$$

Many passive walking models assume the foot is in pure rolling and use a rolling resistance coefficient in place of the Coulomb friction coefficient in (1.4). However, there are other friction effects that, in some cases, cannot be neglected. Fig. 1.1 depicts some of the important friction effects, where the horizontal axis is the sliding velocity, and the friction force is the vertical axis. The parameter v_s in Fig. 1.1d) is the Stribeck velocity.

There are many different friction models that capture the effects shown in Fig. 1.1d). Many of these friction models take the form of (1.5), where the coefficient of friction is a function of the sliding velocity (v), Coulomb friction coefficient (μ_c), static friction coefficient (μ_s), and the Stribeck velocity (v_s). A more comprehensive review of friction

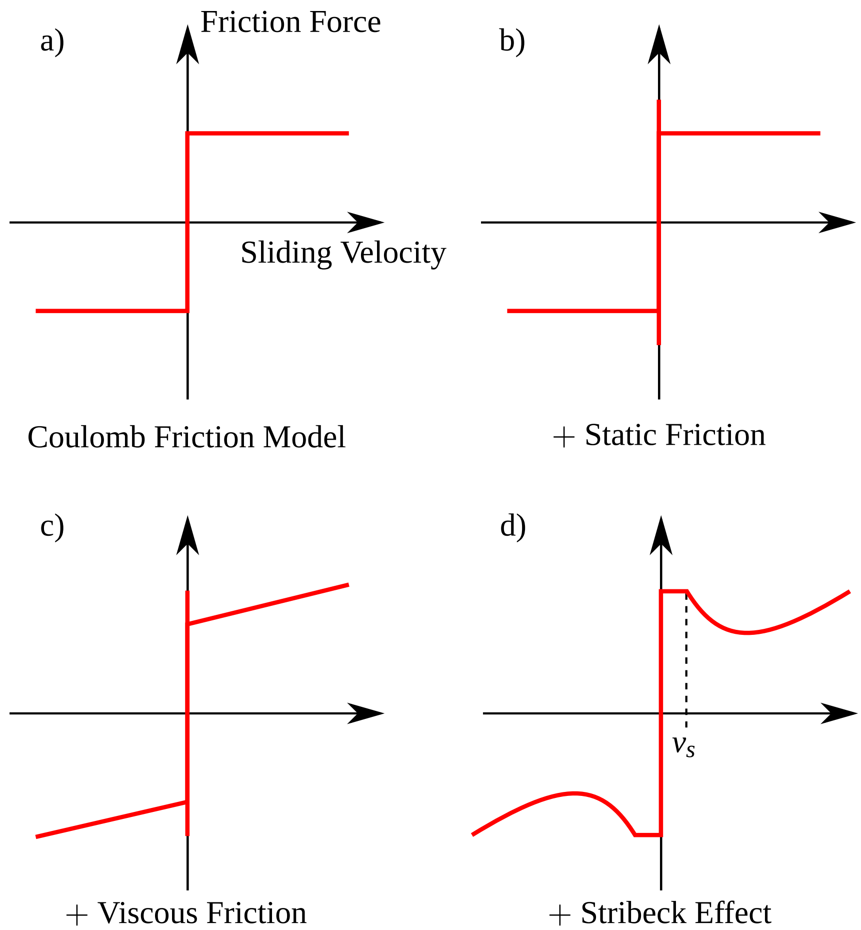

Figure 1.1: Visualization of different friction effects a) Coulomb friction model b) Coulomb friction model with static friction effects c) Coulomb friction model with static, and viscous friction effects d) Coulomb friction model with static, viscous, and Stribeck effects.

models is provided in [16].

$$F_f = F_N \mu(v, \mu_c, \mu_s, v_s) \tag{1.5}$$

While many of these friction models can capture the friction during sliding or micro-sliding, determining the friction force when $v = 0$ is not as easy. A more advanced friction model is the LuGre friction model [17], which can transition from zero sliding velocity to micro-sliding to sliding friction. The LuGre friction model is developed from the bristle interpretation of friction contact, where a tangential force will initially deflect the bristles and if sufficiently large the bristles begin to slip. The friction force of the LuGre model is described by (1.6), which is a function of a state observer (z), and viscous friction effects $(f(v))$. The friction state observer (z) is described by (1.7) and (1.8), where the state observer (z) can be visualized as the bristle deflection. The parameter σ_0 describes the elastic behaviour of the bristles and σ_1 describes the damping behaviour of the bristles.

$$F_f = -(\sigma_0 z + \sigma_1 \dot{z} + f(v))F_N \tag{1.6}$$

$$\dot{z} = v - \sigma_0 \frac{|v|}{g_L(v)} z \tag{1.7}$$

$$g_L(v) = \mu_c + (\mu_s - \mu_c) e^{-\left(\frac{v}{v_S}\right)^2} \tag{1.8}$$

1.2.4 Biped Dynamic Balance Measures

Stability and dynamic balance are defined here as two separate notions. A biped in a stable gait is moving in a periodic gait that if slightly disturbed will eventually return to the same periodic gait. A biped that maintains dynamic balance is upright with the ability to maintain forward locomotion. Thus, if a biped is in a stable gait it will maintain dynamic balance, but a biped that maintains dynamic balance is not necessarily in a stable gait.

The idea of biped dynamic balance measures is to reduce the complex dynamics of the biped to a single point or single idea that can be measured and used as feedback for the biped control system. Zero Moment Point (ZMP) was developed over forty years ago and is still used today [18]. The concept of ZMP is to maintain control over the passive joint (the contact between the foot and the ground). When the foot is flat on level ground, the ZMP and center of pressure coincide. If the ZMP is within the contact envelope and not on the boundary, the foot will not rotate in the horizontal direction. However maintaining the ZMP within the contact envelope can cause the biped to loose dynamic balance in some situations. For example, if the center of mass of the biped is outside the support polygon with a zero velocity, then maintaining the ZMP will act to drive the center of mass towards the ground.

Even when the foot is rotating the idea of ZMP can be used. This is labeled either

Fictitious Zero Moment Point (FZMP) [18] or Foot Rotation Indicator (FRI) [19]. The FZMP (or FRI) is the point on the ground where the ground reaction forces would have to act to stop the foot from rotating. More recently there has been a shift into understanding how the whole body angular momentum, and by extension ground reaction torque, effects the biped gait. Centroidal Moment Pivot (CMP) [20][21][2] describes the moment arm of the ground reaction torque with respect to the center of mass of the biped. The CMP can be used to monitor the dynamic balance of the biped with respect to the angular momentum. Angular momentum is important because the average angular momentum of a biped during a gait must be zero, otherwise the biped is rotating over about its center of mass. A review of the concepts of ZMP, FRI, and CMP is provided in [22].

1.3 Previous Work at the University of Manitoba

The start of the experimental research of passive dynamic walking, at the University of Manitoba, began with a study on a small wooden walker with straight legs [23]. Following the initial study, a small wooden kneed four-legged walker was built and rough measurements were taken with a 30 Hz video camera [24][25]. A second undergraduate thesis [26] was completed on passive walking, with a larger kneed passive walker, named Dexter, that was made out of aluminum flat bar. However, there were a number of issues with Dexter which limited the accuracy of the data. After these theses, the passive dynamic walking research was continued with undergraduate summer research completed by Dean Ferley and myself, from which a general report was completed. The NSERC summer report elaborated on the modifications made to Dexter, leading to Dexter Mk II. As well, a fair number of trials were completed with Dexter Mk II using a 60Hz video camera, resulting is slightly improved measurement accuracy compared to the previous experiments at the University of Manitoba. In the following summer of 2009 I designed and built another passive walker, named Dexter Mk III. The gait of Dexter Mk III was measured with an optical rotatory en-

[2]Referred to as Zero Spin Control Point (ZSCP) in [20] and Zero Rate of change of Angular Momentum (ZRAM) in [21].

coder to measure the hip joint angle, and an accelerometer to detect the heel strike events. Another undergraduate thesis was also completed at the University of Manitoba on passive dynamic walking, by Sean O'Brien during the fall term of 2009. O'Brien also built a passive dynamic kneed bipedal walker. Following this I completed my undergraduate thesis in the Winter semester of 2010 using Dexter Mk III to determine the equivalence of walking on a treadmill to walking on a ramp. Further research was completed with Dexter Mk III by Rushdi Kazi [27], where the effects of the mass distribution and flat feet were studied.

1.4 Objectives and Overview of the Thesis

The objective of this thesis was to develop a new mathematical model of passive dynamic walking that models the whole gait without switching between different sets of equations. The gait comprises of the single support phase, heel strike impact, and double support phase. To continuously model single contact dynamics, an impact event, and multi-contact dynamics, the Hunt-Crossley contact model and the LuGre friction model were incorporated in the proposed passive walking model. To validate the proposed passive walking model, a physical passive walker was designed and built. The resulting gait of both the physical passive walker and the proposed passive walking model were compared to determine the validity of the proposed passive walking model. The stability of the passive dynamic gait was analyzed using the proposed mathematical model. To determine if the angular momentum of a biped provides information about the biped's stability, the stability of the passive walker was quantified and compared against the angular momentum of the passive walker.

The thesis is organized as follows. Chapter 2 derives the proposed passive walking mathematical model and explains how the approximate solution is determined. As well, chapter 2 gives the derivation of an impact based passive dynamic mathematical model to compare the proposed mathematical model against. Chapter 3 provides details on the design of an experimental passive dynamic walker, the gait measurement system and the experimental methodology. Chapter 4 outlines a method to calculate the Lyapunov exponents of the proposed mathematical model. A method for finding the basin of attraction of a 2D projection of a system is outlined in chapter 4. Chapter 5 gives a comparison of the proposed mathematical model to a standard impact–based passive walking model. Chapter 5 also provides a validation of the mathematical model against the experimental results. The basin of attraction of the mathematical model is compared to the angular momentum of the walker as well. Chapter 6 summarizes the conclusions of the thesis and provides some areas for future work.

Chapter 2

Mathematical Modeling

2.1 Introduction

The derivation of a new mathematical model of passive dynamic biped walking is given in this chapter. The mathematical model uses the Hunt-Crossley contact model and the LuGre friction model to account for the ground reaction forces. The application of the Hunt-Crossley model and LuGre model to the passive walking model is explained. To solve the proposed mathematical model, the equations are transformed into the state space form. A review of the solution approximation method is provided. To compare the proposed passive dynamic walking mathematical model, a traditional impact model is derived. The impact model uses one set of equations for the swing phase and another set for the impact phase.

2.2 Proposed Mathematical Model

2.2.1 Derivation of Equations of Motion

The passive walking model consists of two links each with a distrusted mass and arced feet. The passive walking model also has a non–rotating mass located at the hip. The hip mass simulates the effects of an upper body. The proposed passive walking model is described by one unified set of equations that describes the entire motion of the passive walker. The proposed passive walking model is able to capture single support and double support[1] dynamics. The friction between the foot and ground is described by the LuGre friction model. The normal contact forces between the foot and the ground are described by the Hunt-Crossley model. The friction at the hip joint is neglected.

Figure 2.1 shows a schematic of the passive walking mathematical model, where l is the length of the legs, b is the distance of the leg center of mass from the hip, and ρ is the foot radius. The parameter δ is the angle offset of the foot. Each leg has a distributed mass m and a radius of gyration of r_g with respect to the center of mass. The hip joint of the passive walker is located by the two coordinates x_{hip} and y_{hip}. There is a non-rotating mass, denoted by M, located at the hip. The angle of each leg, with reference to the normal of the ramp, is denoted by θ_1 and θ_2. The ramp is at an inclination γ. The reference frame is rotated so that the x-axis is in line with the direction of the ramp. There are two points, c_1 and c_2, marked on the feet, which are the contacts points or impending contact points. The points c_1 and c_2 are the points on the feet with the lowest y coordinate.

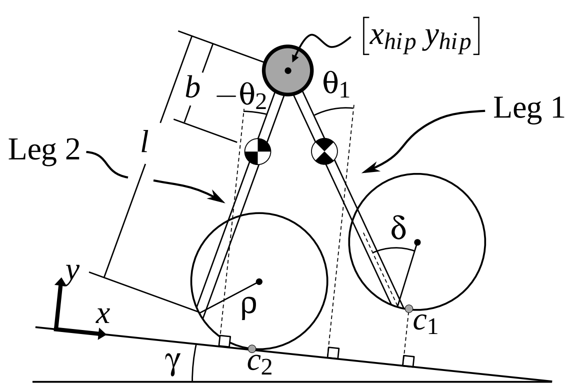

Figure 2.1: Model diagram.

The equations of motion are derived using Lagrangian mechanics which requires the kinetic and potential energy of the system. To start, the position (2.1) and the velocity (2.2)

[1]both feet on the ground

of the center of mass are determined, where $i = 1$ or 2.

$$\vec{r}_{CoM_i} = \begin{bmatrix} x_{hip} + b\sin\theta_i & y_{hip} - b\cos\theta_i \end{bmatrix} \tag{2.1}$$

$$\vec{v}_{CoM_i} = \begin{bmatrix} \dot{x}_{hip} + \dot{\theta}_i b\cos\theta_i & \dot{y}_{hip} + \dot{\theta}_i b\sin\theta_i \end{bmatrix} \tag{2.2}$$

Using the equations of the center of mass velocity, the kinetic energy of the system (2.3) is determined.

$$T = \frac{1}{2}m(\vec{v}^2_{CoM_1} + r_g^2\dot{\theta}_1^2) + \frac{1}{2}m(\vec{v}^2_{CoM_2} + r_g^2\dot{\theta}_2^2) + \frac{1}{2}M(\dot{x}^2_{hip} + \dot{y}^2_{hip}) \tag{2.3}$$

The height of the center of mass of the leg in the gravitationally plane, (2.4), is determined by rotating the position vector (2.1) by an angle γ.

$$\begin{aligned} h_{CoM_i} &= \begin{bmatrix} -\sin\gamma & \cos\gamma \end{bmatrix} \cdot \vec{r}_{CoM_i} \\ &= -\sin\gamma\left(x_{hip} + b\sin\theta_i\right) + \cos\gamma\left(y_{hip} - b\cos\theta_i\right) \end{aligned} \tag{2.4}$$

The potential energy of the system is then found to be (2.5).

$$\begin{aligned} V &= mgh_{CoM_1} + mgh_{CoM_2} + Mgh_{hip} \\ &= mg(\cos\gamma(y_{hip} - b\cos\theta_1) - \sin\gamma(x_{hip} + b\sin\theta_1)) \\ &\quad + mg(\cos\gamma(y_{hip} - b\cos\theta_2) - \sin\gamma(x_{hip} + b\sin\theta_2)) + Mg(y_{hip}\cos\gamma - x_{hip}\sin\gamma) \end{aligned} \tag{2.5}$$

Using the kinetic and potential energy of the system the Lagrangian, (2.6), is formed.

$$L = T - V \tag{2.6}$$

Substituting the Lagrangian into the Lagrange equation, (2.7), yields the equations of motion, (2.8).

$$\frac{d}{dt}\left(\frac{\partial L}{\partial \dot{q}_i}\right) - \frac{\partial L}{\partial q_i} = Q_i \tag{2.7}$$

$$\mathbf{M}(\mathbf{q})\ddot{\mathbf{q}} + \mathbf{H}(\mathbf{q},\dot{\mathbf{q}}) + \mathbf{G}(\mathbf{q}) = \mathbf{F}(\mathbf{q},\dot{\mathbf{q}}) \tag{2.8}$$

Where the matrix $\mathbf{q}$ describes the state of the system, $\mathbf{M}(\mathbf{q})$ is the mass matrix, $\mathbf{H}(\mathbf{q},\dot{\mathbf{q}})$ is the centripetal force matrix, $\mathbf{G}(\mathbf{q})$ is the gravitational force matrix, and $\mathbf{F}(\mathbf{q},\dot{\mathbf{q}})$ are the generalized forces on the system.

$$\mathbf{q} = \begin{bmatrix} x_{hip} \\ y_{hip} \\ \theta_1 \\ \theta_2 \end{bmatrix} \quad \dot{\mathbf{q}} = \begin{bmatrix} \dot{x}_{hip} \\ \dot{y}_{hip} \\ \dot{\theta}_1 \\ \dot{\theta}_2 \end{bmatrix} \quad \ddot{\mathbf{q}} = \begin{bmatrix} \ddot{x}_{hip} \\ \ddot{y}_{hip} \\ \ddot{\theta}_1 \\ \ddot{\theta}_2 \end{bmatrix} \tag{2.9}$$

$$\mathbf{M}(\mathbf{q}) = \begin{bmatrix} M+2m & 0 & mb\cos\theta_1 & mb\cos\theta_2 \\ 0 & M+2m & mb\sin\theta_1 & mb\sin\theta_2 \\ mb\cos\theta_1 & mb\sin\theta_1 & mb^2+r_g^2 & 0 \\ mb\cos\theta_2 & mb\sin\theta_2 & 0 & mb^2+r_g^2 \end{bmatrix} \tag{2.10}$$

$$\mathbf{H}(\mathbf{q},\dot{\mathbf{q}}) = \begin{bmatrix} -mb\dot{\theta}_1^2\sin\theta_1 - mb\dot{\theta}_2^2\sin\theta_2 \\ mb\dot{\theta}_1^2\cos\theta_1 + mb\dot{\theta}_2^2\cos\theta_2 \\ 0 \\ 0 \end{bmatrix} \tag{2.11}$$

$$\mathbf{G}(\mathbf{q}) = g\begin{bmatrix} -(M+2m)\sin\gamma \\ (M+2m)\cos\gamma \\ mb\sin(\theta_1-\gamma) \\ mb\sin(\theta_2-\gamma) \end{bmatrix} \tag{2.12}$$

$$\mathbf{F}(\mathbf{q},\dot{\mathbf{q}}) = \begin{bmatrix} F_{f_1}+F_{f_2} \\ F_{N_1}+F_{N_2} \\ F_{f_1}c_{y_1}^{hip} + F_{N_1}c_{x_1}^{hip} \\ F_{f_2}c_{y_2}^{hip} + F_{N_2}c_{x_2}^{hip} \end{bmatrix} \tag{2.13}$$

The normal force applied on each foot is denoted by F_{N_1} and F_{N_2}. The friction force of between each foot and the ground are denoted by F_{f_1} and F_{f_2}. The position of the contact points, shown in Fig. 2.1, relative to the hip is described by the vector $\vec{c}^{hip}$.

$$\vec{c}_i^{hip} = \begin{bmatrix} l\sin\theta_i - \rho\sin(\theta_i - \delta) & l\cos\theta_i - \rho(\cos(\theta_i - \delta) - 1) \end{bmatrix} \tag{2.14}$$

The global position of the contact points of the two feet are defined by $(\vec{c})$ and their corresponding velocities are defined by $(\dot{\vec{c}})$.

$$\vec{c}_i = \begin{bmatrix} x + l\sin\theta_i - \rho\sin(\theta_i - \delta) & y - l\cos\theta_i + \rho(\cos(\theta_i - \delta) - 1) \end{bmatrix} \tag{2.15}$$

$$\dot{\vec{c}}_i = \begin{bmatrix} \dot{x} + \dot{\theta}_i(l\cos\theta_i - \rho\cos(\theta_i - \delta) + \rho) & \dot{y} + \dot{\theta}_i(l\sin\theta_i - \rho\sin(\theta_i - \delta)) \end{bmatrix} \tag{2.16}$$

2.2.2 Contact Model

The Hunt-Crossley contact model [13] is an extension of the Hertz [12] contact model to include hysteretic damping in the contact forces. The Hertz contact model describes the contact forces of a static system by the indentation caused by contact of the two bodies. For dynamic simulations, the contact force is described by the inter-penetration, h, and the inter-penetration velocity, $\dot{h}$, of the two bodies. The inter-penetration and corresponding velocity are described by (2.17) and (2.18), respectively. Fig. 2.2 shows a schematic of the inter-penetration of the two bodies.

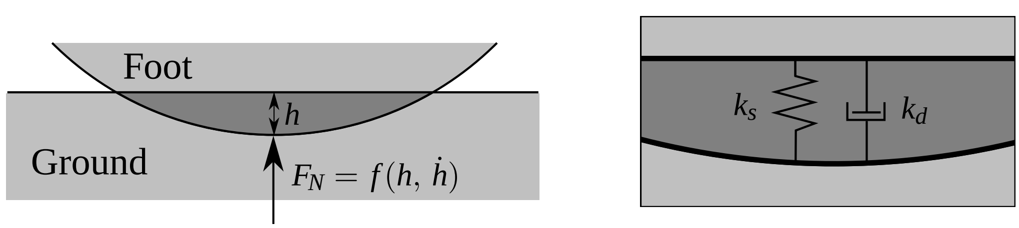

Figure 2.2: Contact diagram.

$$h_i = \begin{cases} 0 & \text{for } c_{y_i} > 0 \\ -c_{y_i} & \text{for } c_{y_i} < 0 \end{cases} \tag{2.17}$$

$$\dot{h}_i = \begin{cases} 0 & \text{for } y_{c_i} > 0 \\ -\dot{c}_{y_i} & \text{for } c_{y_i} < 0 \end{cases} \tag{2.18}$$

The level of the force (N_i) is determined by (2.19), where n, p, and q are dependent on the geometry of the contact and the material of the two bodies. For the passive dynamic walking model, $n = p = \frac{3}{2}$ and $q = 1$ was selected, which corresponds to a spherical or cylindrical contact.

$$N_i = k_s h_i^n + k_d h_i^p \dot{h}_i^q \tag{2.19}$$

The normal force, F_{N_i}, is equal to the level of force if the level of the force is greater than or equal to zero. How can the Hunt-Crossley model predict a negative normal force. The Hunt-Crossley model assumes the two bodies are joined once the inter-penetration is positive. However, if the restitution velocity is great enough, the level of force (2.19) can be negative even when h is positive. To account for this, condition (2.20) is introduced. In reality this situation would occur when separation of the two bodies occurs before both bodies have restored to their undeformed shape.

$$F_{N_i} = \begin{cases} N_i & \text{for } N_i > 0 \\ 0 & \text{for } N_i < 0 \end{cases} \tag{2.20}$$

The advantage of using a force based contact model, like the Hunt-Crossley model, is that there is no need to switch between two sets of equations for each impact. As well, the Hunt-Crossley model can simulate multiple contact dynamics, which is important for biped walking to simulate the double support phase.

2.2.3 Friction Model

The friction between the foot and the surface is modeled using the LuGre friction model [17]. The LuGre friction model is a continuous dynamic model that can describe the static friction force, Coulomb friction force, and the transition between the two. The LuGre model can be visualized as two sets of elastic bristles, as shown in Fig 2.3, where z is the bristle deflection. The bristles will deflect until a large enough force is applied and the two surfaces slide over one another. The friction force determined by the LuGre friction model is shown in equation (2.21), where the terms that describe the viscous friction are omitted.

$$F_{f_i} = -(\sigma_0 z_i + \sigma_1 \dot{z}_i) F_{N_i} \tag{2.21}$$

$$\dot{z}_i = v_i - \sigma_0 \frac{|v_i|}{g_L(v_i)} z_i \tag{2.22}$$

$$g_L(v_i) = \mu_c + (\mu_s - \mu_c) e^{-\left(\frac{v_i}{v_s}\right)^2} \tag{2.23}$$

Where $i = 1$ or 2 corresponding to each foot. The sliding velocity between the two surfaces, v_i, is represented by $\dot{c}_{x_i}$ in the passive walking model.

$$\dot{c}_{x_i} = \dot{x} + \dot{\theta}_i (l \cos\theta_i - \rho \cos(\theta_i - \delta) + \rho) \tag{2.24}$$

The variables σ_0 and σ_1 control the stiffness and damping of the bristle deflection. The static and Coulomb friction coefficients are represented by μ_s and μ_c, respectively. The Stribeck velocity is represented by v_s.

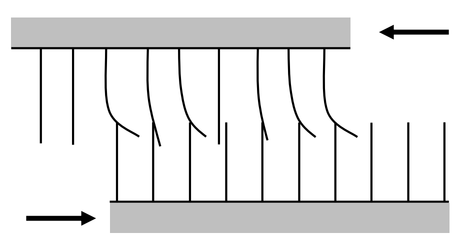

Figure 2.3: Visualized LuGre model.

2.2.4 State Space Model

In order to solve the mathematical model the equations are transformed into a state space representation. The state space model is formed from incorporating the friction state observers (2.22) and the contact force equations (2.21) and (2.20) with the equations of the motion (2.8). The final state space model (2.25) has ten states that are described in (2.26).

$$\dot{\mathbf{Q}} = f(\mathbf{Q}) \tag{2.25}$$

$$\begin{aligned}\mathbf{Q} &= \begin{bmatrix} Q_1 & Q_2 & Q_3 & Q_4 & Q_5 & Q_6 & Q_7 & Q_8 & Q_9 & Q_{10} \end{bmatrix}^T \\ &= \begin{bmatrix} x_{hip} & y_{hip} & \theta_1 & \theta_2 & \dot{x}_{hip} & \dot{y}_{hip} & \dot{\theta}_1 & \dot{\theta}_2 & z_1 & z_2 \end{bmatrix}^T \end{aligned} \tag{2.26}$$

$$\begin{bmatrix} \dot{\mathbf{Q}}_1 \\ \dot{\mathbf{Q}}_2 \\ \dot{\mathbf{Q}}_3 \\ \dot{\mathbf{Q}}_4 \end{bmatrix} = \begin{bmatrix} \mathbf{Q}_5 \\ \mathbf{Q}_6 \\ \mathbf{Q}_7 \\ \mathbf{Q}_8 \end{bmatrix} \quad \text{and} \quad \begin{bmatrix} \dot{\mathbf{Q}}_5 \\ \dot{\mathbf{Q}}_6 \\ \dot{\mathbf{Q}}_7 \\ \dot{\mathbf{Q}}_8 \end{bmatrix} = \mathbf{A}(\mathbf{Q})^{-1}\mathbf{B}(\mathbf{Q}) \tag{2.27}$$

$$\dot{\mathbf{Q}}_9 = v_1(\mathbf{Q}) - \sigma_0 \frac{|v_1(\mathbf{Q})|}{g_1(v_1(\mathbf{Q}))} Q_9 \tag{2.28}$$

$$\dot{\mathbf{Q}}_{10} = v_2(\mathbf{Q}) - \sigma_0 \frac{|v_2(\mathbf{Q})|}{g_2(v_2(\mathbf{Q}))} Q_{10} \tag{2.29}$$

Where (2.28) and (2.29) are the state space form of the friction state observer equation (2.22). The matrices $\mathbf{A}(\mathbf{Q})$ and $\mathbf{B}(\mathbf{Q})$ are defined by (2.30) and (2.31). For matrices $\mathbf{M}(\mathbf{Q})$, $\mathbf{H}(\mathbf{Q})$, $\mathbf{G}(\mathbf{Q})$, $\mathbf{F}(\mathbf{Q})$, refer to (2.10), (2.11), (2.12), and (2.13), respectively, on page 14.

$$\mathbf{A}(\mathbf{Q}) = \mathbf{M}(\mathbf{Q}) \tag{2.30}$$

$$\mathbf{B}(\mathbf{Q}) = \mathbf{F}(\mathbf{Q}) - \mathbf{H}(\mathbf{Q}) - \mathbf{G}(\mathbf{Q}) \tag{2.31}$$

The inverse of $\mathbf{A}(\mathbf{Q})$ was solved manually and simplified to the form shown in (2.32)

$$\mathbf{A}(\mathbf{Q})^{-1} = \begin{bmatrix} \frac{A_M(c_1^2+c_2^2+A_M)+C_mC_p}{M_W} & \frac{A_{sc}(A_M+1)}{M_W} & -\frac{C_{AC}}{b} & -\frac{C_{CA}}{b} \\ \frac{A_{sc}(A_M+1)}{M_W} & \frac{A_M(s_1^2+s_2^2+A_M)-C_mC_p}{M_W} & -\frac{S_{AC}}{b} & -\frac{S_{CA}}{b} \\ -\frac{C_{AC}}{b} & -\frac{S_{AC}}{b} & \frac{A_MM_W}{b^2} & \frac{C_mM_W}{b^2} \\ -\frac{C_{CA}}{b} & -\frac{S_{CA}}{b} & \frac{C_mM_W}{b^2} & \frac{A_MM_W}{b^2} \end{bmatrix} \frac{1}{m(A_M^2-C_m^2)} \tag{2.32}$$

$$M_W = 2 + \frac{M}{m} \tag{2.33}$$

$$A_M = M_W\left(1+\left(\frac{r_g}{b}\right)^2\right) - 1 \tag{2.34}$$

$$A_{sc} = \sin(Q_3)\cos(Q_3) + \sin(Q_4)\cos(Q_4) \tag{2.35}$$

$$C_m = \cos(Q_3 - Q_4), \, S_m = \sin(Q_3 - Q_4) \tag{2.36}$$

$$C_p = \cos(Q_3 + Q_4), \, S_p = \sin(Q_3 + Q_4) \tag{2.37}$$

$$C_{CA} = \cos(Q_3)C_m + \cos(Q_4)A_M \tag{2.38}$$

$$S_{CA} = \sin(Q_3)C_m + \sin(Q_4)A_M \tag{2.39}$$

$$C_{AC} = \cos(Q_3)A_M + \cos(Q_4)C_m \tag{2.40}$$

$$S_{AC} = \sin(Q_3)A_M + \sin(Q_4)C_m \tag{2.41}$$

$$\mathbf{B}(\mathbf{Q}) = \begin{bmatrix} (F_{f_1}+F_{f_2}) + mb(Q_7^2\sin Q_3 + Q_8^2\sin Q_4) + g(M+2m)\sin\gamma \\ (F_{N_1}+F_{N_1}) - mb(Q_7^2\cos Q_3 + Q_8^2\cos Q_4) - g(M+2m)\cos\gamma \\ F_{f_1}c_{y_1}^{hip} + F_{N_1}c_{x_1}^{hip} - mgb\sin(Q_3-\gamma) \\ F_{f_2}c_{y_2}^{hip} + F_{N_2}c_{x_2}^{hip} - mgb\sin(Q_4-\gamma) \end{bmatrix} \tag{2.42}$$

The normal force F_{N_i} is defined by (2.20) on page 16. The friction force F_{f_i} is defined by (2.21) on page 17. The contact positions relative to the hip, $\vec{c}_i^{hip}$, is defined by (2.14) on page 15.

2.3 Solution Procedure

2.3.1 Numerical Solution Approximation

To approximate a solution to the proposed mathematical model (2.25), the code ODE15S was used. ODE15S is a Matlab code for solving stiff ODEs and DAEs, which is based on the Numerical Differentiation Formulas (NDF). The NDF are a family of formulas used to approximate solutions to ODEs and DAEs and are given by (2.43)

$$\sum_{m=1}^{k} \frac{1}{m} \nabla^m y_{n+1} - hF(t_{n+1}, y_{n+1}) - \kappa\gamma_k (y_{n+1} - y_{n+1}^{(0)}) = 0 \tag{2.43}$$

The NDF are an extension of the Backwards Difference Formulas, where $-\kappa\gamma_k(y_{n+1} - y_{n+1}^{(0)})$ is the additional term. The term κ is a scalar parameter used to tune the stability and local truncation error (LTE) of the method and $\gamma_k = \sum_{j=1}^{k} \frac{1}{j}$. The ODE15S code uses $A(\alpha)$ stability to monitor the stability of the solver. The ODE15S code uses the Jacobian of the system if supplied, and will numerically estimate the Jacobian if not supplied. A detailed derivation of the ODE15S code can be found in [14].

The form of (2.43) used to numerical integrate the state space model is shown in (2.44), where the fifth order version of (2.43) was used $(k = 5)$. The function $f(\mathbf{Q})$ is defined in (2.25) and $\mathbf{Q}$ is defined in (2.26) on page 18.

$$\sum_{m=1}^{5} \frac{1}{m} \nabla^m \mathbf{Q}_{n+1} - hf(\mathbf{Q}) - \kappa\gamma_5 (\mathbf{Q}_{n+1} - \mathbf{Q}_{n+1}^{(0)}) = 0 \tag{2.44}$$

To clarify the notation used $\mathbf{Q}_{n+1} = \mathbf{Q}(t_{n+1})$, $\mathbf{Q}^{(0)}$ is the initial estimate of the states, and ∇ is the backward difference operator.

2.3.2 Swing Leg Ground Clearance

Unlike biped walkers with knees, two link biped walkers need a mechanism for the swing leg to clear the ground. In physical experiments this ground clearance can be created with "stepping stones". In the numerical simulations the effect of stepping stones is established by switching between two support phases, single support and double support. The two support phases are represented by *Double Support* $=$ True or False. In the single support phase, one leg is the stance leg and the other the swing leg. The leg that is the swing leg can penetrate the ground without incurring reaction forces. The initial conditions are chosen so that the walker is just starting the swing phase of the next leg, therefore *Double Support* $=$ False and *Stance Leg* = Leg 1 if $\theta_1 > \theta_2$ or *Stance Leg* = Leg 2 if $\theta_2 > \theta_1$.

During the simulation, at every time step, the program checks if the system has transitioned to another phase. The transition to double support is determined by the condition in Fig. 2.4 and the transition to single support is determined by the condition in Fig. 2.5. The parameter c_y is the y-coordinate of the contact point, and α_0 is the minimum inner leg angle.

Once the support phase and stance leg are determined, the value of the penetration, h, and penetration velocity, $\dot{h}$, are determined. Initially the penetration and penetration velocity are set to zero and are only changed if the condition in Fig. 2.6 is met.

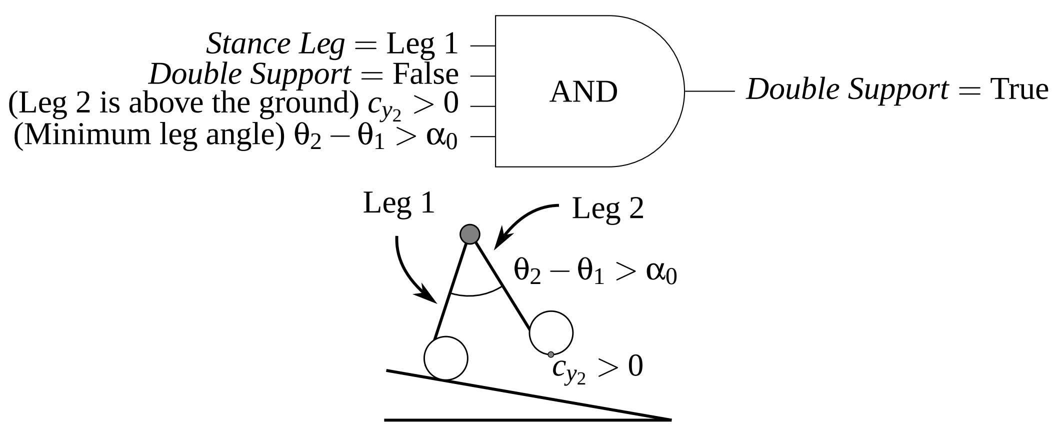

Figure 2.4: Transition to double support from Leg 1, vice versa for transition to double support from Leg 2.

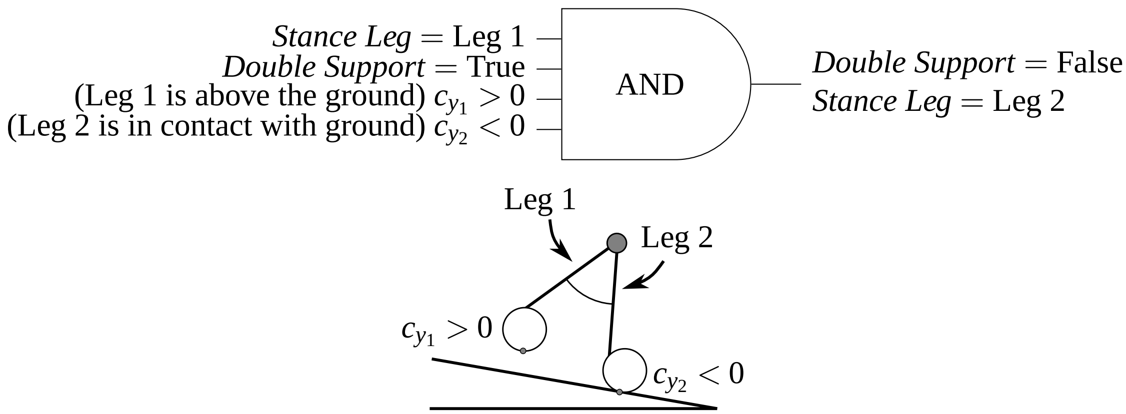

Figure 2.5: Transition to single support on Leg 2 from double support, vice versa for transition to single support on Leg 1

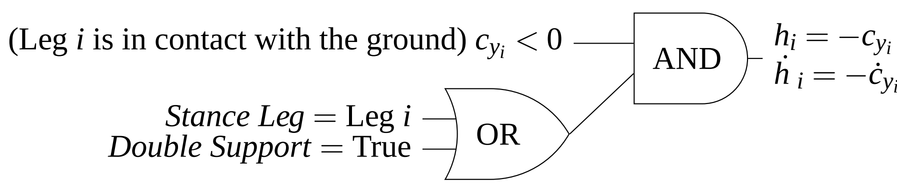

Figure 2.6: Determining the value of h_i and $\dot{h}_i$ for leg i, where $i = 1$ or 2.

2.4 Standard Impact Passive Walking Model

To compare the proposed mathematical model, a standard passive walking impact model was derived. The standard impact model derived in this section is similar to the impact-based passive walking models used by other researchers. The model developed in [4] assumed that $m << M$ so that the swing leg does not effect the stance leg, but the same assumptions are used for the impact equations that are used in this section. If $\rho = 0$ and $\delta = 0$, the impact model derived in this section simplifies to the model presented in [5]. The standard impact model has two parts, the equations of motion (2.45) and the impact transition equations (2.55). The subscript '*st*' refers to the stance leg and the subscript '*sw*' refers to the swing leg.

$$\begin{bmatrix} M_{1,1} & M_{1,2} \\ M_{2,1} & M_{2,2} \end{bmatrix} \begin{bmatrix} \ddot{\theta}_{st} \\ \ddot{\theta}_{sw} \end{bmatrix} + \begin{bmatrix} H_{1,1} & H_{1,2} \\ H_{2,1} & 0 \end{bmatrix} \begin{bmatrix} \dot{\theta}_{st}^2 \\ \dot{\theta}_{sw}^2 \end{bmatrix} + \begin{bmatrix} G_1 \\ G_2 \end{bmatrix} = \begin{bmatrix} F_1 \\ F_2 \end{bmatrix} \tag{2.45}$$

where

$$\begin{aligned}
M_{1,1} &= (m+M)l^2 + m(c^2+r_g^2) + 2\rho^2(2m+M)(1-\cos(\theta_{st}-\delta)) \\
&\quad + 2\rho((m+M)l+mc)(\cos\theta_{st}-\cos\delta) && (2.46) \\
M_{1,2} &= -mlb\cos(\theta_{st}-\theta_{sw}) + m\rho b(\cos(\theta_{st}-\theta_{sw}-\delta)-\cos\theta_{sw}) && (2.47) \\
M_{2,1} &= -mlb\cos(\theta_{st}-\theta_{sw}) + m\rho b(\cos(\theta_{st}-\theta_{sw}-\delta)-\cos\theta_{sw}) && (2.48) \\
M_{2,2} &= m(b^2+r_g^2) && (2.49)
\end{aligned}$$

$$\begin{aligned}
H_{1,1} &= \rho^2(2m+M)\sin(\theta_{st}-\delta) - \rho((m+M)l+mc)\sin\theta_{st} && (2.50) \\
H_{1,2} &= -mlb\sin(\theta_{st}-\theta_{sw}) + m\rho b\,(\sin(\theta_{st}-\theta_{sw}-\delta)+\sin\theta_{sw}) && (2.51) \\
H_{2,1} &= mlb\sin(\theta_{st}-\theta_{sw}) - m\rho b\sin(\theta_{st}-\theta sw-\delta) && (2.52)
\end{aligned}$$

$$\begin{aligned}
G_1 &= g\,(-((m+M)l+mc)\sin(\theta_s t-\gamma) + \rho\,((2m+M)(\sin(\theta_{st}-\delta-\gamma)+\sin\gamma)) && (2.53) \\
G_2 &= gmb\sin(\theta_{sw}-\gamma) && (2.54)
\end{aligned}$$

The impact transition equations are based on the assumption that angular momentum is conserved for the whole walker about the point of contact and for the stance leg about the hip. The post impact angular velocities are determined by (2.55) and the post impact angular positions are determined by (2.56), where the superscript '$-$' denotes a state before the impact and '$+$' denotes a state after the impact.

$$\begin{bmatrix} Q_{1,1}^- & Q_{1,2}^- \\ Q_{2,1}^- & 0 \end{bmatrix} \begin{bmatrix} \theta_{st}^- \\ \theta_{sw}^- \end{bmatrix} = \begin{bmatrix} Q_{1,1}^+ & Q_{1,2}^+ \\ Q_{2,1}^+ & Q_{2,2}^+ \end{bmatrix} \begin{bmatrix} \theta_{st}^+ \\ \theta_{sw}^+ \end{bmatrix} \tag{2.55}$$

$$\begin{bmatrix} 0 & 1 \\ 1 & 0 \end{bmatrix} \begin{bmatrix} \theta_{st}^- \\ \theta_{sw}^- \end{bmatrix} = \begin{bmatrix} \theta_{st}^+ \\ \theta_{sw}^+ \end{bmatrix} \tag{2.56}$$

$$
\begin{aligned}
Q^{-}_{1,1} = {} & \rho^2(2m+M)\Big(1-\cos(\theta_{st}-\delta)-\cos(\theta_{sw}-\delta)+\cos(\theta_{st}-\theta_{sw})\Big) \\
& +\rho\Big(((m+M)l+mc)\left(\cos\theta_{st}+\cos\theta_{sw}-\cos(\theta_{st}-\theta_{sw}-\delta)-\cos(\theta_{st}-\theta_{sw}+\delta)\right) \\
& +mb(\cos\delta-\cos\theta_{st})\Big)+(2mlc+Ml^2)\cos(\theta_{st}-\theta_{sw})-mbc
\end{aligned}
\tag{2.57}
$$

$$
Q^{-}_{1,2} = m\rho b\left(\cos\delta-\cos\theta_{sw}\right)-mbc \tag{2.58}
$$

$$
Q^{-}_{2,1} = m\rho b\left(\cos\delta-\cos\theta_{st}\right)-mbc \tag{2.59}
$$

$$
\begin{aligned}
Q^{+}_{1,1} = {} & 2\rho^2(2m+M)\Big(1-\cos(\theta_{st}-\delta)\Big)+\rho\Big(2((m+M)l+mc)(\cos\theta_{st}-\cos\delta) \\
& +mb(\cos(\theta_{st}-\theta_{sw}-\delta)-\cos\theta_{sw})\Big)+(m+M)l^2+mc^2-mlb\cos(\theta_{st}-\theta_{sw})
\end{aligned}
\tag{2.60}
$$

$$
Q^{+}_{1,2} = m\rho b(\cos(\theta_{st}-\theta_{sw}-\delta)-\cos\theta_{sw})+mb^2-mlb\cos(\theta_{st}-\theta_{sw}) \tag{2.61}
$$

$$
Q^{+}_{2,1} = m\rho b(\cos(\theta_{st}-\theta_{sw}-\delta)-\cos\theta_{sw})-mlb\cos(\theta_{st}-\theta_{sw}) \tag{2.62}
$$

$$
Q^{+}_{2,2} = mb^2 \tag{2.63}
$$

To determine a numerical approximation to the impact model, ODE45 in Matlab was used to solve the equations of motion. The equations of motion are solved until the swing foot comes in contact with the ground. Then the final state of the system is used as the pre–impact state to calculate the post–impact state with (2.55) and (2.56). The post impact velocities and the final position of the walker are then used as the initial conditions for the next step, and the equations of motion are solved once again.

2.5 Summary

A new passive walking mathematical model was developed in this chapter. The proposed model incorporates a continuous contact and friction force models. The proposed model avoids discontinuities in the solution unlike standard impact based passive walking model.

The standard impact based passive walking model switches between two sets of equations, one for the swing dynamics and the other for the impact phase. The proposed mathematical model is able to model multi–contact scenarios and contact sliding. The simulation procedure for the proposed mathematical model was outlined along with a brief explanation of the solution approximation method.

Chapter 3

Experimental Passive Biped Walker

3.1 Introduction

To validate the proposed passive walking mathematical model, presented in the previous chapter, an experimental passive walking machine was built and was named HM2L (Hip Mass 2 Links). A system was developed to measure the gait of the experimental passive walker. This chapter presents the design of the experimental passive walker, gait measurement system and the test platform.

3.2 Design goals

One of the main design goals, compared to previous walkers that I built [28], was to make the walker able to sustain repeated falls, since the potential for the walker to collapse is always present. As well, sensors were incorporated in the design of HM2L to measure gait parameters. To validate the mathematical model, a series of experiments with different parameters was required. Therefore HM2L was designed to be able to vary these different parameters. There are three main categories of parameters for a passive dynamic walker: mass parameters, geometric parameters and contact parameters.

3.2.1 Mass Parameters

The mass parameters of HM2L include: the center of mass and radius of gyration of each link, and the hip mass. To obtain different center of mass values without having to add a substantial amount of weight, the frame of the walker was designed to be light weight. Then with weights added to the legs, the center of mass can be changed. Another advantage of having a light weight frame with added weights is that the differences in mass parameters between the legs will be minimized by the added mass. The hip was designed to rotate independently of the two legs with a section for weight to be added.

3.2.2 Geometric Parameters

The geometric parameters of HM2L include: length of the legs, foot radius, and foot center offset. Two sets of feet with the same foot radius were made for HM2L. The first set was designed to create different foot center offsets. The second set was designed to change the length of the legs.

3.2.3 Contact Parameters

The contact parameters of HM2L are the foot contact stiffness and damping, and foot contact friction. The foot contact parameters are important for developing a stable gait. Having a large enough friction coefficient at the foot-ground contact to prevent sliding, but not too large to prevent smooth motion is crucial. As well, the foot-ground impact should be inelastic and be dampened to prevent vibration throughout the walker.

3.3 Experimental Setup

3.3.1 Physical Model Overview

The experimental passive biped walker, HM2L, is shown in Fig. 3.1. HM2L consists of two links with arced feet and a hip mass. The hip mass can rotate independently from the two legs. HM2L has no means for swing foot clearance so the biped walker must walk on “stepping stones” as shown in Fig. 3.2. To measure the gait parameters of the experimental passive biped walker, the design for HM2L incorporated two optical rotary encoders to measure the relative rotation between each leg, a single inclinometer to determined global orientation, and an accelerometer to detect the instance of heel strike.

The legs of the experimental walker are connected to the hip via roller bearings. To limit the motion of the passive walker to the sagittal plane the inside leg pair and outside

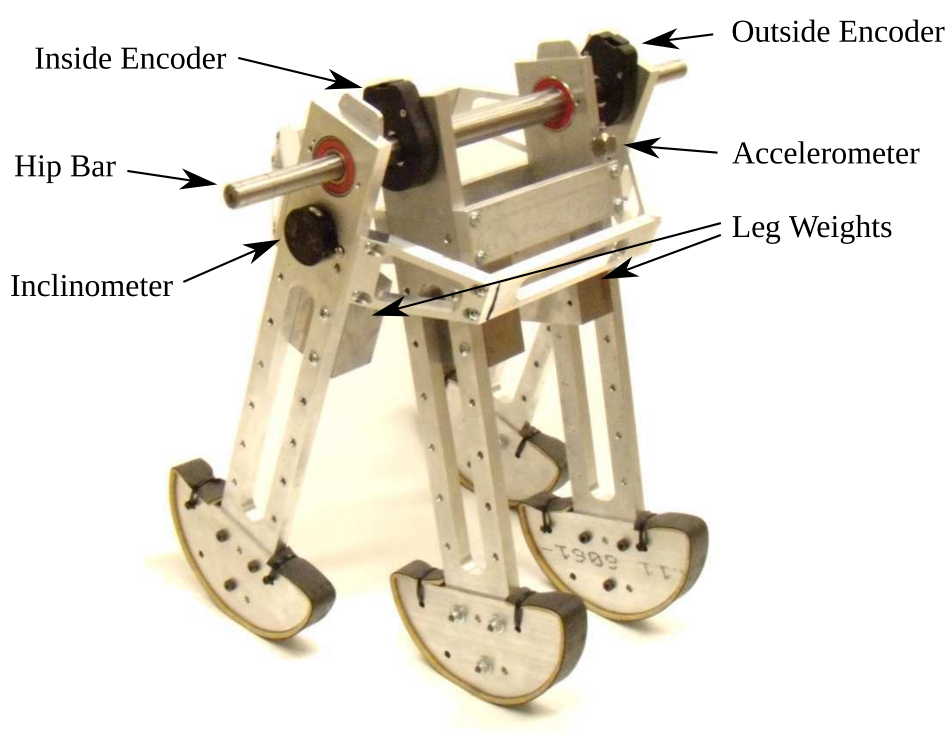

Figure 3.1: Photo of HM2L.

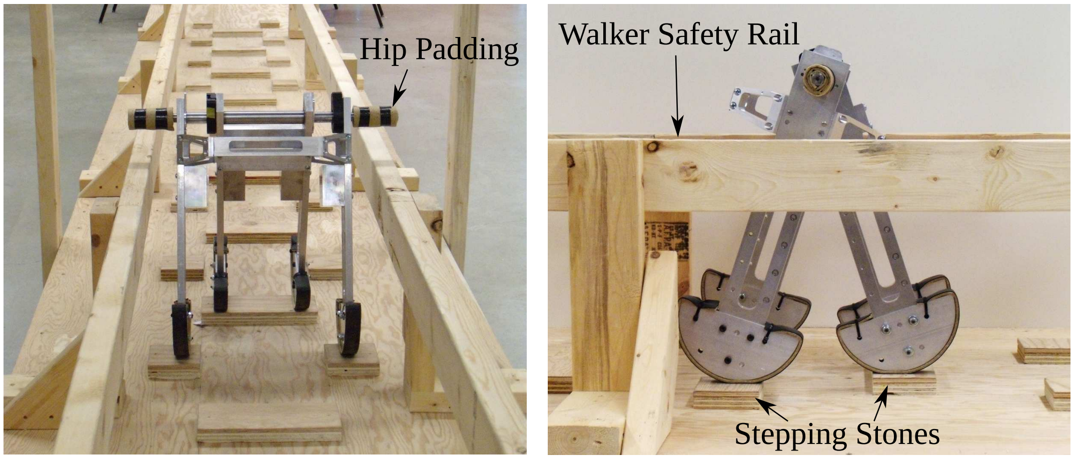

Figure 3.2: Photos of HM2L on the test ramp.

leg pair are coupled together. HM2L also has four movable leg weights, shown in Fig. 3.1. The leg weights consist of 45% of the walkers total mass and can be moved to six discrete locations. Moving the leg weights can produce a change in the center of mass from 33% to 56% of the walker's height (measured from the hip). The feet can be placed at five discrete locations to produce five different arc center offsets. Another set of feet were made, shown in Fig. 3.3, that allow the length of the legs to be increased by 3.81cm increments to a total increase of 11.42cm. Weights were modified to fit onto the hip bar, shown in Fig. 3.3, and can be locked in place by spring clips placed in the groves of the hip. With the hip weights made, seven different hip mass/total mass ratios are possible, ranging from 11% to 75%. For experiments that did not use the hip weights, padding was added to the hip, as shown

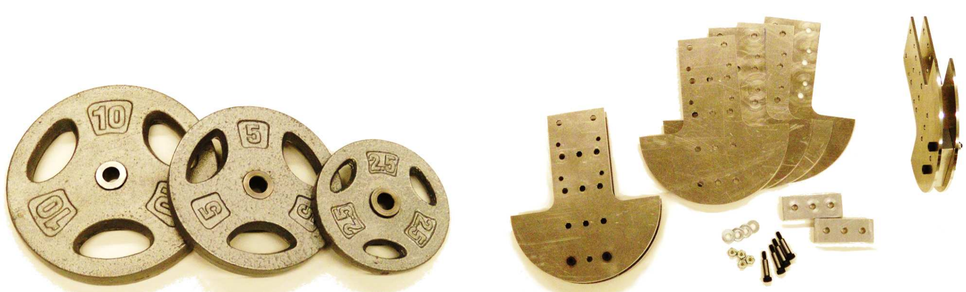

Figure 3.3: Hip weights and leg extensions.

in Fig. 3.2. The hip padding provided some protection when the walker would fall on the walker safety rail. For the experiments conducted the geometric parameters of HM2L are shown in Table 3.1 and the dynamic parameters are shown in Table 3.2 for the leg weights at the highest position.

Table 3.1: WALKER GEOMETRIC PARAMETERS.

Item	Symbol	Measurement
Walker Height	l	$40.64 cm$
Walker Width	w	$30.61\, cm$
Foot Radius*	ρ	$8.13\, cm$

*With no sole.

Table 3.2: WALKER DYNAMIC PARAMETERS.

Item	Inside		Outside	
Mass (kg)	5.144	44.24%	5.172	44.49%
Center of Mass (cm)	13.59	33.05%	13.52	32.88%
Radius of Gyration (cm)	11.83	28.76%	12.02	29.23%
Hip Mass (kg)	1.282			
Total Mass (kg)	11.598			

*Center of mass is measured from the the hip joint
**Radius of gyration is with respect to the center of mass.

3.3.2 Test Ramp

A test ramp was designed and built for the passive walker experiments. The test ramp, shown in Fig. 3.4, is 32 feet $(9.75m)$ long and 2 feet 10 inches $(0.86m)$ wide. The test ramp is made out of 16 inch engineered floor joists that are 16 feet long. Sixteen foot long joists were the maximum length that could fit through the hallways and into the lab. The floor joists are spliced together in the middle with $5/8$ inch plywood to make one 32 foot long joist. The joists are spaced 16 inches on center with blocking every 8 feet. The top deck is made of $5/8$ inch plywood screwed to the joists and $1/4$ inch sanded plywood on top. The $1/4$ inch sanded plywood can be removed to resurface the ramp without diminishing the

Figure 3.4: Test ramp.

structural integrity of the ramp. Two adjustable supports were made to change the angle of the ramp. One support is placed at the top of the ramp and the other mid way down the ramp where the joists are spliced together. The supports have a 3ply 2×6 inch laminated beam that the ramp sits on. The 3ply 2×6 inch laminated beam is supported by a $3/4$ inch threaded rod on each end that is held in placed by a 2×6 inch C–channel.

3.4 Gait Measurement

Four devices were used to measure aspects of the gait of the experimental walker: two rotary optical encoders, one accelerometer, and an inclinometer. The two optical rotary encoders have 7200 counts per revolution giving a 0.05° resolution. The encoders provide the relative angle between the corresponding leg set and the hip bar. The accelerometer is a Kistler Miniature PiezoBeam Triaxial accelerometer with a range of ± 50g. The inclinometer is a US Digital X3M absolute inclinometer that uses MEMS accelerometers to determine the orientation angle.

To capture a good representation of the gait of the experimental walker, the step period, step length, and average hip velocity were measured. To measure these gait parameters three things are needed: the time of each heel strike, the inner leg angle, and the geometry

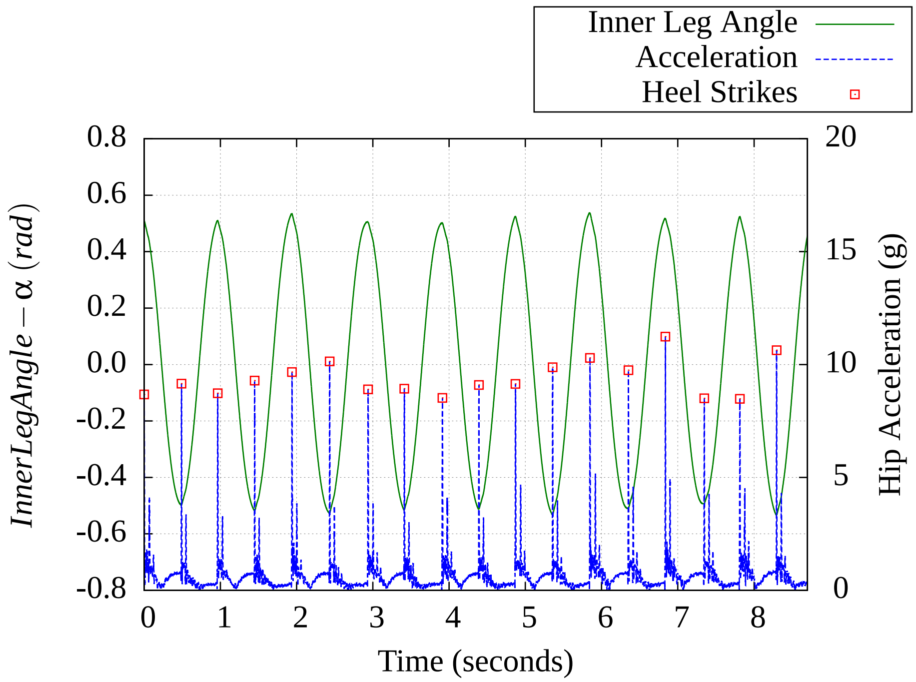

Figure 3.5: Example of experimental data.

of the walker. An accelerometer was attached to the walker at the location shown in Fig. 3.1. This location was chosen so that the accelerometer would be protected from damage and so the cable would have a minimal effect on the gait. The time of each heel strike was determined from the peak of the measured acceleration. The inner leg angle was determined from the difference between the two encoder measurements. The step period can then be determined from the time difference between consecutive heel strikes. The step length can be determined from the measured inner leg angle and the geometry of the walker. The average hip velocity can be determined with a combination of the inner leg angle, step period, and the geometry of the walker. Fig. 3.5 shows a sample of experimental data taken during a trial. The red squares in Fig. 3.5 are the maximum measured acceleration caused by each heel strike. The leg angles (with respect to the ramp normal) at the point of heel strike can be calculated using the measured inner leg angle (α) and (3.1) and (3.2). When $\alpha > 0$, (3.1) and (3.2), calculate the lead leg (ld) and trail leg (tr) angles, respectively. If

$\delta = 0$, then $\theta_{ld} = \alpha/2$ and $\theta_{tr} = -\alpha/2$.

$$\theta_{ld} = \arctan \frac{l\,(1-\cos\alpha)+\rho\,(\cos(\alpha+\delta)-\cos\delta)}{l\sin\alpha+\rho\,(-\sin(\alpha+\delta)+\sin\delta)} \tag{3.1}$$

$$\theta_{tr} = \arctan \frac{l\,(1-\cos\alpha)+\rho\,(\cos(\alpha-\delta)-\cos\delta)}{-l\sin\alpha+\rho\,(\sin(\alpha-\delta)+\sin\delta)} \tag{3.2}$$

Using the calculated leg angles, the step length, L_{step}, can be calculated using (3.3).

$$L_{step} = (l\sin\theta_{ld} - \rho\sin(\theta_{ld}-\delta)) - (l\sin\theta_{tr} - \rho\sin(\theta_{tr}-\delta)) \tag{3.3}$$

The average hip velocity, $\bar{v}_{hip}$, can be calculated using (3.4), where T_{step} is the step period, θ_{ld}^{0} is the angle of the front leg at the start of the step, and θ_{tr}^{1} is the angle of the same leg at the end of the step.

$$\begin{aligned}\bar{v}_{hip} &= \frac{c_x^{hip^0} - c_x^{hip^1} + \rho\left(\theta_{ld}^0 - \theta_{tr}^1\right)}{T_{step}} \\ &= \frac{\left(l\sin\theta_{ld}^0 - \rho\sin(\theta_{ld}^0-\delta)\right) - \left(l\sin\theta_{tr}^1 - \rho\sin(\theta_{tr}^1-\delta)\right) + \rho\left(\theta_{ld}^0 - \theta_{tr}^1\right)}{T_{step}}\end{aligned} \tag{3.4}$$

3.4.1 Data Acquisition

The data collected was captured with a Quanser Q8 data acquisition board connected to a PC. The data was saved with a Simulink program that uses features from QuaRC[1]. The two encoders were directly connected to the Q8 data acquisition board encoder inputs. The accelerometer connects to three power conditioners, one per axis, and then to the Q8 data acquisition board analog inputs. The inclinometer generates a pulse width modulation (PWM) signal and was connected to the Q8 data acquisition board digital inputs. The PWM signal was decoded during the Simulink streaming process, while all of the other data was saved as it was streamed.

[1] Software developed by Quanser

3.5 Experimental Procedure

For each experimental trial the procedure outlined below was used. The feet are initially locked together to zero the encoders, thereby using $\alpha = 0$ as the initial inner leg reference angle. All trials were recorded with an HD video camera. The inclinometer angle was zeroed to the ramp normal. The encoder angles were used to zero the inclinometer angle by standing the walker on the ramp for 20 seconds. For the trials completed, the foot offset was set to $\delta = 0$, therefore when the walker is standing still on the ramp, the inclinometer angle should read half the inner leg angle $\left(\pm\frac{\alpha}{2}\right)$. A successful run down the ramp was counted if the walker made it at least ten steps or half way down the ramp, which ever was longer. Once ten successful runs down the ramp were made, the trial was ended.

Experimental Trial Procedure:

1. Put a rod through the feet bolt holes to lock the legs together.
2. Start the video capture.
3. Start the data acquisition system.
4. Place the walker standing on the ramp for 20 seconds to calibrate the inclinometer.
5. Continue with trial until ten successful runs are completed.
6. Stop the data acquisition system
7. Stop the video capture.

The aim of the experimental trials was to determine the effect of the center of mass on the gait. Six trials, labeled L#1 to L#6, with a center of mass ranging from 32.72% to 55.83% measured from the hip were planned. The different center of mass values were obtained by moving the leg masses to six different locations. The varied parameters of the trials are shown in Table 3.3. When moving the leg masses, the radius of gyration was changed slightly. The radius of gyration changed from 25.75% to 28.77%.

Table 3.3: VARIABLE TRIAL PARAMETERS.

Trial	Center of Mass b		Radius of Gyration r_g	
	[m]	b/l	[m]	r_g/l
L#1	0.1356	32.72%	0.1192	28.77%
L#2	0.1547	37.34%	0.1112	27.03%
L#3	0.1739	41.96%	0.1077	26.00%
L#4	0.1930	46.58%	0.1067	25.75%
L#5	0.2122	51.21%	0.1091	26.32%
L#6	0.2313	55.83%	0.1146	27.65%

3.6 Data Processing and Analysis

After the trials were completed the data was processed using a post-processing program developed in Matlab. The data post-processing program was improved from a previous version used in [28]. At least two steps were removed from the beginning and end of each run down the ramp. If the step length and step period had not settled after two steps, more steps were removed. A moving window partial Fourier series was used to fit the inner leg angle and determine the first and second derivatives of the inner leg angle. The moving window was set at $1/16$ of the step period and only one set of the series was used. An overview of the post-processing program is given below.

Post-Processing Program:

1. Load trial data.
2. Calibrate inclinometer to ramp normal.
3. Initial scan for usable data using the following criteria:
   (a) Oscillations of α with period of 0.3 to 1.0 seconds.
   (b) Minimum amplitude of $\alpha = 20°$.
   (c) At least four steps (i.e. four peaks).
4. Prompt user to verify found data and ignored data section by section.
5. Prompt user on number of steps to remove from each trial. The step period and step length of each trial is shown.

6. Prompt user to save data selection.
7. Determine the gait data: Step period, step length, and average hip velocity.
8. Smooth data with a curve fit algorithm.
9. Save post-processed data.

Chapter 4

Stability Analysis

4.1 Introduction

This section provides an explanation on how to calculate the Lyapunov characteristic exponents of the ten dimensional passive walking mathematical model. The stability of a ten dimensional system is difficult to quantify. However, an attempt is made to understand the stability by determining the basins of attraction of the stable walking cycle. A novel method was developed to determine the basin of attraction of the 2D projection of a system.

4.2 Lyapunov Exponents

Lyapunov exponents are a valuable tool for analyzing the behaviour of non-linear systems. Specifically Lyapunov exponents can be described as the "average exponential rates of divergence or convergence of nearby orbits in phase space." [29]. For a continuous n-dimensional phase space, the Lyapunov exponents describe the long-term evolution of an infinitesimal n-(hyper)sphere of initial conditions. An n-dimensional system will have n Lyapunov exponents. Over a period of time the n-sphere will deform and become an n-(hyper)ellipsoid, contracting and expanding along different axes. Due to this contraction and expansion, the i^{th} Lyapunov exponent does not relate to the i^{th} state in the phase space, but the Lyapunov exponent spectrum relates to the system as a whole. Lyapunov exponents are invariant of the trajectory used to calculate the Lyapunov exponents. In other words, Lyapunov exponents are independent of initial conditions, if in the same basin of attraction. The Lyapunov exponent spectrum is given by (4.1), where Z_i is the length of the i^{th} principle axis of the n-(hyper)ellipsoid.

$$\lambda_i = \lim_{t\to\infty} \lim_{Z_i(0)\to 0} \frac{1}{t} \ln \frac{||Z_i(t)||}{||Z_i(0)||} \tag{4.1}$$

The signs of the Lyapunov exponents of a system provide information about the qualitative properties of a system. For a three dimensional system the possible Lyapunov exponent spectra are (+ve, 0, -ve) for a strange attractor, (0, 0, -ve) for a two-torus, (0, -ve, -ve) for a limit cycle, and (-ve, -ve, -ve) for a fixed point.

4.2.1 Calculating Lyapunov Exponents

There are different methods that have been developed for computing Lyapunov exponents. The method developed by [29] will be explained. With the method developed by [29], to compute Lyapunov exponents a "fiducial" trajectory is selected as the center of the n-sphere, where the motion of the "fiducial" trajectory is defined by the non-linear equations. The trajectories of the points on the surface of the sphere, which are infinitesimally separated from the center, are defined by the linearized equations. The non-linear and linear equations are described by (4.2). Ψ is the state transition matrix of the linearized equations and describes the evolution of the n-sphere. J is the linearized system of equations. Figure 4.1 shows a depiction of how the system evolves in time.

$$\begin{Bmatrix} \dot{y} \\ \dot{\Psi} \end{Bmatrix} = \begin{Bmatrix} f(y(t)) \\ J(y(t))\Psi \end{Bmatrix} \tag{4.2}$$

$$\Psi = \begin{bmatrix} \nu_1^T & \nu_2^T & \dots & \nu_n^T \end{bmatrix} \tag{4.3}$$

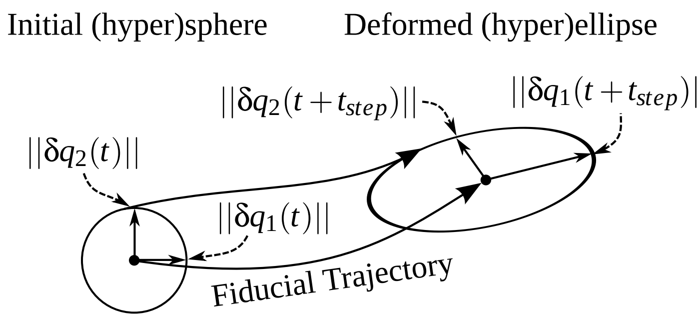

Figure 4.1: A visualization of the time evolution of the initial infinitesimal sphere in 2D.

The Lyapunov exponents are derived of the time evolution of the volume of the n-ellipsoid defined by $[\nu_1, \nu_2, \dots \nu_n]$. However, the vectors $[\nu_1, \nu_2, \dots \nu_n]$ tend to align as $t \to \infty$ making the volume difficult to accurately compute. Therefore, the vectors are orthonormalized during the integration. Figure 4.2 shows a depiction of orthonormalization about the vector ν_1.

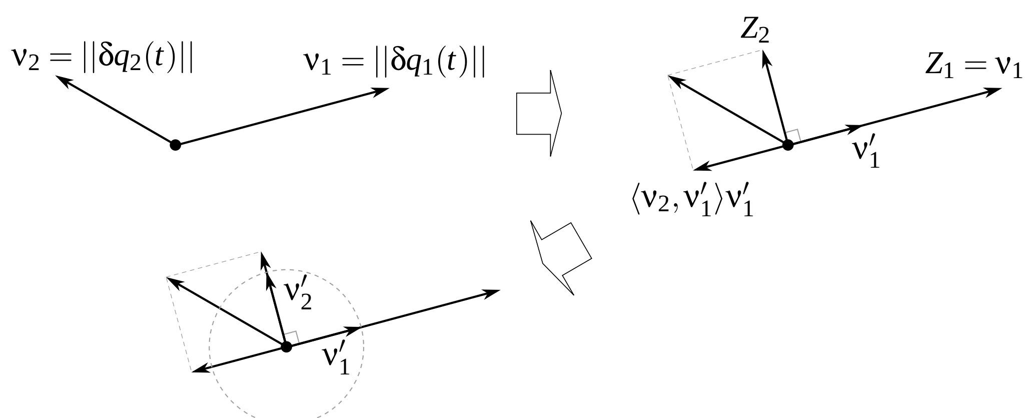

Figure 4.2: The GSR procedure for a set of 2D vectors

The Gram-Schmidt reorthonormalization (GSR) procedure is used to orthonormalize the state vectors.

$$Z_1 = \nu_1 \tag{4.4}$$

$$Z_2 = \nu_2 - \langle \nu_2, \nu_1' \rangle \nu_1' \tag{4.5}$$

$$\vdots \tag{4.6}$$

$$Z_n = \nu_n - \langle \nu_n, \nu_{n-1}' \rangle \nu_{n-1}' - \ldots - \langle \nu_2, \nu_1' \rangle \nu_1' \tag{4.7}$$

$$\nu_i' = \frac{Z_i}{||Z_i||} \tag{4.8}$$

An arbitrary initial vector set can be chosen since the set of ν_i tend to align with the direction of λ_1 and the GSR has orientation preserving properties. Therefore the initial vector set is chosen to be $\Psi = I$, where I is an identity matrix. The algorithm for determining the Lyapunov exponents is shown below.

Lyapunov Exponents Algorithm

Initial conditions: y_0 and $\Psi_0 = I$.

Main Loop: starting at t_0 and moving forward by t_{step}. From an ODE solver with $(time|t : t + t_{step})$ yields the evolution of the fiducial trajectory y and the n-ellipsoid Ψ.

$$\begin{bmatrix} \nu_1^T & \nu_2^T & \ldots & \nu_n^T \end{bmatrix} = \Psi_{time=t+t_{step}}$$

$$Z_1(t) = \nu_1$$

$$Z_2(t) = \nu_2 - \langle \nu_2, \nu_1' \rangle \nu_1'$$

$$\vdots$$

$$Z_n(t) = \nu_n - \langle \nu_n, \nu_{n-1}' \rangle \nu_{n-1}' - \ldots - \langle \nu_2, \nu_1' \rangle \nu_1'$$

Where

$$\nu_i' = \frac{Z_i(t)}{||Z_i(t)||}$$

$$C_i(t+t_{step}) = C_i(t) + \frac{\ln(||Z_i||)}{\ln(2)} \tag{4.9}$$

$$\lambda_i(t+t_{step}) = \frac{C_i(t+t_{step})}{t-t_0}$$

$$t = t + t_{step}$$

$$y_0 = y|_{time=t+t_{step}}$$

$$\Psi_0 = \begin{bmatrix} \nu_1'^T & \nu_2'^T & \dots & \nu_n'^T \end{bmatrix}$$

End of Loop

As $t \to \infty$ the value of $\lambda_i(t)$ will converge to λ_i.

4.2.2 LuGre Model Approximation

To calculate the Lyapunov characteristic exponents of the ten dimension state space of the proposed mathematical model, the method outlined in [29] was used. The method outlined in [29] requires the Jacobian of the equations of motion. To calculate the Jacobian of the equations of motion an approximation of the LuGre model is required. The derivative of the bristle deflection, $\dot{z}$, of the LuGre model is partially a function of the absolute value of the sliding velocity between the two surfaces. The derivative of an absolute value at zero is undefined. Therefore, a smooth approximation to the absolute value was substituted based on the information in [30]. The original system, (4.10), is approximated by (4.11).

$$\dot{z} = v - \sigma_0 \frac{|v|}{g(v)} z \tag{4.10}$$

$$\dot{\hat{z}} = S_v^2 v - \sigma_0 \frac{S_v v}{g(v)} z \tag{4.11}$$

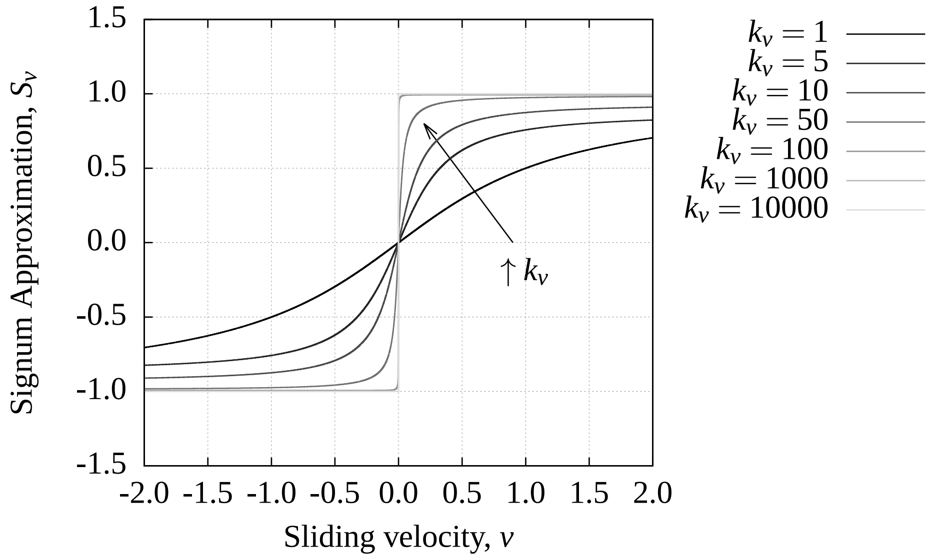

Figure 4.3: Signum approximation function - $S_v = \frac{2}{\pi}\arctan(k_v v)$.

Where the signum function is approximated by (4.12). Fig. 4.3 illustrates how the parameter k_v effects the approximation function.

$$S_v = \frac{2}{\pi}\arctan(k_v v) \tag{4.12}$$

The value k_v is a tuning parameter that was set to $k_v = 10^8$. The value of k_v was selected by choosing the smallest value that had a negligible effect on the solution. As $k_v \to \infty$ the function S_v approaches the signum function. The derivative of the smooth approximation, (4.14), has an extra term compared to the derivative of the original equation, (4.13).

$$\frac{\partial \dot{z}}{\partial v} = 1 - \sigma_0 \frac{\frac{v}{|v|}}{g(v)} z \left(1 + 2\left(\frac{v}{v_s}\right)^2 \left(1 - \frac{\mu_c}{g(v)}\right)\right) \tag{4.13}$$

$$\begin{aligned} \frac{\partial \dot{\tilde{z}}}{\partial v} &= S_v^2 - \sigma_0 \frac{S_v}{g(v)} z \left(1 + 2\left(\frac{v}{v_s}\right)^2 \left(1 - \frac{\mu_c}{g(v)}\right)\right) \\ &\quad + \frac{2}{\pi}\left(\frac{k_v v}{1 + (k_v v)^2}\right)\left(2S_v - \frac{\sigma_0}{g(v)} z\right) \end{aligned} \tag{4.14}$$

However, the extra term tends towards zero as $k_v \to \infty$. The Jacobian of the system with the approximation can be found in Appendix A.2.

4.3 Basin of Attraction

A stable attractor of a dynamic system is a point, orbit, or region of the state space, that nearby trajectories will tend towards. All trajectories that tend toward an attractor make up a region of space called the basin of attraction. Each attractor has its own basin of attraction. When the passive walker reaches a stable gait, the passive walker is in a stable periodic orbit, where the periodic orbit is an attractor. The mathematical model of the passive walker is a ten dimensional state system. Trying to map out a ten dimensional state space basin of attraction is computationally demanding. Therefore, for this thesis, the basin of attraction was determined for a 2D projection of the ten state system.

The size and shape of the basin of attraction is used to quantify the stability of the passive walker. The basin of attraction at discrete points on the gait were calculated for two parameters. Eight points were selected on a leg angle phase portrait. These eight points are referred to as "Points of Interest" (POI) and are shown in Fig. 4.4 and listed in Table 4.1. The basin of attraction of the leg angle, and leg angle velocity was determined for each POI.

Table 4.1: POINTS OF INTEREST ALONG THE PHASE PORTRAIT.

POI	1	2	3	4	5	6	7	8
Marker	$\dot{\theta}_1 = 0$	$\theta_1 = 0$	$\theta_2 = 0$	$\dot{\theta}_1 = 0$	$\dot{\theta}_2 = 0$	$\theta_2 = 0$	$\theta_1 = 0$	$\dot{\theta}_2 = 0$
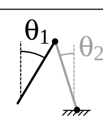	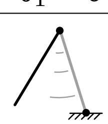	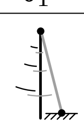	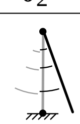	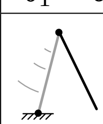	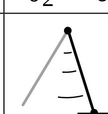	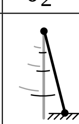	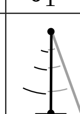	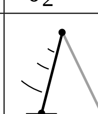
Stance Leg	Leg 2				Leg 1			

During the stance phase, if the leg angle (θ) or leg angle velocity $(\dot{\theta})$ are changed, the leg could be rotated into the ground. Therefore, during the stance phase, the states x_{hip},

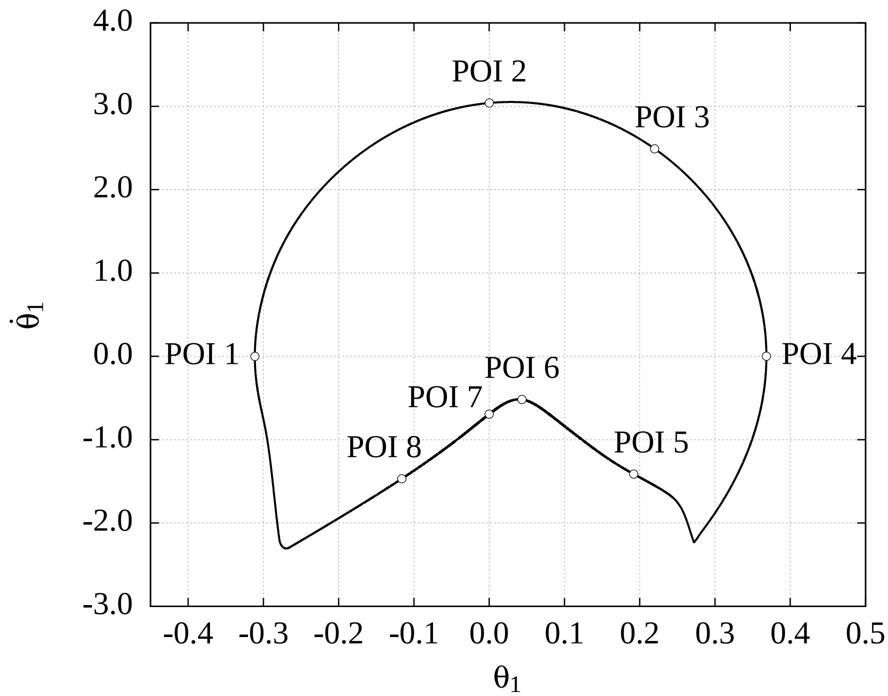

Figure 4.4: Phase portrait of the leg angle with points of interest labeled.

y_{hip}, $\dot{x}$, $\dot{y}$, were changed to create an equivalent change in θ and $\dot{\theta}$ so that the same contact forces were produced compared to the original state.

$$\theta_s^* = \theta_s + \varepsilon_1 \tag{4.15}$$

$$\dot{\theta}_s^* = \dot{\theta}_s + \varepsilon_2 \tag{4.16}$$

$$y^* = y - l(\cos\theta_s - \cos\theta_s^*) + \rho(\cos(\theta_s - \delta) - \cos(\theta_s^* - \delta)) \tag{4.17}$$

$$\begin{aligned}\dot{x}^* = \dot{x} + \dot{(\theta)}_s(l(\cos\theta_s - \cos\theta_s^*) - \rho(\cos(\theta_s - \delta) - \cos(\theta_s^* - \delta))) \\ - \varepsilon_2(l\cos\theta_s^* - \rho\cos(\theta_s^* - \delta) + \rho)\end{aligned} \tag{4.18}$$

$$\begin{aligned}\dot{y}^* = \dot{y} + \dot{(\theta)}_s(l(\sin\theta_s - \sin\theta_s^*) - \rho(\sin(\theta_s - \delta) - \sin(\theta_s^* - \delta))) \\ - \varepsilon_2(l\sin\theta_s^* - \rho\sin(\theta_s^* 1 - \delta))\end{aligned} \tag{4.19}$$

```
cross_over = false;
last_point = stable; /* First point is the equilibrium point.                 */
while abs(ε − ε0*)/2 > step_min and cross_over == true do
    point = function_test(stable or unstable);
    if point == stable then
        if cross_over == false or last_point == stable then
            ε0 = ε;
            ε = 2ε;
        else
            ε0* = ε0; /* Place Holder                                          */
            ε0 = ε;
            ε = ε + abs(ε − ε0*)/2;
            cross_over = true;
        end
        last_point = stable;
    else
        if cross_over == false or last_point == unstable then
            ε0 = ε;
            ε = ε/2;
        else
            ε0* = ε0; /* Place Holder                                          */
            ε0 = ε;
            ε = ε − abs(ε − ε0*)/2;
            cross_over = true;
        end
        last_point = unstable;
    end
end
```

Algorithm 1: Edge point with binary search method.

4.3.1 BoA Edge Algorithm

To calculate a 2D projection of the basin of attraction (BoA) a simple grid search can be performed, where each parameter combination is tested to see if the initial condition is stable or unstable[1]. However, a grid search is inefficient, and depending on the resolution, the grid search can take a very long time. As well, if the grid search is not fine enough, some of the BoA may not be found. Therefore, a new method was developed to find the

[1] i.e. Will eventually reach the attractor.

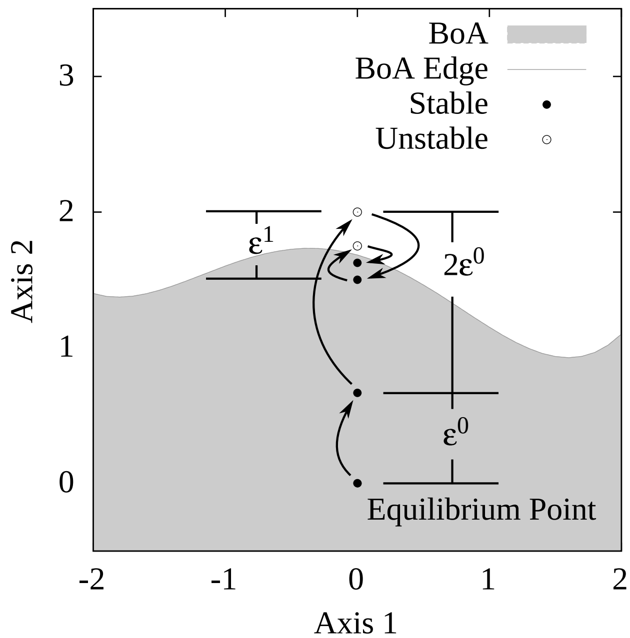

Figure 4.5: BoA algorithm - finding first point

BoA edge. The BoA edge algorithm finds the edge of non-riddled basins of attraction surround the stable point. Below, a step by step explanation of the algorithm is provided.

Step 1: Find the first point on the BoA

Starting from the stable initial point, the algorithm searches for the edge of the BoA in the positive direction of axis 2. To find the edge a binary search method is used. The algorithm for the binary search method is shown in algorithm 1. Fig. 4.5 shows a visual example of the algorithm finding the first point of the BoA edge. Initially, if the first guess is stable, the offset will double until the algorithm finds an unstable point. Alternatively, if the first guess is unstable, the algorithm will half the offset until a stable point is found. Once the algorithm has crossed the BoA edge, the binary search method is employed, where the next guess is the halfway point between the closest stable and unstable point. This method is repeated until the step size[2] is below a set minimum, noted as *step_min* in the pseudo code.

[2]difference between the next guess and current guess

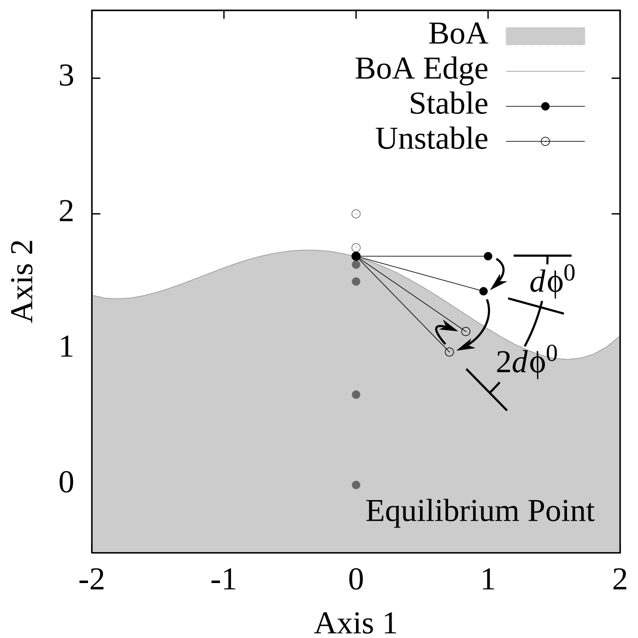

Figure 4.6: BoA edge algorithm - finding first edge

Step 2: Find the next edge on the BoA

The first edge of the BoA is found in the positive direction of axis 1. The algorithm searches using a set radius and varies the angle using the same binary search method shown in algorithm 1. Fig. 4.6 shows a visual example of the algorithm find the first edge of the BoA. The algorithm searches clockwise around the BoA edge, thus if an unstable point is found the algorithm rotates the search arm in the clockwise direction and counterclockwise for a stable point.

There are several checks in place to make sure the algorithm is finding the full BoA. If the algorithm cannot find the BoA edge within an obtuse angle from the previous line, the algorithm goes into a reverse protocol. The reverse protocol searches with a finer resolution and attempts to avoid skipping part of the BoA, like the example shown in Fig. 4.7. Also, if the algorithm crosses itself then it follows a backtracking protocol, where the algorithm backs up and decreases the increment amount. Every time the algorithm crosses it self the algorithm backs up more and further decreases the increase increment. The initial guess for the next angle is determined by using a curve fit of the previously found points, where

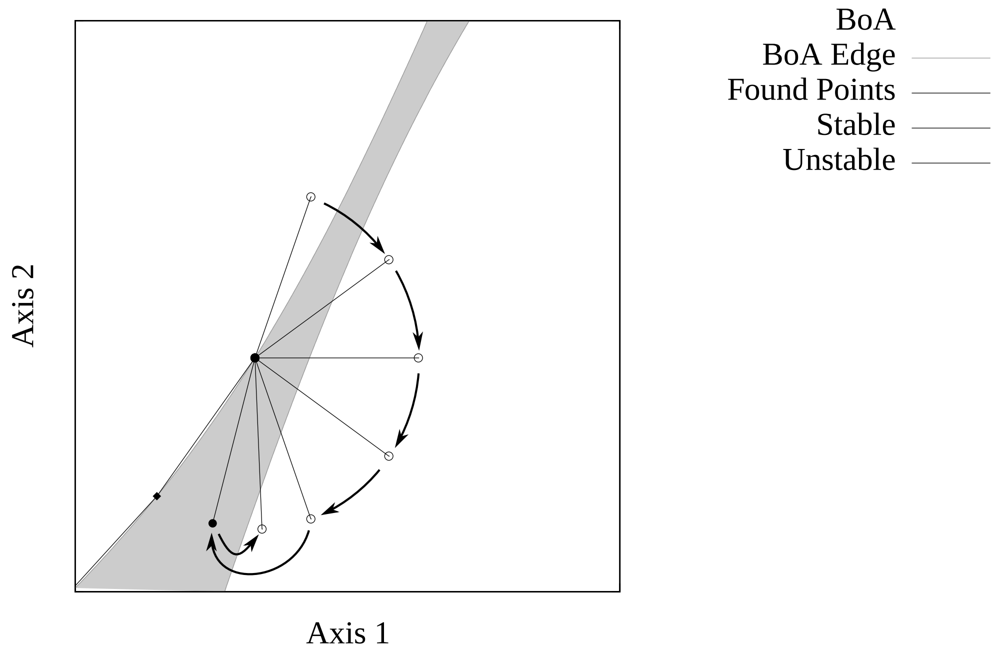

Figure 4.7: An example without the reverse protocol, where part of the BoA is skipped.

the algorithm attempts to find a curve that will best approximate the last known point using the previous points. The algorithm starts with two points, and increases up to maximum of 20 and starts at a straight line and moves to a polynomial curve fit. If the algorithm cannot find a reasonable guess, the algorithm reverts to using the last angle as the initial guess for the next angle.

Fig. 4.8 shows the performance of the algorithm with a test function (4.21)–(4.22), where $c = 0.77$ and $d = 15$. The test function was created with acute angles to test the reverse protocol and backtracking protocol. The algorithm took 872 evaluations to determine the edge of the test function with a relative angular error of 10^{-2}. A cell map of 900 evaluations is shown in comparison to the algorithm's solution in Fig. 4.8.

$$0 < \phi < 2\pi \tag{4.20}$$

$$x = -\cos(\phi + c) \tag{4.21}$$

$$y = -\sin(\phi)\sin^5\left(\frac{\phi}{2}\right)\left(d + \operatorname{sgn}\left(\sin(\phi)\sin^5\left(\frac{\phi}{2}\right)(d-1)\right)\right) \tag{4.22}$$

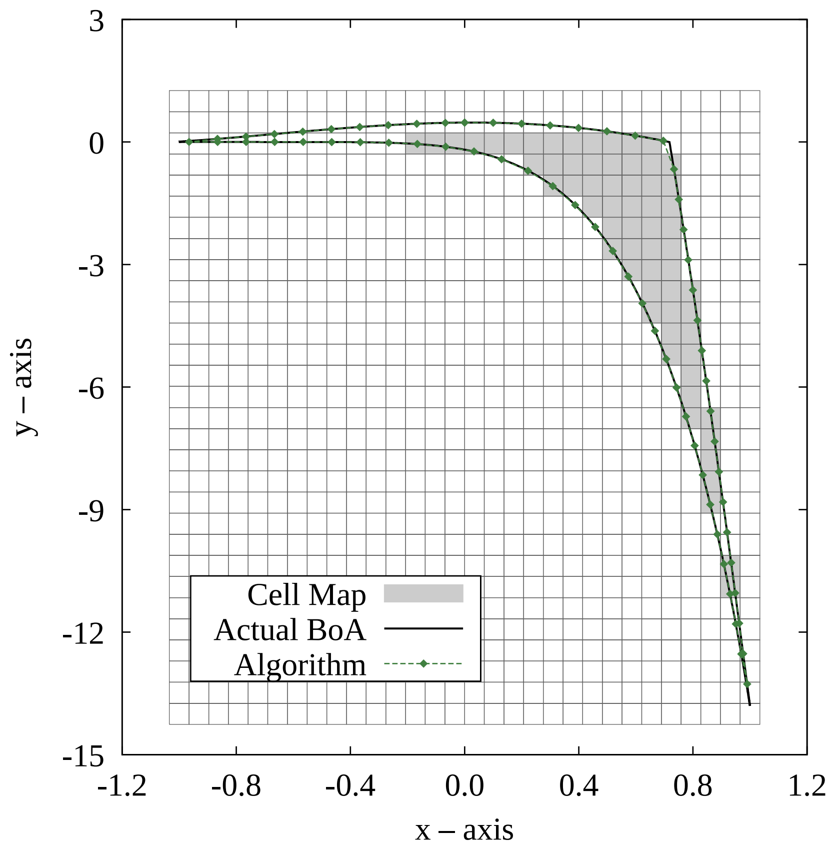

Figure 4.8: Algorithm vs cell map using a test curve.

4.4 Summary

This chapter introduced the concept of Lyapunov exponents and explained some of the properties of Lyapunov exponents. A review of the method to calculate Lyapunov exponents found in [29], was given. The method to calculate the Lyapunov exponents is based on the numerical solution of the original ODE and the linearize version of the ODE. A novel method for finding the edge of non-riddled basins of attraction was explained. The method was compared to a simple grid search algorithm.

Chapter 5

Results and Discussion

5.1 Introduction

The proposed passive walking mathematical model was able to produce stable walking motion. With simulation results of the proposed passive walking mathematical model some of the advantages of the proposed model are explained. Trials with the physical passive walker, HM2L, were completed with six different center of mass locations. The gait parameters of the proposed passive walking mathematical model and the impact-based passive walking model were compared to the gait measurements of the physical passive walker. The stability and robustness of passive dynamic walking was analyzed with the proposed mathematical model. Lyapunov exponents of the proposed passive walking mathematical mode were calculated for one case. The basin of attraction edge algorithm was used to determine the BoA of the proposed passive walking mathematical model. The area of the BoA is used to quantify the robustness of the passive walker and is analyzed against the change in angular momentum of the passive walker. As well, the proposed passive walking mathematical model is simulated with human like parameters and the angular momentum of the resulting gait is discussed in comparison to the angular momentum measured from human gaits.

5.2 Proposed Mathematical Model

The proposed mathematical model is able to capture more complex dynamics, like the double support phase, compared to the impact-based passive walking model. With the added complexity of the contact force models, stable solutions of the proposed model were still found. Finding stable initial conditions for passive walking models is not an easy task. Unfortunately for those readers trying to find initial conditions of their own, mostly intuition was used to find the first initial conditions. However, there are some tricks to finding initial conditions. If the initial conditions are close to stable initial conditions the walker will usually oscillate from a small step to a big step. Thus if the first step was too big, reduce the swing leg velocity or increase the stance leg velocity to reduce the step size and vice versa for a small step. Another trick is to choose parameters that produce a more robust walker, like a larger hip mass. Once a set of stable initial conditions are found, to find stable conditions for other parameter combinations, offset the desired parameter from the first parameter set slightly. Then simulate the new parameter set until the simulation stabilizes. If the simulation does not stabilize then reduce the offset. If the simulation does stabilize then offset the parameter again, repeat until the desired parameter is reached.

To demonstrate some of the advantages of the proposed model, simulations were conducted with the parameters shown in Table 5.1. For comparison, simulations of the traditional impact-based passive walking model were completed with model parameters of Table 5.1. The initial conditions of the proposed passive walking model (5.1) and the impact-based passive walking model (5.2) were selected so that the system was already in a stable gait.

Proposed Passive Walking Mathematical Model

$$\begin{aligned} Q_0 = \big[&0.000 \quad 0.4114 \quad 0.1399 \quad 0.0512 \quad 0.1708 \\ &0.0048 \quad 2.8056 \quad -0.4126 \quad 3.000\times10^{-6} \quad 0.493\times10^{-6}\big]^T \end{aligned} \tag{5.1}$$

Impact-Based Passive Walking Mathematical Model

$$Q_0 = \begin{bmatrix} 0.2414 & -0.2414 & -1.7314 & -0.7318 \end{bmatrix}^T \tag{5.2}$$

Table 5.1: WALKER SIMULATION PARAMETERS.

Model Parameters

l	$=$	0.4143	$[m]$	ρ	$=$	0.0860	$[m]$
δ	$=$	0°	$[degrees]$	γ	$=$	2.05°	$[degrees]$
m	$=$	5.1587	$[kg]$	M	$=$	1.2826	$[kg]$
b	$=$	0.1930	$[m]$	r_g	$=$	0.1067	$[m]$

Contact Parameters

μ_s	$=$	0.38		μ_c	$=$	0.30	
k_s	$=$	9.3920×10^5	$[N/m^{3/2}]$	k_d	$=$	1.6879×10^7	$[N\,s/m^{5/2}]$
σ_0	$=$	10^5	$[N/m]$	σ_1	$=$	$2\sqrt{\sigma_0}$	$[N\,s/m]$
v_s	$=$	10^-4	$[m/s]$	α^0	$=$	10°	

Fig. 5.1a) shows the stable phase portrait of a leg angle versus leg angle velocity of the proposed model. The heel strike regions are highlighted in red and the double support phase is highlighted in dark red with a thicker line in Fig. 5.1a). Fig. 5.1b) shows the stable phase portrait of the a leg angle of the standard impact model. The standard impact model heel strike regions are vertical since the position state does not change over the impact. With the Hunt-Crossley contact model and the LuGre friction model the position states change during the impact event, as they would in reality. As well, the contact and friction model allow the system to slide during the impact event (i.e. no sliding during impact is *not* assumed), if the tangential force is great enough to overcome the contact friction force.

Fig. 5.2 shows the normal force and friction force for one foot over one step. The initial peak in the normal force plot is due to the impact of the foot with the ramp. After the impact

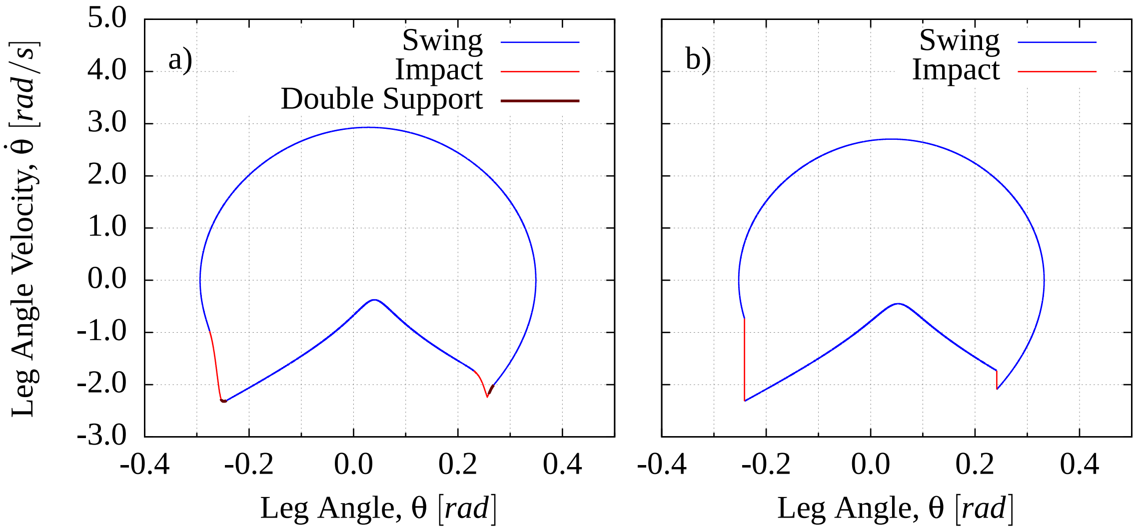

Figure 5.1: Leg angle phase portrait a) proposed mathematical model b) impact-based mathematical model.

phase the normal force settles to a value near the steady state normal force $(M+2m)g$. The contact force still varies after the impact phase due to the movement of the legs. During the impact phase, the friction force suddenly decreases when the foot stops sliding. The friction direction reverses twice through out a single step. The second reversal is due to the foot dragging at lift off.

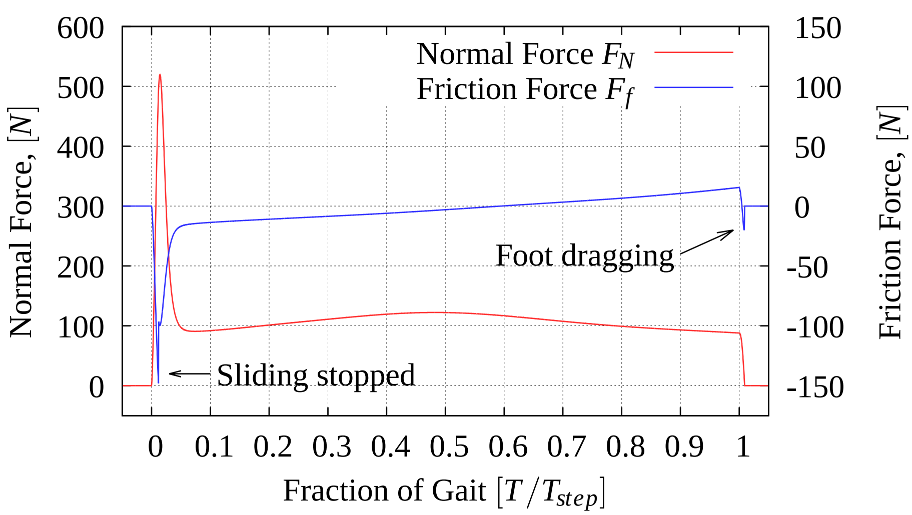

Figure 5.2: Normal and friction force vs time.

Fig. 5.3 shows the friction state z for one leg over two steps. Notice how the state observer is still active during non-contact sections of the gait. Simulations were completed with reseting the state observer to zero after each separation and no discernible difference was found between the resulting gaits. Therefore the equation for z was kept continuous through out the whole simulation.

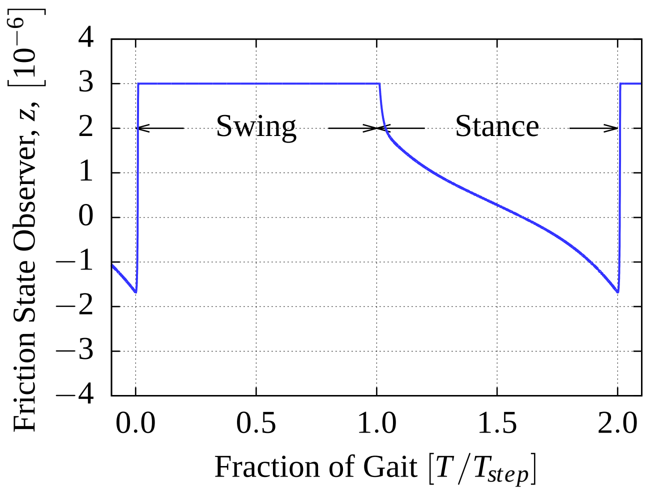

Figure 5.3: Friction state observer.

5.3 Physical Walker and Gait Measurement Performance

The physical passive walker, HM2L, was able to walk down a 32 foot long ramp. The design proved to be rigid and reliable. The ramp design was rigid, but to adjust the ramp took about thirty minutes to adjust the ramp to a desired angle. The data acquisition system worked well with one exception. The inclinometer was found to have some issues that prevented useful data from being captured. A US Digital X3M inclinometer was used to measure the global orientation of the experimental walker. The X3M uses MEMS accelerometers to determine the orientation of the sensor, which when subject to vibration from each heel strike gave a noisy signal. With the exception of the inclinometer, the gait measurement system performed very well.

5.4 Mathematical Model Validation

In this section the validation of the mathematical model is provided against experimental data gathered using the passive walker HM2L. As a reference, the impact-based passive walking model is compared against the experimental data as well. The effects of changing the center of mass on the step period, step length, and average hip velocity is used to compare the three resulting gaits. The parameters used in the simulations for the validation case, rounded to four decimal spaces, can be found in Table 5.2 and Table 5.3. The geometric parameters were determined from the SolidWorks model that was used to generate the machine shop drawings for the passive walker HM2L. Each machined part, bolt, and nut of the walker was weighed and the corresponding mass was entered in the SolidWorks model. Assuming a uniform density for each part, bolt, and nut, the mass properties of the walker were determined. To measure the angle of the ramp, a laser level was used to first

Table 5.2: CONSTANT TRIAL PARAMETERS.

		Model Parameters Parameters					
l	$=$	0.4143	$[m]$	ρ	$=$	0.0860	$[m]$
δ	$=$	0°	$[degrees]$	γ	$=$	2.05°	$[degrees]$
m	$=$	5.1587	$[kg]$	M	$=$	1.2826	$[kg]$
		Contact Parameters					
μ_s	$=$	0.38		μ_c	$=$	0.30	
k_s	$=$	9.3920×10^5	$[N/m^{3/2}]$	k_d	$=$	1.6879×10^7	$[N s/m^{5/2}]$
σ_0	$=$	10^5	$[N/m]$	σ_1	$=$	$2\sqrt{\sigma_0}$	$[N s/m]$
v_s	$=$	$10^{-}4$	$[m/s]$	α^0	$=$	10°	

Table 5.3: VARIABLE TRIAL PARAMETERS.

Trial	Center of Mass b		Radius of Gyration r_g	
	[m]	b/l	[m]	r_g/l
L#1	0.1356	32.72%	0.1192	28.77%
L#2	0.1547	37.34%	0.1112	27.03%
L#3	0.1739	41.96%	0.1077	26.00%
L#4	0.1930	46.58%	0.1067	25.75%
L#5	0.2122	51.21%	0.1091	26.32%
L#6	0.2313	55.83%	0.1146	27.65%

measure the topography of the floor. Then, using the floor as a reference, the relative height of four locations on the ramp were measured. Using the relative heights, the average angle of the ramp was determined.

The friction coefficients were estimated from measurements of a previous ramp and walker setup [28]. The parameters specific to the LuGre model (σ_0, σ_1, and v_s) were selected based on the information found in [31]. For the contact parameters, the steady state value of the deformation of the foot was measured when the walker was standing. Using the measured deflection and (5.3), the value of k_s was estimated. The contact damping parameter k_d was the only parameter that was used to adjust the model to fit the experimental data. The parameter k_d was adjusted so that the experimental step length of trial:CoM L#1 matched the simulations. The adjusted value of k_d was kept constant for the remaining simulations. For the simulations, only the center of mass and radius of gyration parameters were changed between trials to match the change of the parameters of the physical walker.

$$k_s = \left(\frac{1}{2}(2m+M)g\right) / (h_{measured})^{\frac{3}{2}} \tag{5.3}$$

Fig. 5.4a), Fig. 5.4b), and Fig. 5.4c) show the step length, step period, and average hip velocity for the proposed mathematical model, the impact model, and the experiments. The impact model was not stable at CoM L#6, but could take over 50 steps. The average of these steps was used and the standard deviation between the steps are shown in the figures. The experiments have two sets of standard deviation bars. The “All steps Stdv.” is the standard deviation of all of the usable steps of all of the runs down the ramp for that trial. The “Trial Stdv.” is the standard deviation of the averages of each run down the ramp for that trial. The simulations of the proposed mathematical model match the experiment in both magnitude and trend. Thus, the ability of the proposed model to generate gait measurement trends is valid. The impact–based model matches the trends of the experiments, but not as closely as the proposed mathematical model. Although the impact–based model may be valid in some cases, Fig. 5.4 shows the inability of the impact–based model to replicate reality in this case.

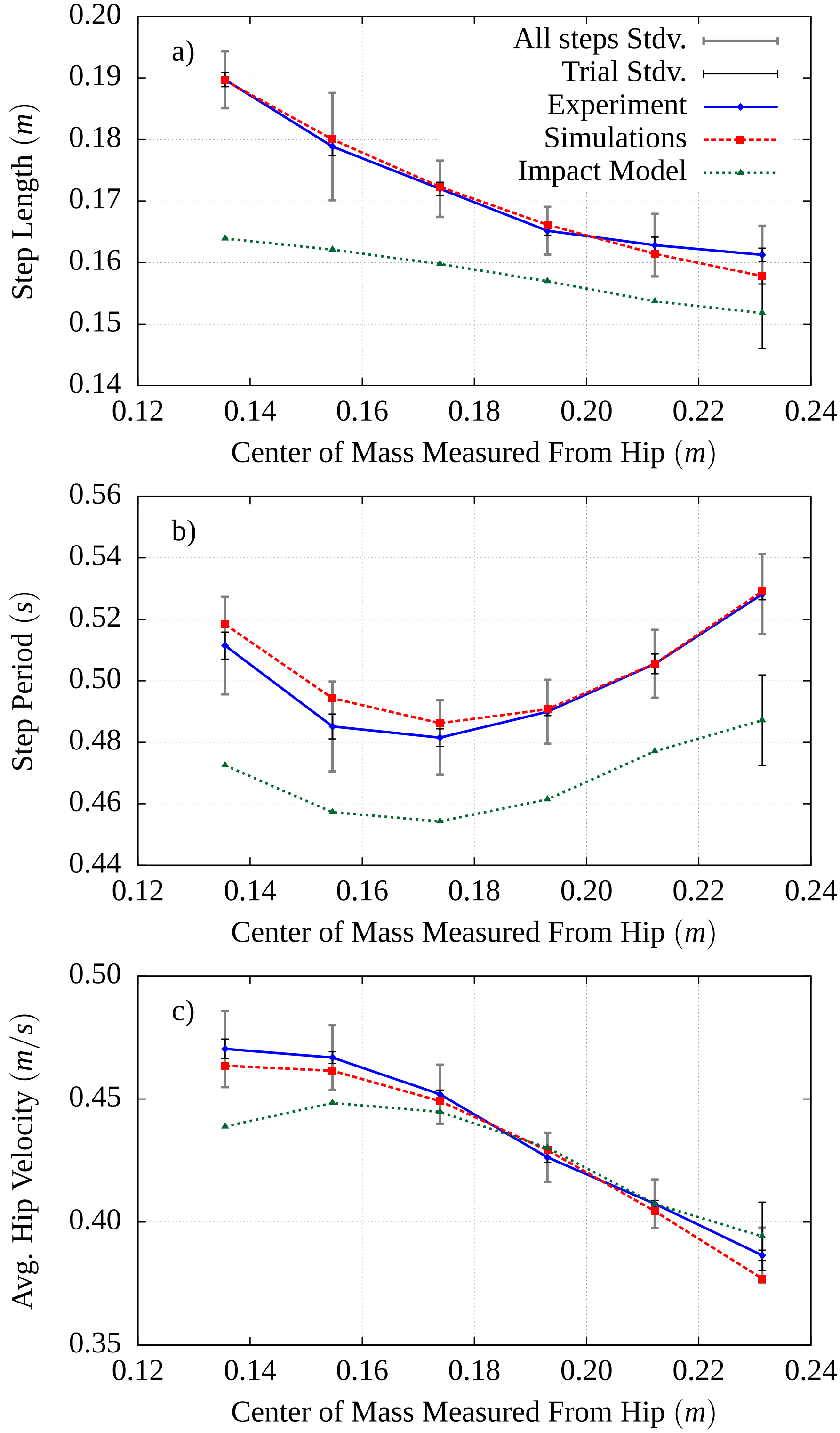

Figure 5.4: Experiment and simulation gait measurements versus center of mass measured from the hip: a) step length b) step period c) average hip velocity.

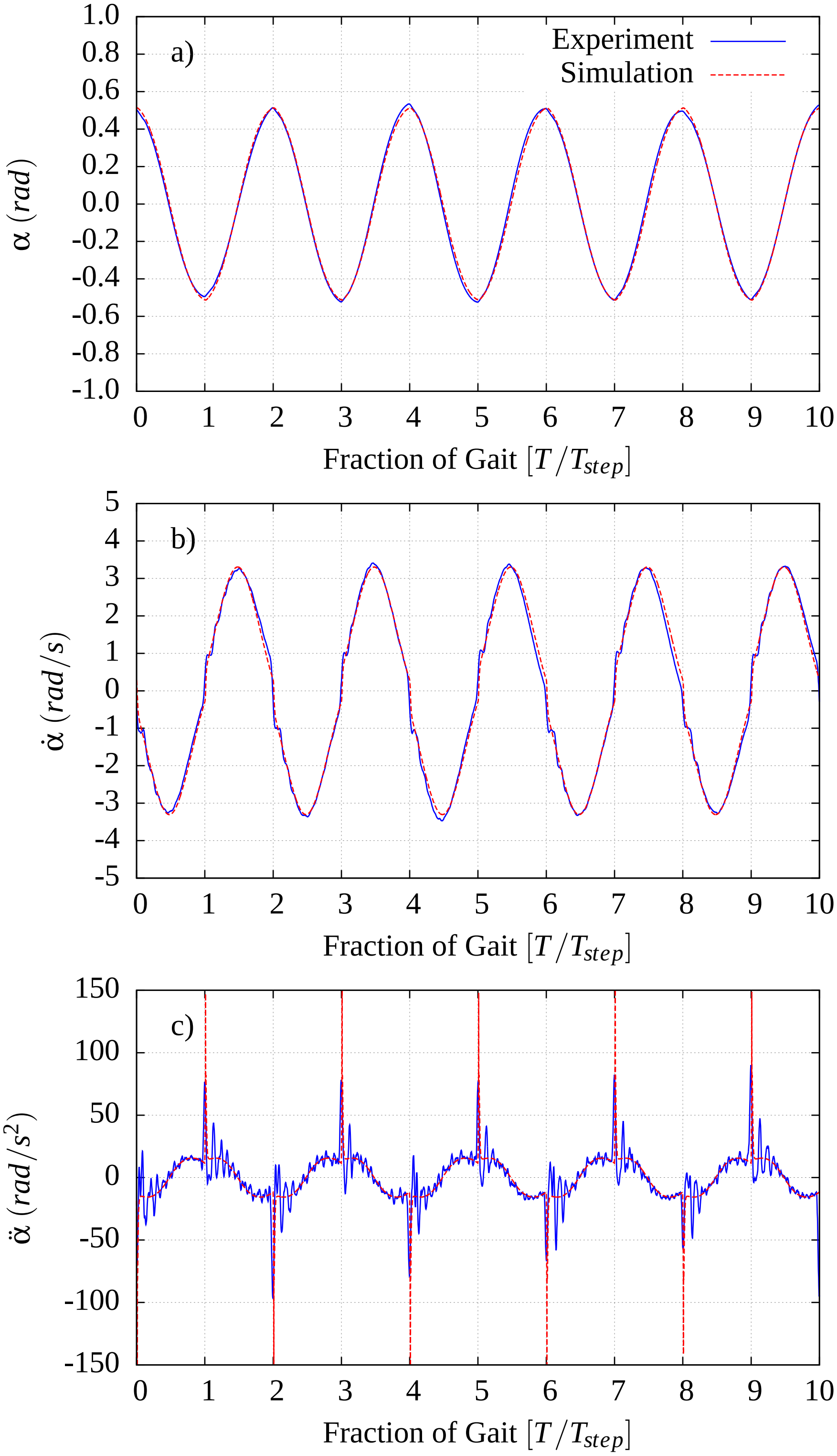

Figure 5.5: The kinematics of the physical walker and the proposed mathematical model: a) inner leg angle b) inner leg angle velocity c) inner leg angle acceleration.

Fig. 5.5a), Fig. 5.5b), and Fig. 5.5c) show a comparison of the kinematics of the simulations and experiments for CoM L#4. Comparing the kinematics goes one step further than comparing the resulting gait measurements and shows how well the proposed model can match the physical walker's motion. Fig. 5.5a) shows the inner leg angle, Fig. 5.5b) shows the inner leg angle velocity, and Fig. 5.5c) shows the inner leg angle acceleration. The inner leg angle data was fit using a Fourier series with a moving window. The derivative of the Fourier series was used to calculated the derivatives of the inner leg angle. With the inner leg angle acceleration, degradation of the signal is noticeable. However, the general shape and magnitude of the inner leg angle acceleration of the simulations and experiments are still in agreement. The agreement between the kinematics of the physical walker and the proposed mathematical model show that the proposed mathematical model can generate valid gait motion, not just valid gait measurement trends.

5.5 Stability Analysis Results

5.5.1 Lyapunov Exponents

The Lyapunov exponents were calculated for the proposed passive walking mathematical model for one case using the approximation to the LuGre model shown in section 4.2. To calculate the Lyapunov exponents for this single case took approximately one month to simulate. Some inefficiencies in the code were found afterward that may reduce the computation time. However, due to the long computation time, using Lyapunov exponents as a measure of stability proved to be unfeasible for this project. The sign of the Lyapunov exponents of this one case still provides some information about the gait. Fig. 5.6 shows the Lyapunov exponents calculated versus time with two close up views. To determine the final values of the Lyapunov exponents, an average of the Lyapunov exponents over the last 1000 seconds of the simulation was taken.

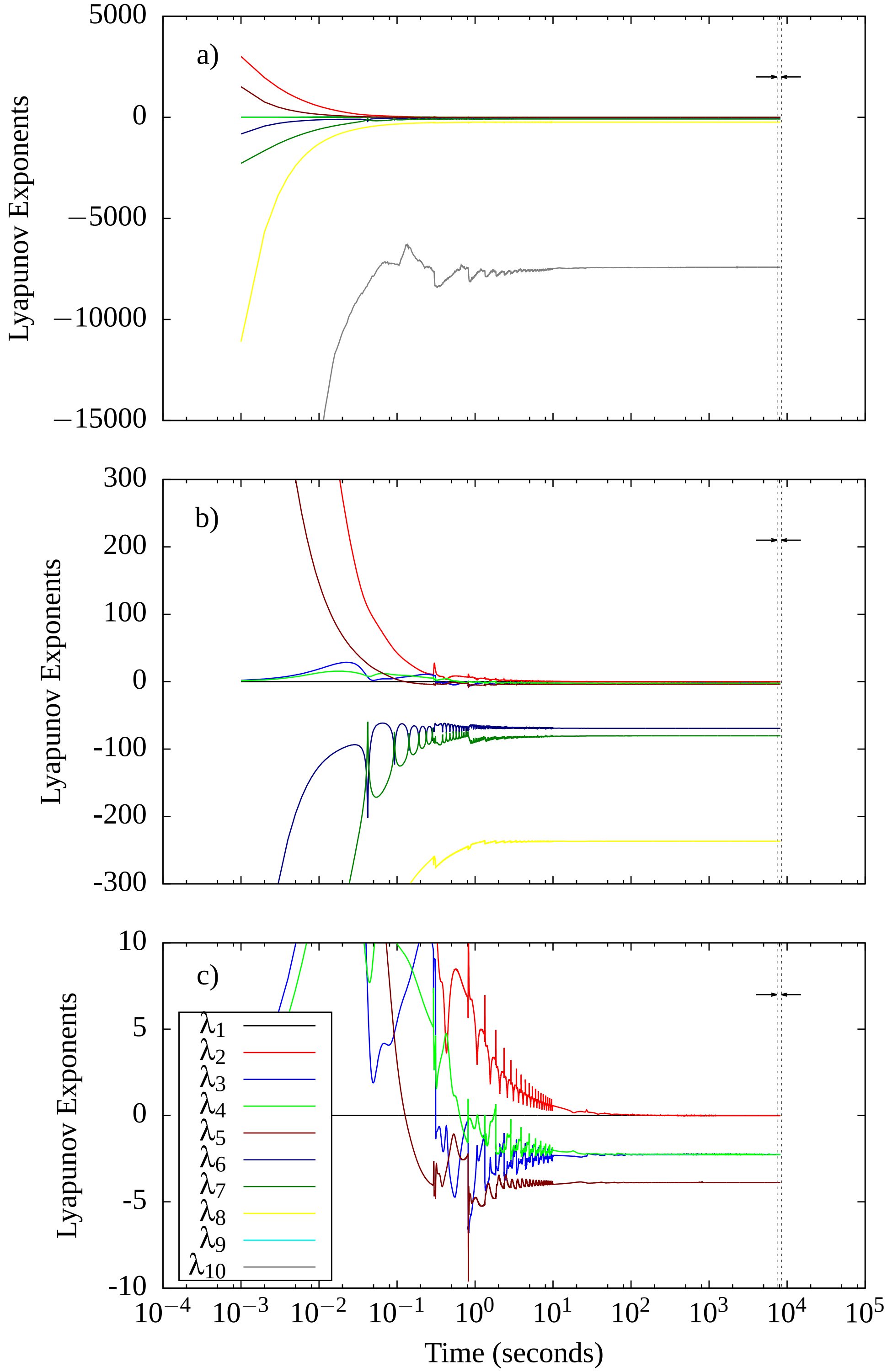

Figure 5.6: Lyapunov exponents vs time a) full view b) close up one c) close up two.

Table 5.4: LYAPUNOV CHARACTERISTIC EXPONENTS.

	LE		STD	% STD
1	0	$\pm$	0	0%
2	-0.01341	$\pm$	0.00013	0.97%
3	-2.25988	$\pm$	0.00018	7.97×10^{-3}%
4	-2.25958	$\pm$	0.00013	5.75×10^{-3}%
5	-3.88372	$\pm$	0.00008	2.06×10^{-3}%
6	-69.30363	$\pm$	0.00018	2.60×10^{-4}%
7	-80.29741	$\pm$	0.00024	2.99×10^{-4}%
8	-236.70207	$\pm$	0.00022	9.29×10^{-5}%
9	-29346.903	$\pm$	0.043	1.47×10^{-4}%
10	-7413.16	$\pm$	0.20	2.70×10^{-3}%

Table 5.4 gives the average calculated Lyapunov exponents over the last 1000 seconds ($T = 7450$ to 8450 seconds). The simulation had to run for longer due to exponent two (λ_2). The sign of exponent two (λ_2) was not determinable until near the end of the simulation. Fig. 5.7 shows the relative error between the current Lyapunov exponents and the Lyapunov exponents shown in Table 5.4. The sign of the Lyapunov exponents was found to be $(0,-,-,\ldots)$, which shows that the mathematical passive walking model is moving in a stable periodic motion not a higher dimensional torus $(0,\ldots,0,-,-,\ldots)$

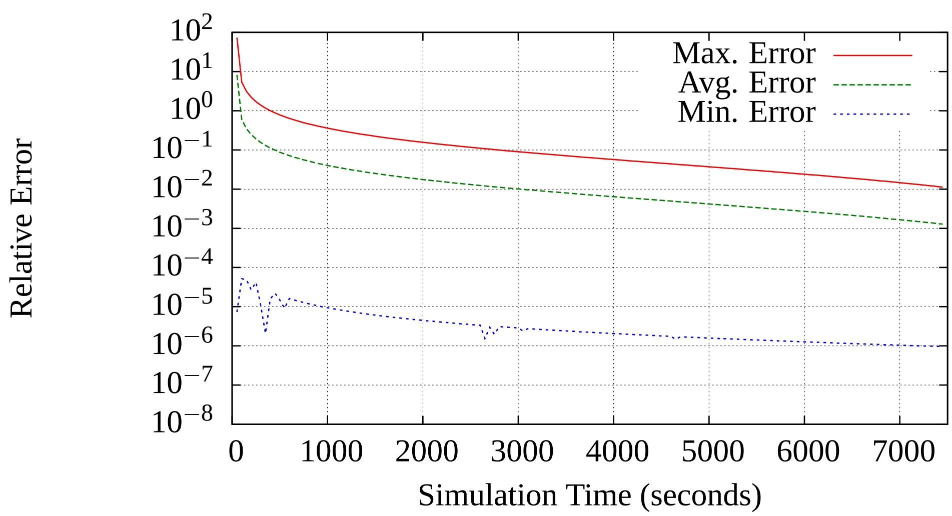

Figure 5.7: Lyapunov exponents relative error versus time.

5.5.2 Basin of Attraction

To validate the basin of attraction (BoA) edge algorithm a grid search was completed around the BoA edge found for case $b/l = 0.35$ at POI 1 (refer to Fig. 4.4 on page 44). The parameters shown in Table 5.5 were used for the simulations. Fig. 5.8 shows the results of the grid search, where the red dots are the stable points and the blue dots are the unstable points. Since calculating the Lyapunov exponents proved to be not feasible for multiple trials, the stability of the system was determined using the POI conditions as the Poincaré section. If all of the states of the system, excluding x, were within 10^{-3} of the stable orbit at the POI, then the system was determined to be stable. Fig. 5.8 shows that the grid search and the BoA edge algorithm results are in agreement. The BoA edge algorithm took 8043 function evaluations to find the edges to an angular relative error of 10^{-4} and the grid search consisted of 6282 points. The BoA edge algorithm was found to be reliable at finding non-riddled basins of attraction. Further more, the BoA edge algorithm, like a grid search method, is based on the input of "stable" or "unstable", so any method for determining the stability of the system could be used.

Table 5.5: BASIN OF ATTRACTION – PARAMETERS

Model Parameters Parameters							
l	$=$	0.4064	$[m]$	ρ	$=$	0.0813	$[m]$
δ	$=$	0°	$[degrees]$	γ	$=$	2.00°	$[degrees]$
m	$=$	5.000	$[kg]$	M	$=$	0	$[kg]$
r_g	$=$	0.1138	$[m]$				
Contact Parameters							
μ_s	$=$	0.38		μ_c	$=$	0.26	
k_s	$=$	10^6	$[N/m^{3/2}]$	k_d	$=$	10^7	$[Ns/m^{5/2}]$
σ_0	$=$	10^5	$[N/m]$	σ_1	$=$	$2\sqrt{\sigma_0}$	$[Ns/m]$
v_s	$=$	10^-4	$[m/s]$	α^0	$=$	10°	

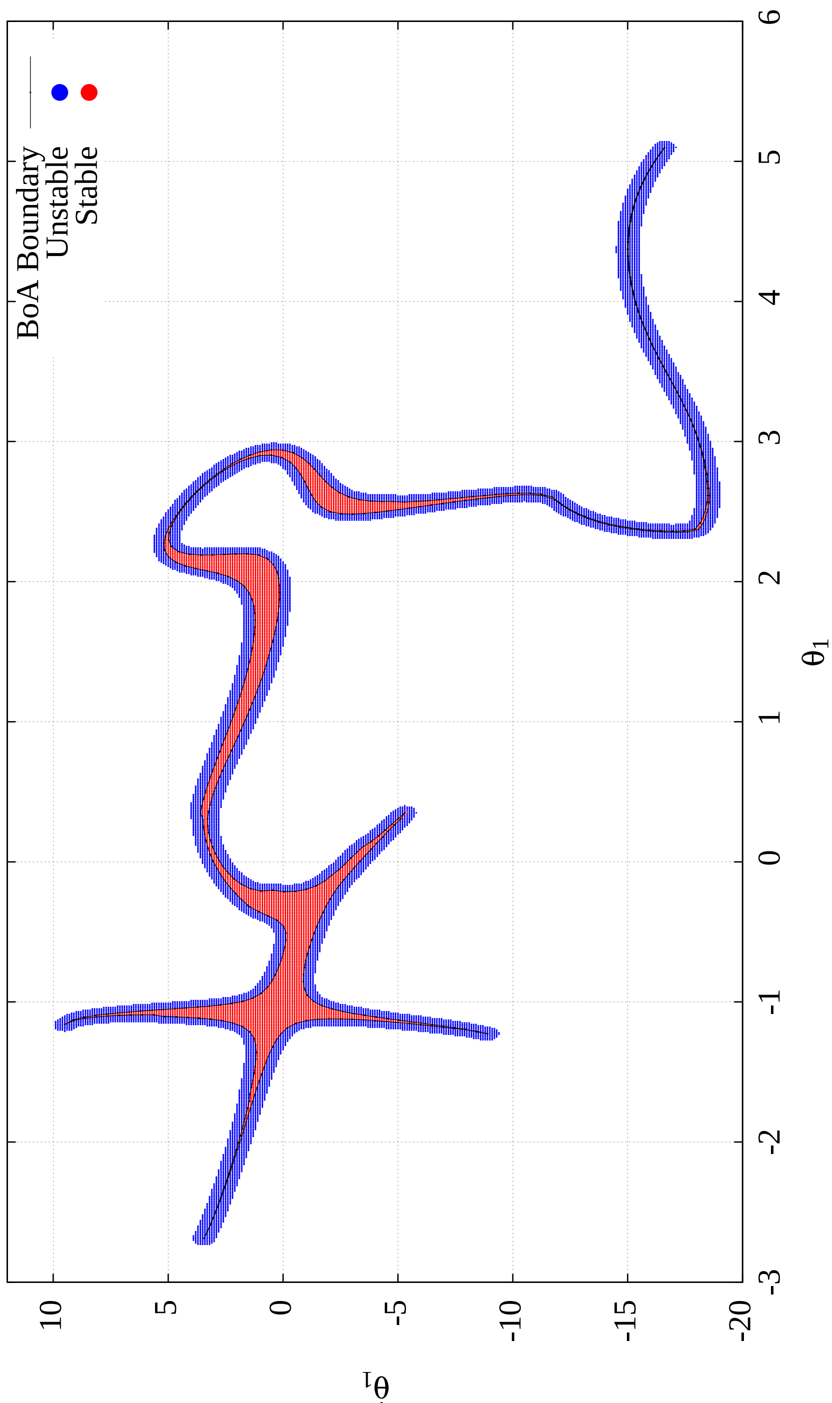

Figure 5.8: BoA edge algorithm validation case: $\frac{b}{l} = 0.35$, POI 1.

Using the BoA edge algorithm, the basin of attraction was found for all eight points of interest for eight different center of mass locations using the parameters in Table 5.5. The center of mass locations are shown in Table 5.6. The stability of the system was determined using a Poincaré section, as mention above. Fig. 5.9 to Fig. 5.16 show how the basin of attraction is effected by the center of mass for POI one to eight. The shape of the basins of attraction on the center of mass boundaries (CoM 16% and CoM 50%) were found to be less broad than between CoM 16% and CoM 50%.

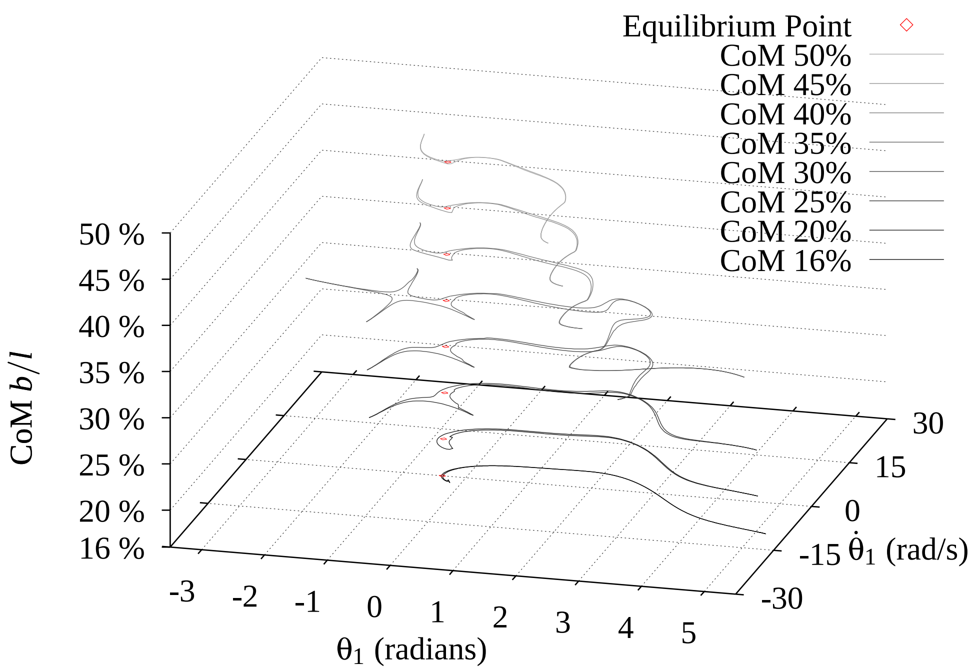

Figure 5.9: BoA for point of interest one.

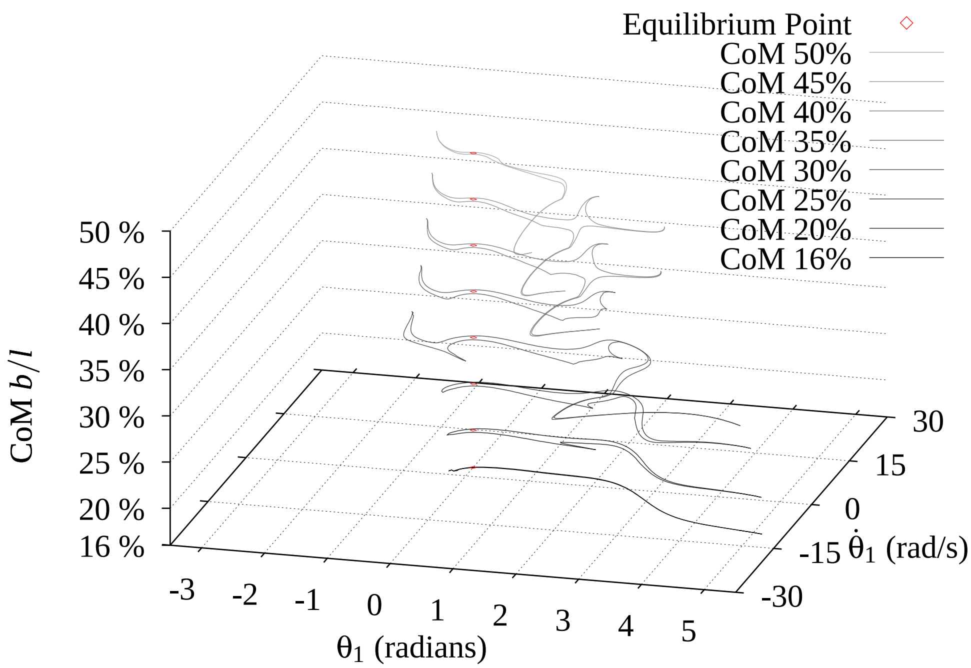

Figure 5.10: BoA for point of interest two.

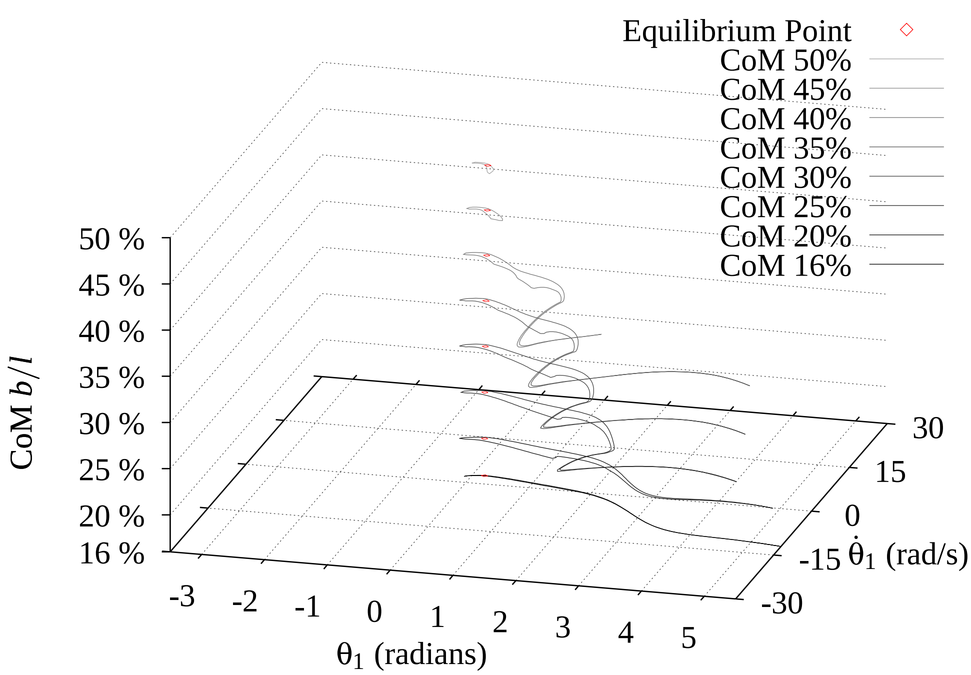

Figure 5.11: BoA for point of interest three.

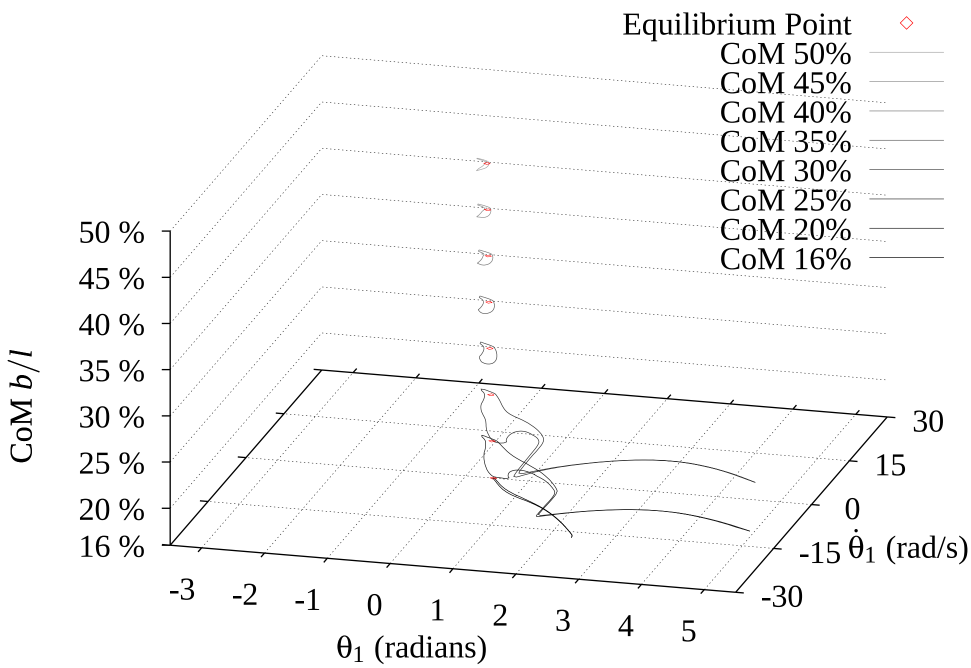

Figure 5.12: BoA for point of interest four.

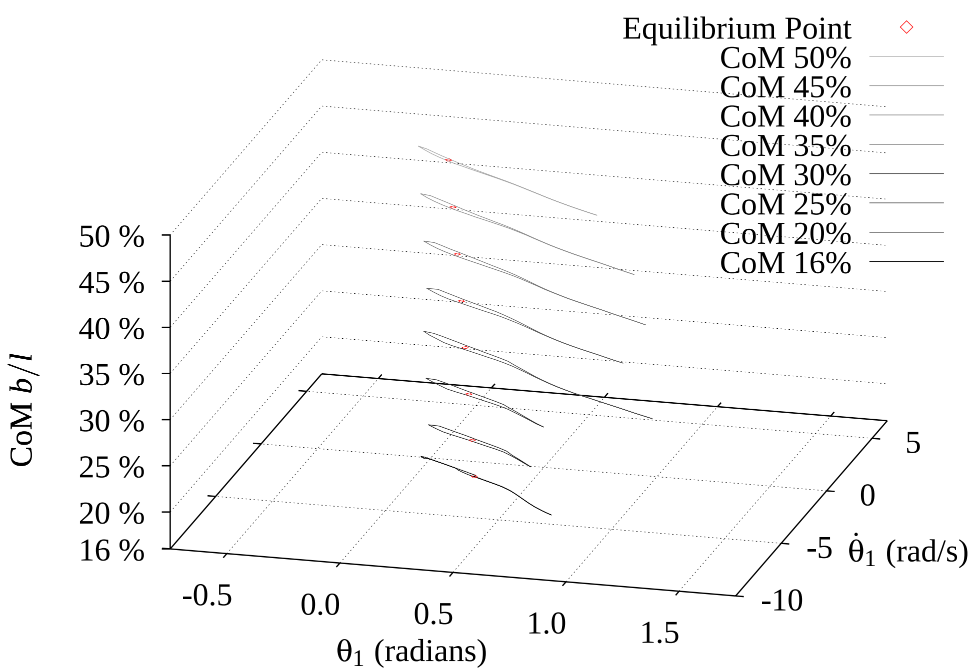

Figure 5.13: BoA for point of interest five.

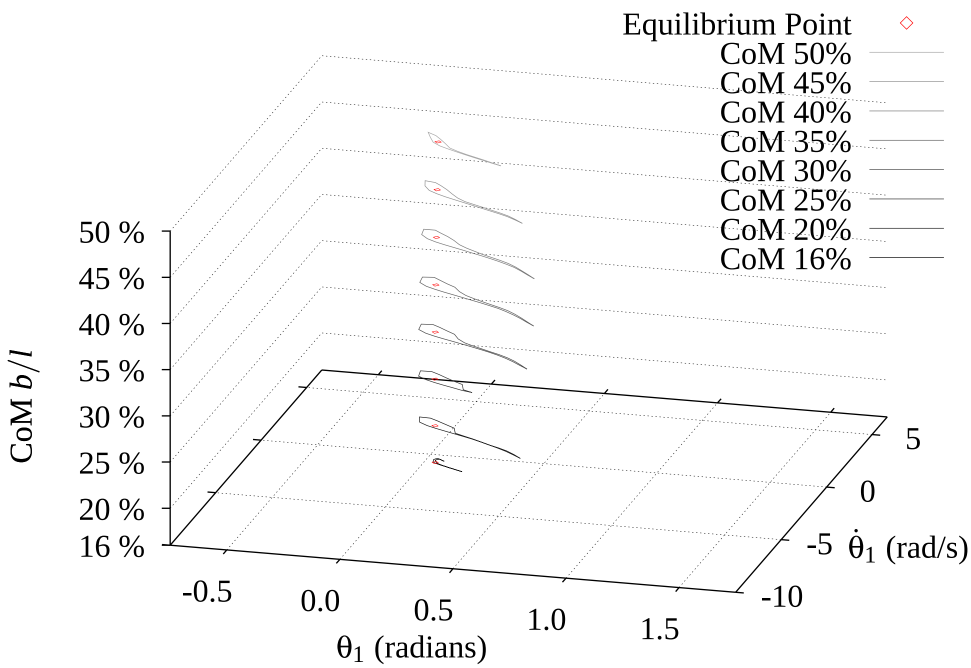

Figure 5.14: Point of interest six.

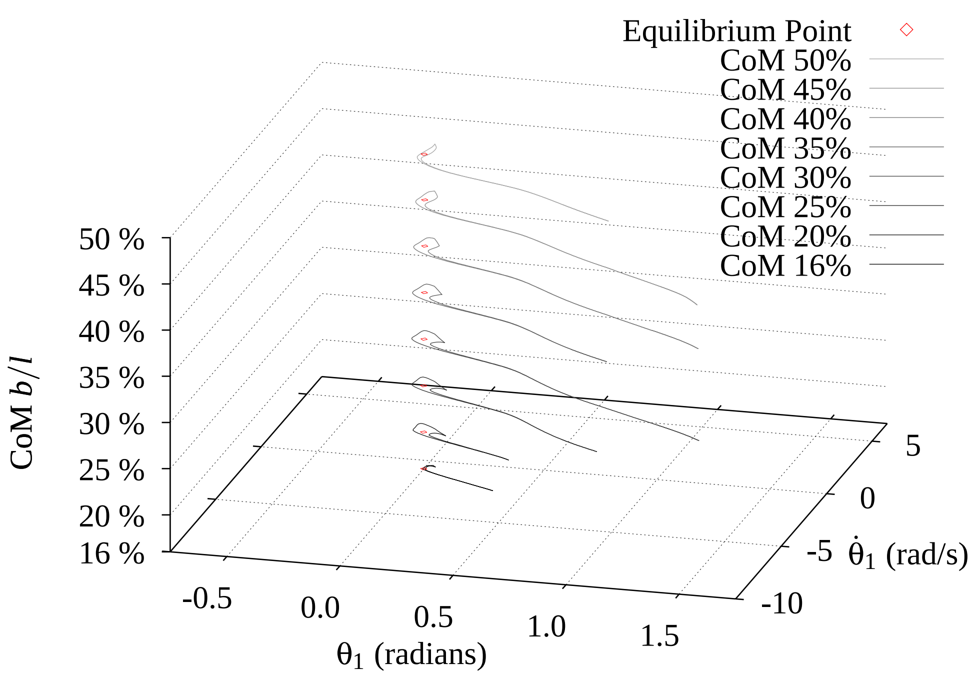

Figure 5.15: BoA for point of interest seven.

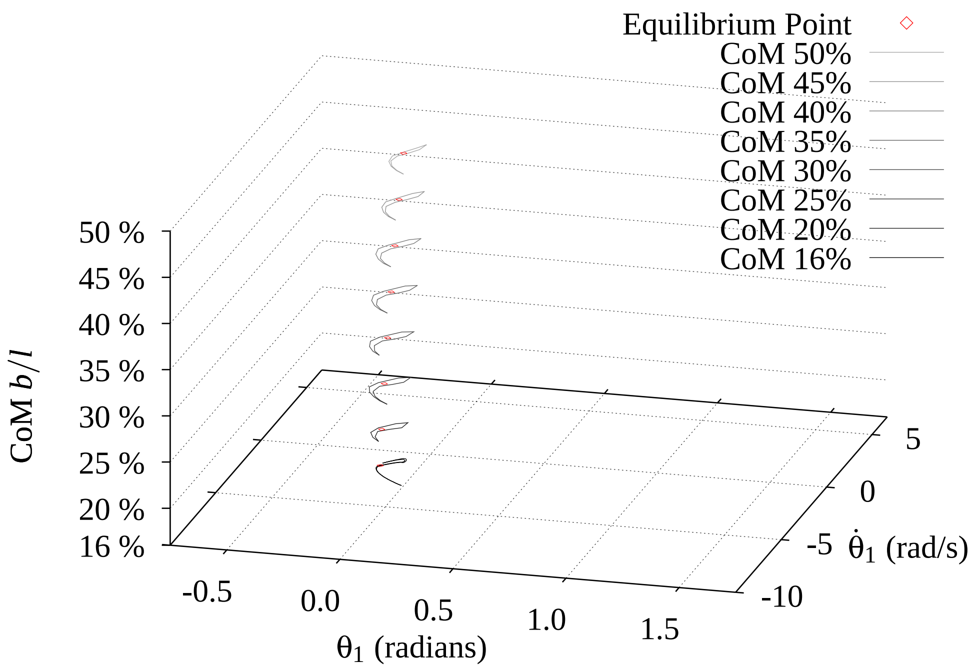

Figure 5.16: BoA for point of interest eight.

Table 5.6: BASIN OF ATTRACTION – CENTER OF MASS PARAMETERS.

Center of Mass b	
$[m]$	b/l
0.0650	16 %
0.0813	20 %
0.1016	25 %
0.1219	30 %
0.1422	35 %
0.1626	40 %
0.1829	45 %
0.2032	50 %

The basins of attraction that were found for the swing leg[1] were found to extend far in the $+\theta$ direction. When the system is offset in the $+\theta$ direction, the angular velocity needs to be adjusted accordingly to return the system back to the stable orbit. Fig. 5.17 shows a visualization of this abnormality, where the swing leg has a large angular offset. As the larger the angular offset, the more precise angular velocity is required. The larger the

[1]i.e. the swing leg parameters were offset, POI 1 to 4.

velocity creates a larger impact force, which in a physical walker would not be contained locally. The model only accounts for local deformation at the contact, not vibrations or deformation of the structure. If vibration of deformation of the structure were accounted for, the BoA of the swing leg would most likely be smaller.

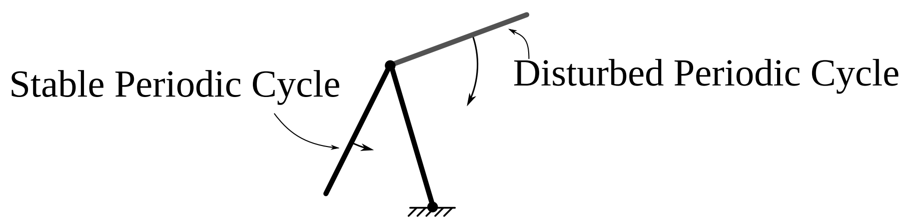

Figure 5.17: Visualization of the swing leg BoA abnormality.

Fig. 5.18 and Fig. 5.19 show the change in area of the BoA versus the change in the CoM for different points of interest along the stable periodic cycle. To account for the abnormality of the swing leg BoA, mentioned above, only the area of the BoA that had an angular offset of less than $\pi/2$ was calculated. From Fig. 5.18 and Fig. 5.19 determining which center of mass location has the largest stability region is not clear. However, it is easy to see that there is a favourable point between 16% and 50%.

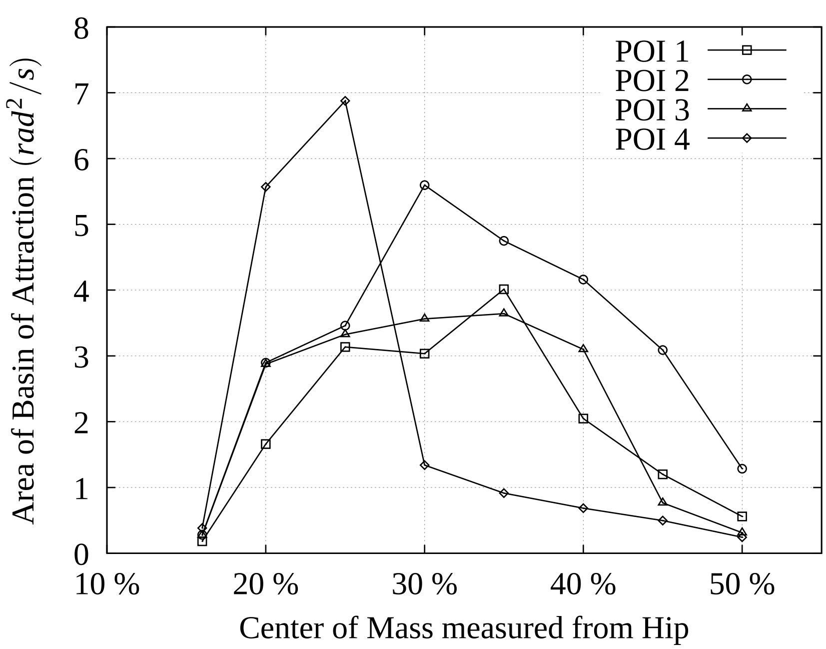

Figure 5.18: Area of the BoA for points of interest that belong to the swing leg.

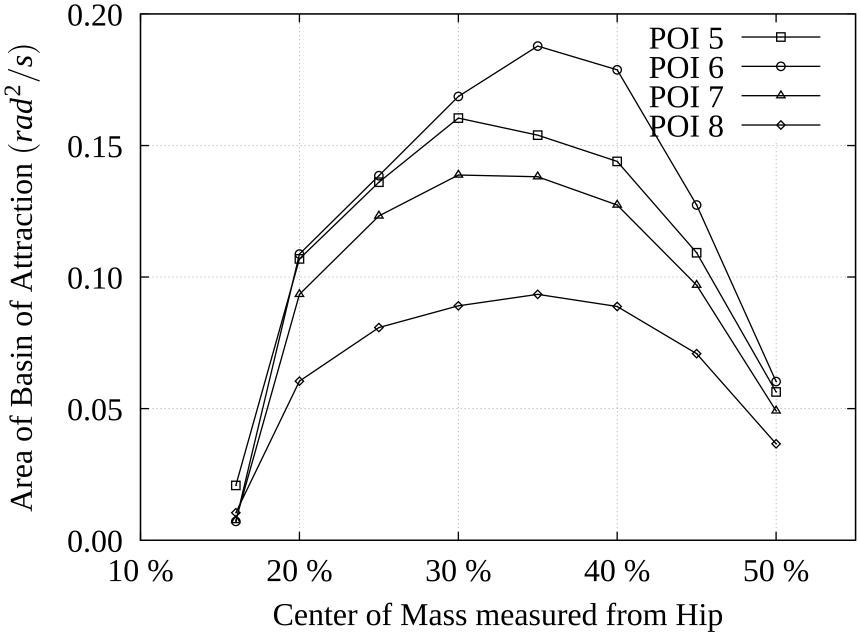

Figure 5.19: Area of the BoA for points of interest that belong to the stance leg.

5.6 Angular Momentum

5.6.1 Angular Momentum vs BoA

Fig. 5.20 show the average absolute angular momentum and ground reaction torque and maximum absolute angular momentum and ground reaction torque of the walker. The angular momentum of the walker was calculated about the center of mass of the walker. The ground reaction torque is the resulting torque caused by the ground reaction forces acting about the center of mass. The average absolute values were calculated by numerically integrating the absolute value and dividing by the period of integration, as shown in (5.4).

$$|\bar{L}| = \frac{1}{t_1 - t_0} \int_{t_0}^{t_1} |L| \tag{5.4}$$

Fig. 5.21 shows the normalized values of Fig. 5.20. The angular momentum was normalized by dividing by the walker height (l), total mass $(2m+M)$, and average hip velocity $(\bar{v}_{hip})$. The torque was normalized by dividing by the height (l), total mass $(2m + M)$ and the acceleration due to gravity (g). As can be seen from Fig. 5.20 and Fig. 5.21, the angular momentum does not display any minimum or maximum between the center of mass locations of 16% and 50% of the leg length. In contrast, the area of the basin of attraction, shown in Fig. 5.18 and Fig. 5.19, shows a favourable point between the center of mass locations of 16% and 50% of the leg length. These results give evidence that the angular momentum of the gait of a biped walker does not correlate to the stability of the gait. This is supported by [32], where the authors suggest that angular momentum is kept small in human walking to reduce the energy required to continue the gait. This statement would make sense if the passive dynamics of the human body have a low angular momentum gait.

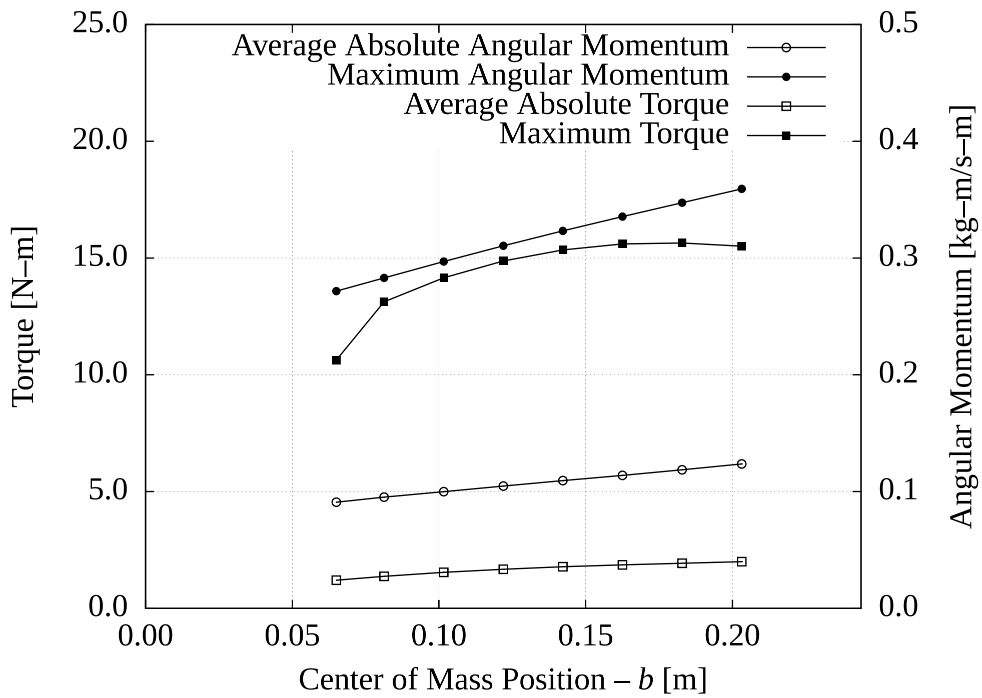

Figure 5.20: Maximum and absolute average torque and angular momentum.

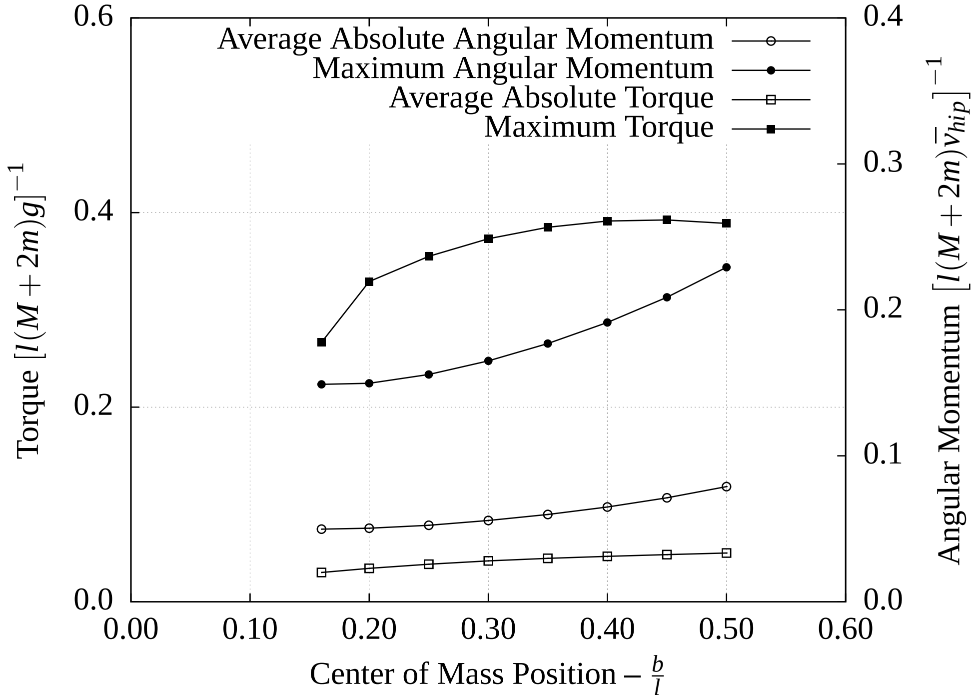

Figure 5.21: Maximum and absolute average torque and angular momentum - normalized.

5.6.2 Angular Momentum with Human Parameters

Recently there have been studies that have measured the angular momentum of the human body during walking [32][33][34]. Humans were found to have a relatively low angular momentum during a normal walking gait. This low angular momentum was attributed to the control of the central nervous system. In the sagittal plane, the angular momentum was found to be low due to canceling angular momenta from opposing leg limbs [32]. This section explores the question "How much of the relatively low angular momentum of the human gait is from the control of the central nervous system?"

First off, what is defined as low angular momentum? In [32], the authors use a falling inverted pendulum as a reference. The inverted pendulum was found to have a maximum normalized angular momentum of ~ 0.2. To determine what the angular momentum of the passive walker, simulations were completed with the parameters in Table 5.7. The parameters in Table 5.7. were set to human like values using data from [35]. Fig. 5.22 shows the angular momentum of the passive dynamic walker over one stride and Fig. 5.23

shows the ground reaction torque over one stride for the parameters in Table 5.7. The absolute maximum normalized angular momentum experienced by the walker was ~ 0.13. The angular momentum of the walker was normalized with the average hip velocity $(\bar{v}_{hip})$, total mass $(2m+M)$, and the walker leg length (l).

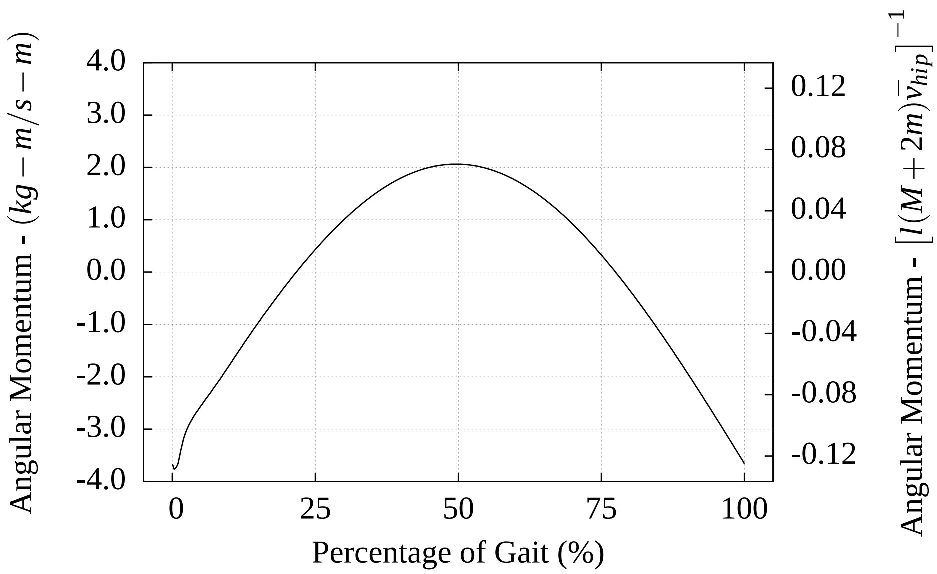

Figure 5.22: Angular momentum of the walker about the center of mass over one step.

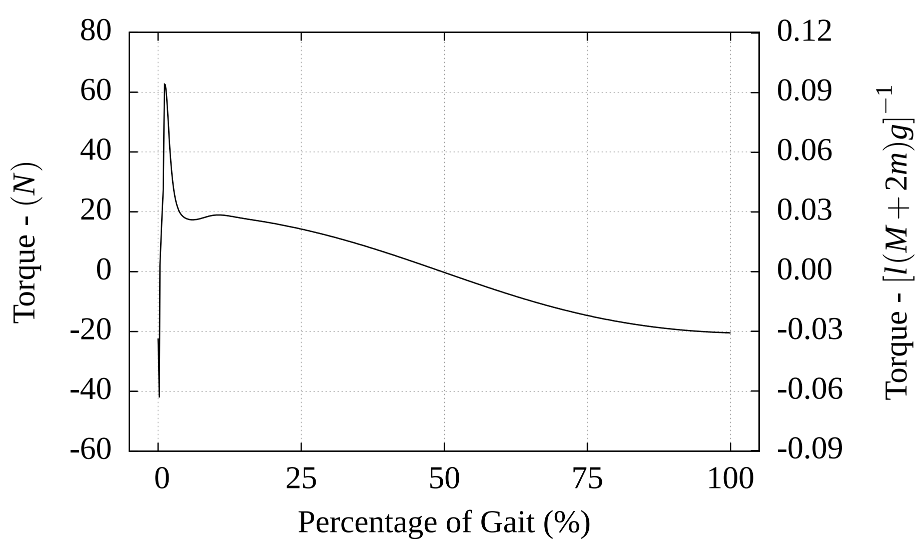

Figure 5.23: Ground reaction torque over one step.

Table 5.7: ANTHROPOMORPHIC PASSIVE WALKER PARAMETERS.

		Model Parameters Parameters					
l	$=$	0.8471	$[m]$	ρ	$=$	$l(0.20)$	$[m]$
δ	$=$	0°	$[degrees]$	$(2m+M)$	$=$	80	$[kg]$
m	$=$	$(2m+M)(0.157)$	$[kg]$	M	$=$	$(2m+M)(0.686)$	$[kg]$
r_g	$=$	$l(0.317)$	$[m]$	b	$=$	$l(0.434)$	$[m]$
γ	$=$	0.6°	$[degrees]$				
		Contact Parameters					
μ_s	$=$	0.38		μ_c	$=$	0.26	
k_s	$=$	8×10^6	$[N/m^{3/2}]$	k_d	$=$	8×10^7	$[N s/m^{5/2}]$
σ_0	$=$	10^5	$[N/m]$	σ_1	$=$	$2\sqrt{\sigma_0}$	$[N s/m]$
v_s	$=$	10^-4	$[m/s]$	α^0	$=$	10°	

The absolute maximum normalized angular momentum of the walker is larger than what was found for humans. The authors of [34] and [33] found the maximum normalized angular momentum to be 0.02 normalized with the body height instead of the leg length (if normalized with the leg length would be $\sim$ 0.04). In [32] the maximum normalized angular momentum was found to be 0.05, normalized with the body center of mass height instead of the leg length (if normalized with the leg length would be slightly larger). In all cases the passive walker experienced more than double the maximum normalized angular momentum.

Why does the passive walker experience a larger angular momentum or more importantly why do humans experience less angular momentum through out their gait. Would a more anthropomorphic passive walker, one with knees or one with an upper body like the one designed in [36], experience less angular momentum than the current passive walker? The answer to that question would provide insight into the questions: “To what degree does the central nervous system control the human gait to have a low angular momentum?” and “Does the central nervous system control the angular momentum of the human gait to be low for energy efficiency?”

Chapter 6

Conclusions and Future Work

6.1 Conclusions

A new mathematical model of passive walking was developed with the Hunt-Crossley contact model and the LuGre friction model. Even with the added complexity of the contact and friction models, stable periodic motion was produced with the proposed passive walking model. The passive walking model was able to simulate the entire gait with one set of equations[1]. The proposed mathematical model was able to replicate the results of the experiments very well. The proposed passive walking mathematical model matched the trend and magnitude of the experimental gait measurements. The impact-based passive walking model also matched the trends of the experimental gait, but was not able to match the gait parameters magnitude. The difference in magnitude between the two mathematical models is attributed to the proposed passive walking mathematical model being able to adjust the damping (i.e. energy loss) of the heel strike impact. The impact-based mathematical model was not stable for the same parameter range as the experiments and proposed mathematical model. The difference in stable parameter range is attributed to the effects of friction.

The sliding velocity between the ramp and the foot never stays at zero. However, the

[1] Does not switch between impact and motion equations like the traditional impact-based passive walking model

sliding velocity does remain below the Stribeck velocity. A friction model with the complexity of the LuGre model may not be needed to capture a majority of the dynamic features of the gait. A friction model that accounts for transition between micro-sliding[2] and full sliding would be sufficient for this dynamic model.

The Lyapunov exponents were calculated for one case. The sign of the Lyapunov exponents were $(0, -, -, \ldots)$ which shows that the passive walking mathematical model is moving in a stable period motion. A Poincaré map was used to determine a "stable" gait from an "unstable" gait. The Poincaré map was used because numerically calculating Lyapunov exponents was found not feasible with the available time and resources. The basin of attraction of the proposed passive walking mathematical model was determine in the θ_1–$\dot{\theta}_1$ (Leg angle–Leg angle velocity) plane. The basin of attraction was found for eight different points in the gait cycle with eight different center of mass locations. The method developed for finding the basin of attraction was able to more efficiently find the basin of attraction compared to a full grid search method.

Increasing the size of the basin of attraction of the passive walker will create a more robust gait and a passive walker that can reject larger disturbances. A favourable center of mass is evident from the area of the basin of attraction determined. However, the angular momentum of the walker versus the center of mass did not show any minimum or maximum. From these results, angular momentum regulation does not seem to play a role in the ability of the passive walker to reject disturbances.

The question was posed: "How much of the relatively low angular momentum of the human gait is from the control of the central nervous system?". The passive walker was found to have a maximum normalized angular momentum of ~ 0.13 more than double than that determined for a human gait of 0.04–0.05. Does the difference between the passive walker angular momentum and the human gait angular momentum stem from the control of the central nervous system of the human gait or is the human body mechanically better tuned to cancel out the angular momentum of the limbs?

[2] the sliding velocity is less then the Stribeck velocity

6.2 Future Work

This model can be used as a framework to develop more complex models (i.e. a passive walker with knees or adding friction to the hip joint). As well, finding a less complex friction model that still captures the necessary dynamics could reduce the number of states of the system. A reduction in the number of states of the system would could reduce the computation time.

Finding a more efficient way of calculating the Lyapunov exponents would improve the methods available for stability analysis of the proposed passive walking mathematical model. By reducing the complexity of the friction model may prove to reduce the time required to calculate the Lyapunov exponents. The basin of attraction edge algorithm can be improved. A method of determining the rough size of the BoA before computation would be advantageous in determining the appropriate step size. As well, the BoA edge algorithm could be extended into three dimensions by using triangles to map out the shape.

The inclinometer sensing device needs to be improved upon for the orientation data to be usable. There are two obvious design routes. The first design route is to reduce the vibrations experienced by the inclinometer. The second design route is to improve the settling time of a pendulum-encoder inclinometer. Another option is to use a motion capture system to determine the orientation of the walker.

Analyzing a more anthropomorphic passive dynamic biped walker may provide insight into the questions posed about the angular momentum of the human gait.

Bibliography

[1] S. Mochon and T. McMahon, “Ballistic walking: An improved model,” Mathematical Biosciences, vol. 52 (3).

[2] T. McGeer, “Passive dynamic walking,” International Journal of Robotics Research, vol. 9 (2), 1990, pp. 62–82.

[3] T. McGeer, “Passive walking with knees,” in Proc. of the 1990 IEEE International Conference on Robotics and Automation, Cincinnati, OH , USA, 1990, pp. 1640–1645.

[4] M. Garcia, A. Chatterjee, A. Ruina, and M. Coleman, “The simplest walking model: Stability, complexity, and scaling,” ASME Journal of Biomechanical Engineering, vol. 120 (2), 1998, pp. 281–288.

[5] A. Goswami, B. Thuilot, and B. Espiau, “A study of the passive gait of a compass-like biped robot: Symmetry and chaos,” International Journal of Robotics Research, vol. 17 (12), 1998, pp. 1282–1301.

[6] Y. Ikemata, K. Yasuhara, A. Sano, and H. Fujimoto, “A study of the leg–swing motion of passive walking,” in Proc. of the 2008 IEEE International Conference on Robotics and Automation, Pasadena, CA , USA, 2008, pp. 1588–1593.

[7] F. Qi, T. Wang, and J. Li, “The elastic contact influences on passive walking gaits,” Robotica, vol. 29, 2010, pp. 787–796.

[8] M. Jafarian, Variable stiffness for robust and energy efficient 2D bipedal locomotion, M.Sc. Report, University of of Twente, Enschede, Netherlands, 2010.

[9] M. Iribe, T. Kinugasa, Y. Sugimoto, and K. Osuka, “Dynamical model verification of passive dynamic walking with a compass model prototype,” in SICE Annual Conference 2010, 2010, pp. 2800–2803.

[10] S. Collins, A. Ruina, R. Tedrake, and M. Wisse, “Efficient bipedal robots based on passive-dynamic walkers,” Science, vol. 307 (5712), 2005, pp. 1082–1085.

[11] Y. Hurmuzlu and T.-H. Chang, “Rigid body collisions of a special class of planar kinematic chains,” IEEE Transactions on Systems, Man, and Cybernetics, vol. 22 (5), 1992, pp. 964–971.

[12] H. Hertz, Miscellaneous Papers, London: MacMillan and Co., Ltd., chap. Chapter 5: On the contact of elastic solids, 2006, pp. 146–162.

[13] K. Hunt and F. R. Crossley, “Coefficient of restitution interpreted as damping in vibroimpact,” Journal of Applied Mechanics, vol. 42 (2), 1975, pp. 440–445.

[14] L. Shampine and M. Reichelt, The Matlab ODE Suite, MathWorks, Inc., 24 Prime Park Way, Natick, MA.

[15] G. Gilardi and I. Sharf, “Literature survey of contact dynamics modeling,” Mechanism and Machine Theory, vol. 37 (10), 2002, pp. 1213–1239.

[16] H. Olsson, K. Åström, C. Canudas de Wit, M. Gäfvert, and P. Lischinsky, “Friction models and friction compensation,” European Journal of Control, vol. 4 (3), 1998, pp. 176–195.

[17] C. Canudas de Wit, H. Olsson, K. Åström, and P. Lischinsky, “A new model for control systems with friction,” IEEE Transactions on Automatic Control, vol. 40 (3), 1995, pp. 419–425.

[18] M. Vukobratovic and B. Borovac, “Zero-moment point - thirty five years of its life,” International Journal of Humanoid Robotics, vol. 1 (1), 2004, pp. 157–173.

[19] A. Goswami, “Postural stability of biped robots and the foot-rotation indicator (fri) point,” International Journal of Robotics Research, vol. 18 (6), 1999, pp. 523–533.

[20] M. Popovic, A. Hofmann, and H. Herr, “Zero spin angular momentum control: Definition and applicability,” in Proc. of the 2004 IEEE RAS/RSJ International Conference on Humanoid Robots, Los Angeles, CA, USA, 2004, vol. 1, pp. 478–493.

[21] A. Goswami and V. Kallem, “Rate of change of angular momentum and balance maintenance of biped robots,” in Proc. of the 2004 IEEE International Conference on Robotics and Automation, New Orleans, LA , USA, 2004, pp. 3785–3790.

[22] M. Popovic, A. Goswami, and H. Herr, “Ground reference points in legged locomotion: Definitions, biological trajectories and control implications,” International Journal of Robotics Research, vol. 24 (12), 2005, pp. 1013–1032.

[23] Q. Wu and N. Sabet, “An experimental study of passive dynamic walking,” Robotica, vol. 22, 2004, pp. 251–262.

[24] Q. Wu and J. Chen, “Effects of ramp angle and mass distribution on passive dynamic gait- an experimental study,” International Journal of Humanoid Robotics, vol. 7 (1), 2010, pp. 55–72.

[25] J. Chen, Design and dynamic analysis of four-legged passive dynamic walker with knees, B.Sc. Thesis, University of Manitoba, Winnipeg, Manitoba, 2007.

[26] A. Greaves and I. Lohrenz, A study in passive dynamic walking, B.Sc. Thesis, University of Manitoba, Winnipeg, Manitoba, 2008.

[27] K. Rushdi, Experimental study on passive dynamic bipedal walking: effects of parameter changes on gait patterns, M.Sc. Thesis, University of Manitoba, Winnipeg, MB, 2011.

[28] D. Koop, Passive dynamic bipedal walking: Ramp-Treadmill comparison and gait variation due to parameter change, B.Sc. Thesis, University of Manitoba, Winnipeg, MB, 2010.

[29] A. Wolf, J. Swift, H. Swinney, and J. Vastano, "Determining lyapunov exponents from a time series," Physica D, 1985, pp. 285–317.

[30] M. Sobczyk, E. Perondi, and M. A. Cunha, "A continuous approximation of the lugre friction model," in ABCM Symposium Series in Mechatronics, 2010, vol. 4, pp. 218–228.

[31] H. Olsson, Control systems with friction, Ph.D. Dissertation, Lund Institute of Technology, Sweden, 1996.

[32] H. Herr and M. Popovic, "Angular momentum in human walking," Journal of Experimental Biology, vol. 211, 2008, pp. 467–481.

[33] A. Silverman, J. Wilken, E. Sinitski, and R. Neptune, "Whole-body angular momentum in incline and decline walking," Journal of Biomechanics, vol. 45, 2012, pp. 965–971.

[34] M. Popovic, A. Hofmann, and H. Herr, "Angular momentum regulation during human walking: biomechanics and control," in Proc. of the 2004 IEEE International Conference on Robotics and Automation, New Orleans, LA , USA, 2004, vol. 3, pp. 2405–2411.

[35] W. Dempster, "Space requirements of the seated operator: Geometrical, kinematic, and mechanical aspects of the body, with special reference to the limbs," Tech. rep., University of Michigan, 1955, wADC Technical Report 55-159.

[36] S. Collins, M. Wisse, and A. Ruina, "A three dimensional passive-dynamic walking robot with two legs and knee," International Journal of Robotics Research, vol. 20 (7), 2001, pp. 607–615.

Appendix A

Additional Mathematical Model Equations

Appendix A provides some additional information about the mathematical model. The equations of motion are transformed into the form of (A.1).

$$\ddot{\mathbf{q}} = \mathbf{A}^{-1}\mathbf{B} \tag{A.1}$$

Where

$$\mathbf{A} = \mathbf{M} \tag{A.2}$$
$$\mathbf{B} = \mathbf{F}(\mathbf{q}, \dot{\mathbf{q}}) - \mathbf{H}(\mathbf{q}, \dot{\mathbf{q}}) - \mathbf{G}(\mathbf{q}) \tag{A.3}$$

The Jacobian of the proposed passive walking mathematical model is given in detail. The Jacobian of the original system and the Jacobian of the system with the smooth approximation made to the LuGre model are given. Also, the equilibrium points of the proposed passive walking mathematical model are given, assuming the swing leg ground clearance procedure is not used.

A.1 Proposed Mathematical Model Reformed

The proposed passive walking mathematical model is reformed to make the numerical solution of the model less cumbersome.

$$\mathbf{A}^{-1} = \begin{bmatrix} \frac{A_M(c_1^2+c_2^2+A_M)+C_mC_p}{M_W} & \frac{A_{sc}(A_M+1)}{M_W} & -\frac{C_{AC}}{b} & -\frac{C_{CA}}{b} \\ \frac{A_{sc}(A_M+1)}{M_W} & \frac{A_M(s_1^2+s_2^2+A_M)-C_mC_p}{M_W} & -\frac{S_{AC}}{b} & -\frac{S_{CA}}{b} \\ -\frac{C_{AC}}{b} & -\frac{S_{AC}}{b} & \frac{A_M M_W}{b^2} & \frac{C_m M_W}{b^2} \\ -\frac{C_{CA}}{b} & -\frac{S_{CA}}{b} & \frac{C_m M_W}{b^2} & \frac{A_M M_W}{b^2} \end{bmatrix} \frac{1}{m(A_M^2-C_m^2)} \tag{A.4}$$

$$\mathbf{B} = \begin{bmatrix} (F_{f_1}+F_{f_2})+mb(\dot{\theta}_1^2\sin\theta_1+\dot{\theta}_2^2\sin\theta_2)+g(M+2m)\sin\gamma \\ (F_{N_1}+F_{N_1})-mb(\dot{\theta}_1^2\cos\theta_1-\dot{\theta}_2^2\cos\theta_2)-g(M+2m)\cos\gamma \\ F_{f_1}c_{y_1}^{hip}+F_{N_1}c_{x_1}^{hip}-mgb\sin(\theta_1-\gamma) \\ F_{f_2}c_{y_2}^{hip}+F_{N_2}c_{x_2}^{hip}-mgb\sin(\theta_2-\gamma) \end{bmatrix} \tag{A.5}$$

$$M_W = 2+\frac{M}{m} \tag{A.6}$$

$$A_M = M_W\left(1+\left(\frac{r_g}{b}\right)^2\right)-1 \tag{A.7}$$

$$A_{sc} = \sin\theta_1\cos\theta_1+\sin\theta_2\cos\theta_2 \tag{A.8}$$

$$C_m = \cos(\theta_1-\theta_2),\ S_m = \sin(\theta_1-\theta_2) \tag{A.9}$$

$$C_p = \cos(\theta_1+\theta_2),\ S_p = \sin(\theta_1+\theta_2) \tag{A.10}$$

$$C_{CA} = \cos\theta_1 C_m+\cos\theta_2 A_M \tag{A.11}$$

$$S_{CA} = \sin\theta_1 C_m+\sin\theta_2 A_M \tag{A.12}$$

$$C_{AC} = \cos\theta_1 A_M+\cos\theta_2 C_m \tag{A.13}$$

$$S_{AC} = \sin\theta_1 A_M+\sin\theta_2 C_m \tag{A.14}$$

A.2 Jacobian

The Jacobian of the of the proposed mathematical model (A.15) is needed to compute the Lyapunov exponents with the method outlined in [29]. The Jacobian of the system can also be used to monitor the stability of the solution for some numerical solvers.

$$\mathbf{J}(\mathbf{Q}) = \begin{bmatrix} 0 & 0 & 0 & 0 & 1 & 0 & 0 & 0 & 0 & 0 \\ 0 & 0 & 0 & 0 & 0 & 1 & 0 & 0 & 0 & 0 \\ 0 & 0 & 0 & 0 & 0 & 0 & 1 & 0 & 0 & 0 \\ 0 & 0 & 0 & 0 & 0 & 0 & 0 & 1 & 0 & 0 \\ 0 & \frac{\partial f_5}{\partial y} & \frac{\partial f_5}{\partial \theta_1} & \frac{\partial f_5}{\partial \theta_2} & \frac{\partial f_5}{\partial \dot{x}} & \frac{\partial f_5}{\partial \dot{y}} & \frac{\partial f_5}{\partial \dot{\theta}_1} & \frac{\partial f_5}{\partial \dot{\theta}_2} & \frac{\partial f_5}{\partial z_1} & \frac{\partial f_5}{\partial z_2} \\ 0 & \frac{\partial f_6}{\partial y} & \frac{\partial f_6}{\partial \theta_1} & \frac{\partial f_6}{\partial \theta_2} & \frac{\partial f_6}{\partial \dot{x}} & \frac{\partial f_6}{\partial \dot{y}} & \frac{\partial f_6}{\partial \dot{\theta}_1} & \frac{\partial f_6}{\partial \dot{\theta}_2} & \frac{\partial f_6}{\partial z_1} & \frac{\partial f_6}{\partial z_2} \\ 0 & \frac{\partial f_7}{\partial y} & \frac{\partial f_7}{\partial \theta_1} & \frac{\partial f_7}{\partial \theta_2} & \frac{\partial f_7}{\partial \dot{x}} & \frac{\partial f_7}{\partial \dot{y}} & \frac{\partial f_7}{\partial \dot{\theta}_1} & \frac{\partial f_7}{\partial \dot{\theta}_2} & \frac{\partial f_7}{\partial z_1} & \frac{\partial f_7}{\partial z_2} \\ 0 & \frac{\partial f_8}{\partial y} & \frac{\partial f_8}{\partial \theta_1} & \frac{\partial f_8}{\partial \theta_2} & \frac{\partial f_8}{\partial \dot{x}} & \frac{\partial f_8}{\partial \dot{y}} & \frac{\partial f_8}{\partial \dot{\theta}_1} & \frac{\partial f_8}{\partial \dot{\theta}_2} & \frac{\partial f_8}{\partial z_1} & \frac{\partial f_8}{\partial z_2} \\ 0 & 0 & \frac{\partial f_9}{\partial \theta_1} & 0 & \frac{\partial f_9}{\partial \dot{x}} & 0 & \frac{\partial f_9}{\partial \dot{\theta}_1} & 0 & \frac{\partial f_9}{\partial z_1} & 0 \\ 0 & 0 & 0 & \frac{\partial f_5}{\partial \theta_2} & \frac{\partial f_{10}}{\partial \dot{x}} & 0 & 0 & \frac{\partial f_{10}}{\partial \dot{\theta}_2} & 0 & \frac{\partial f_{10}}{\partial z_2} \end{bmatrix} \tag{A.15}$$

$$\frac{\partial f_{i+4}}{\partial q} = \frac{\partial \mathbf{B}}{\partial q} \cdot \mathbf{A}^{-1}_{(i,:)} \text{ for } i = 1 \text{ to } 4 \text{ and } q = [y, \dot{x}, \dot{y}, \dot{\theta}_1, \dot{\theta}_2, z_1, z_2] \tag{A.16}$$

$$\begin{aligned} \frac{\partial f_5}{\partial \theta_1} = \frac{\partial \mathbf{B}}{\partial \theta_1} \cdot \mathbf{A}^{-1}_{(1,:)} + \frac{1}{m(A_M^2 - C_m^2)} \Bigg(\left(\frac{-2c_1 s_1 A_M - S_m C_p - C_m S_p}{M_W} - 2mC_m S_m A^{-1}_{1,1} \right) B_1 \\ + \left(\frac{(c_1^2 - s_1^2)(A_M + 1)}{M_W} - 2mC_m S_m A^{-1}_{1,2} \right) B_2 \\ + \left(\frac{s_1 A_m + c_2 S_m}{b} - 2mC_m S_m A^{-1}_{1,3} \right) B_3 + \left(\frac{s_1 C_m + c_1 S_m}{b} - 2mC_m S_m A^{-1}_{1,4} \right) B_4 \Bigg) \end{aligned} \tag{A.17}$$

$$\begin{aligned} \frac{\partial f_5}{\partial \theta_2} = \frac{\partial \mathbf{B}}{\partial \theta_2} \cdot \mathbf{A}^{-1}_{(2,:)} + \frac{1}{m(A_M^2 - C_m^2)} \Bigg(\left(\frac{-2c_2 s_2 A_M + S_m C_p - C_m S_p}{M_W} + 2mC_m S_m A^{-1}_{1,1} \right) B_1 \\ + \left(\frac{(c_2^2 - s_2^2)(A_M + 1)}{M_W} + 2mC_m S_m A^{-1}_{1,2} \right) B_2 \\ + \left(\frac{s_2 C_m - c_2 S_m}{b} + 2mC_m S_m A^{-1}_{1,3} \right) B_3 + \left(\frac{s_2 A_m - c_1 S_m}{b} + 2mC_m S_m A^{-1}_{1,4} \right) B_4 \Bigg) \end{aligned} \tag{A.18}$$

$$
\begin{aligned}
\frac{\partial f_6}{\partial \theta_1} = \frac{\partial \mathbf{B}}{\partial \theta_1} \cdot \mathbf{A}^{-1}_{(2,:)} + \frac{1}{m(A_M^2 - C_m^2)} \Bigg(& \left(\frac{(c_1^2 - s_1^2)(A_M + 1)}{M_W} - 2mC_mS_mA^{-1}_{2,1} \right) B_1 \\
& + \left(\frac{2s_1c_1A_M + S_mC_p + C_mS_p}{M_W} - 2mC_mS_mA^{-1}_{2,2} \right) B_2 \\
& + \left(\frac{-c_1A_m + s_2S_m}{b} - 2mC_mS_mA^{-1}_{2,3} \right) B_3 + \left(\frac{-c_1C_m + s_1S_m}{b} - 2mC_mS_mA^{-1}_{2,4} \right) B_4 \Bigg)
\end{aligned}
\tag{A.19}
$$

$$
\begin{aligned}
\frac{\partial f_6}{\partial \theta_2} = \frac{\partial \mathbf{B}}{\partial \theta_2} \cdot \mathbf{A}^{-1}_{(2,:)} + \frac{1}{m(A_M^2 - C_m^2)} \Bigg(& \left(\frac{(c_2^2 - s_2^2)(A_M + 1)}{M_W} + 2mC_mS_mA^{-1}_{1,2} \right) B_1 \\
& + \left(\frac{2s_2c_2A_M - S_mC_p + C_mS_p}{M_W} + 2mC_mS_mA^{-1}_{2,2} \right) B_2 \\
& + \left(\frac{-c_2C_m - s_2S_m}{b} + 2mC_mS_mA^{-1}_{2,3} \right) B_3 + \left(\frac{-c_2A_m - s_1S_m}{b} + 2mC_mS_mA^{-1}_{2,4} \right) B_4 \Bigg)
\end{aligned}
\tag{A.20}
$$

$$
\begin{aligned}
\frac{\partial f_7}{\partial \theta_1} = \frac{\partial \mathbf{B}}{\partial \theta_1} \cdot \mathbf{A}^{-1}_{(3,:)} + \frac{1}{m(A_M^2 - C_m^2)} \Bigg(& \left(\frac{s_1A_m + c_2S_m}{b} - 2mC_mS_mA^{-1}_{3,1} \right) B_1 \\
& + \left(\frac{-c_1A_m + s_2S_m}{b} - 2mC_mS_mA^{-1}_{3,2} \right) B_2 \\
& + \left(-2mC_mS_mA^{-1}_{3,3} \right) B_3 + \left(-\frac{S_mM_W}{b^2} - 2mC_mS_mA^{-1}_{3,4} \right) B_4 \Bigg)
\end{aligned}
\tag{A.21}
$$

$$
\begin{aligned}
\frac{\partial f_7}{\partial \theta_2} = \frac{\partial \mathbf{B}}{\partial \theta_2} \cdot \mathbf{A}^{-1}_{(3,:)} + \frac{1}{m(A_M^2 - C_m^2)} \Bigg(& \left(\frac{s_2C_m - c_2S_m}{b} + 2mC_mS_mA^{-1}_{3,1} \right) B_1 \\
& + \left(\frac{-c_2C_m - s_2S_m}{b} + 2mC_mS_mA^{-1}_{3,2} \right) B_2 \\
& + \left(2mC_mS_mA^{-1}_{3,3} \right) B_3 + \left(\frac{S_mM_W}{b^2} + 2mC_mS_mA^{-1}_{3,4} \right) B_4 \Bigg)
\end{aligned}
\tag{A.22}
$$

$$\begin{aligned}\frac{\partial f_8}{\partial\theta_1} = \frac{\partial\mathbf{B}}{\partial\theta_1}\cdot\mathbf{A}^{-1}_{(4,:)} + \frac{1}{m(A_M^2 - C_m^2)}\Bigg(&\left(\frac{s_1C_m + c_1S_m}{b} - 2mC_mS_mA^{-1}_{4,1}\right)B_1\\ &+\left(\frac{-c_1C_m + s_1S_m}{b} - 2mC_mS_mA^{-1}_{4,2}\right)B_2\\ &+\left(-\frac{S_mM_W}{b^2} - 2mC_mS_mA^{-1}_{4,3}\right)B_3 + \left(-2mC_mS_mA^{-1}_{4,4}\right)B_4\Bigg)\end{aligned} \tag{A.23}$$

$$\begin{aligned}\frac{\partial f_8}{\partial\theta_2} = \frac{\partial\mathbf{B}}{\partial\theta_2}\cdot\mathbf{A}^{-1}_{(4,:)} + \frac{1}{m(A_M^2 - C_m^2)}\Bigg(&\left(\frac{s_2A_m - c_1S_m}{b} + 2mC_mS_mA^{-1}_{4,1}\right)B_1\\ &+\left(\frac{-c_2A_m - s_1S_m}{b} + 2mC_mS_mA^{-1}_{4,2}\right)B_2\\ &+\left(\frac{S_mM_W}{b^2} + 2mC_mS_mA^{-1}_{4,3}\right)B_3 + \left(2mC_mS_mA^{-1}_{4,4}\right)B_4\Bigg)\end{aligned} \tag{A.24}$$

The original mathematical model:

$$\frac{\partial f_{i+8}}{\partial q} = \frac{\partial\dot{x}_{c_i}}{\partial q}C_{f_i} \text{ for } q = [\theta_1, \dot{x}, \dot{\theta}_1] \tag{A.25}$$

$$\frac{\partial f_{i+8}}{\partial z_i} = -\sigma_0\frac{|\dot{x}_{c_i}|}{g(\dot{x}_{c_i})} \text{ for } i = 1, 2 \tag{A.26}$$

$$C_{f_i} = 1 - \frac{\sigma_0 z_i\dot{x}_{c_i}}{g(\dot{x}_{c_i})|\dot{x}_{c_i}|}\left(1 + \frac{2\dot{x}_{c_i}^2}{v_s^2}\left(1 - \frac{\mu_c}{g(\dot{x}_{c_i})}\right)\right) \tag{A.27}$$

The smooth approximation: (Outlined in section 4.2.2 on page 41)

$$\frac{\partial\tilde{f}_{i+8}}{\partial q} = \frac{\partial\dot{x}_{c_i}}{\partial q}\tilde{C}_{f_i} \text{ for } q = [\theta_1, \dot{x}, \dot{\theta}_1] \tag{A.28}$$

$$\frac{\partial\tilde{f}_{i+8}}{\partial z_i} = -\sigma_0\frac{S_v\dot{x}_{c_i}}{g(\dot{x}_{c_i})} \text{ for } i = 1, 2 \tag{A.29}$$

$$\begin{aligned}\tilde{C}_{f_i} = S_v^2 - \frac{\sigma_0 z_i S_v}{g(\dot{x}_{c_i})}&\left(1 + \frac{2\dot{x}_{c_i}^2}{v_s^2}\left(1 - \frac{\mu_c}{g(\dot{x}_{c_i})}\right)\right)\\ &+\frac{2}{\pi}\left(\frac{k_v\dot{x}_{c_i}}{1 + (k_v\dot{x}_{c_i})^2}\right)\left(2S_v - \frac{\sigma_0}{g(\dot{x}_{c_i})}z\right)\end{aligned} \tag{A.30}$$

$$S_v = \frac{2}{\pi}\arctan(k_v\dot{x}_{c_i}) \tag{A.31}$$

Where k_v is a tuning parameter. As $k_v \to \infty$ the function S_v approaches the signum function.

$$\frac{\partial \dot{x}_{c_i}}{\partial \theta_i} = \dot{\theta}_i \left(-l \sin\theta_i + \rho \sin\left(\theta_i - \delta\right)\right) \tag{A.32}$$

$$\frac{\partial \dot{x}_{c_i}}{\partial \dot{x}} = 1 \tag{A.33}$$

$$\frac{\partial \dot{x}_{c_i}}{\partial \dot{\theta}_i} = l \cos\theta_i - \rho \cos\left(\theta_i - \delta\right) + \rho \tag{A.34}$$

$$\frac{\partial F_{N_i}}{\partial y} = -\frac{3}{2}\sqrt{h_i}\left(k_s + k_d \dot{h}_i\right) \tag{A.35}$$

$$\begin{aligned}\frac{\partial F_{N_i}}{\partial \theta_i} = &-\frac{3}{2}\sqrt{h_i}\left(l \sin\theta_i - \rho \sin\left(\theta_i - \delta\right)\right)\left(k_s + k_d \dot{h}_i\right) \\ &- k_d h_i^{\frac{3}{2}} \dot{\theta}_i \left(l \cos\theta_i - \rho \cos\left(\theta_i - \delta\right)\right)\end{aligned} \tag{A.36}$$

$$\frac{\partial F_{N_i}}{\partial \dot{y}} = -k_d h_i^{\frac{3}{2}} \tag{A.37}$$

$$\frac{\partial F_{N_i}}{\partial \dot{\theta}_i} = -k_d h_i^{\frac{3}{2}} \left(l \sin\theta_i - \rho \sin\left(\theta_i - \delta\right)\right) \tag{A.38}$$

$$\frac{\partial F_{f_i}}{\partial q} = -\left(\sigma_0 z_i + \sigma_1 \dot{z}_i\right)\frac{\partial F_{N_i}}{\partial q} \text{ for } q = [y, \dot{y}] \tag{A.39}$$

$$\frac{\partial F_{f_i}}{\partial q} = -\sigma_1 \frac{\partial f_{8+i}}{\partial q} F_{N_i} - \left(\sigma_0 z_i + \sigma_1 \dot{z}_i\right)\frac{\partial F_{N_i}}{\partial q} \text{ for } q = [\theta_i, \dot{x}, \dot{\theta}_i, z_i] \tag{A.40}$$

$$\frac{\partial c_{x_i}^{hip}}{\partial \theta_i} = l \cos\theta_i - \rho \cos\left(\theta_i - \delta\right) \tag{A.41}$$

$$\frac{\partial c_{y_i}^{hip}}{\partial \theta_i} = -l \sin\theta_i + \rho \sin\left(\theta_i - \delta\right) \tag{A.42}$$

$$\frac{\partial \mathbf{B}(\mathbf{q})}{\partial y} = \begin{bmatrix} \frac{\partial F_{f_1}}{\partial y} + \frac{\partial F_{f_2}}{\partial y} \\ \frac{\partial F_{N_1}}{\partial y} + \frac{\partial F_{N_2}}{\partial y} \\ c_{y_1}^{hip}\frac{\partial F_{f_1}}{\partial y} + c_{x_1}^{hip}\frac{\partial F_{N_1}}{\partial y} \\ c_{y_2}^{hip}\frac{\partial F_{f_2}}{\partial y} + c_{x_2}^{hip}\frac{\partial F_{N_2}}{\partial y} \end{bmatrix}, \quad \frac{\partial \mathbf{B}(\mathbf{q})}{\partial z_1} = \begin{bmatrix} \frac{\partial F_{f_1}}{\partial z_1} \\ 0 \\ c_{y_1}^{hip}\frac{\partial F_{f_1}}{\partial z_1} \\ 0 \end{bmatrix}, \quad \frac{\partial \mathbf{B}(\mathbf{q})}{\partial z_2} = \begin{bmatrix} \frac{\partial F_{f_2}}{\partial z_2} \\ 0 \\ 0 \\ c_{y_2}^{hip}\frac{\partial F_{f_2}}{\partial z_2} \end{bmatrix} \tag{A.43}$$

$$\frac{\partial \mathbf{B}(\mathbf{q})}{\partial \theta_1} = \begin{bmatrix} \frac{\partial F_{f_1}}{\partial \theta_1} + mb\dot{\theta}_1^2 \cos\theta_1 \\ \frac{\partial F_{N_1}}{\partial \theta_1} + mb\dot{\theta}_1^2 \sin\theta_1 \\ c_{y_1}^{hip} \frac{\partial F_{f_1}}{\partial \theta_1} + c_{x_1}^{hip} \frac{\partial F_{N_1}}{\partial \theta_1} + \frac{\partial c_{y_1}^{hip}}{\partial \theta_1} F_{f_1} + \frac{\partial c_{x_1}^{hip}}{\partial \theta_1} F_{N_1} - mbg\cos(\theta_1 - \gamma) \\ 0 \end{bmatrix} \tag{A.44}$$

$$\frac{\partial \mathbf{B}(\mathbf{q})}{\partial \theta_2} = \begin{bmatrix} \frac{\partial F_{f_1}}{\partial \theta_2} + mb\dot{\theta}_2^2 \cos\theta_2 \\ \frac{\partial F_{N_2}}{\partial \theta_2} + mb\dot{\theta}_2^2 \sin\theta_2 \\ 0 \\ c_{y_2}^{hip} \frac{\partial F_{f_2}}{\partial \theta_2} + c_{x_2}^{hip} \frac{\partial F_{N_2}}{\partial \theta_2} + \frac{\partial c_{y_2}^{hip}}{\partial \theta_2} F_{f_2} + \frac{\partial c_{x_2}^{hip}}{\partial \theta_2} F_{N_2} - mbg\cos(\theta_2 - \gamma) \end{bmatrix} \tag{A.45}$$

$$\frac{\partial \mathbf{B}(\mathbf{q})}{\partial \dot{x}} = \begin{bmatrix} \frac{\partial F_{f_1}}{\partial \dot{x}} + \frac{\partial F_{f_2}}{\partial \dot{x}} \\ 0 \\ c_{y_1}^{hip} \frac{\partial F_{f_1}}{\partial \dot{x}} \\ c_{y_2}^{hip} \frac{\partial F_{f_2}}{\partial \dot{x}} \end{bmatrix}, \quad \frac{\partial \mathbf{B}(\mathbf{q})}{\partial \dot{y}} = \begin{bmatrix} \frac{\partial F_{f_1}}{\partial \dot{y}} + \frac{\partial F_{f_2}}{\partial \dot{y}} \\ \frac{\partial F_{N_1}}{\partial \dot{y}} + \frac{\partial F_{N_1}}{\partial \dot{y}} \\ c_{y_1}^{hip} \frac{\partial F_{f_1}}{\partial \dot{y}} + c_{x_1}^{hip} \frac{\partial F_{N_1}}{\partial \dot{y}} \\ c_{y_2}^{hip} \frac{\partial F_{f_2}}{\partial \dot{y}} + c_{x_2}^{hip} \frac{\partial F_{N_2}}{\partial \dot{y}} \end{bmatrix} \tag{A.46}$$

$$\frac{\partial \mathbf{B}(\mathbf{q})}{\partial \dot{\theta}_1} = \begin{bmatrix} \frac{\partial F_{f_1}}{\partial \dot{\theta}_1} + 2mb\dot{\theta}_1 s_1 \\ \frac{\partial F_{N_1}}{\partial \dot{\theta}_1} - 2mb\dot{\theta}_1 c_1 \\ c_{y_1}^{hip} \frac{\partial F_{f_1}}{\partial \dot{\theta}_1} + c_{x_1}^{hip} \frac{\partial F_{N_1}}{\partial \dot{\theta}_1} \\ 0 \end{bmatrix}, \quad \frac{\partial \mathbf{B}(\mathbf{q})}{\partial \dot{\theta}_2} = \begin{bmatrix} \frac{\partial F_{f_2}}{\partial \dot{\theta}_2} + 2mb\dot{\theta}_2 s_2 \\ \frac{\partial F_{N_2}}{\partial \dot{\theta}_2} - 2mb\dot{\theta}_2 c_2 \\ 0 \\ c_{y_2}^{hip} \frac{\partial F_{f_2}}{\partial \dot{\theta}_2} + c_{x_2}^{hip} \frac{\partial F_{N_2}}{\partial \dot{\theta}_2} \end{bmatrix} \tag{A.47}$$

A.3 Equilibrium Points

Unlike other mathematical models of passive dynamic walking, the model presented can come to an equilibrium. This equilibrium is when both feet are on the ground. Therefore, the swing leg ground clearance procedure, outlined in section 2.3.2 on page 21, would not be used. At an equilibrium all of the velocities are equal to zero and $x^* \in \mathbb{R}$. There are four equations, (A.48) to (A.51), that describe the remaining five unknown equilibrium points. Therefore, the equations can be described by $[\theta_1^*, \theta_2^*, z_1^*, z_2^*] = f(y^*)$, where $-l \leq y^* \leq l$.

$$\begin{gathered}\sigma_0 Q_9 k_s(-Q_2 + l\cos Q_3 + \rho(\cos(Q_3 - \delta) - 1))^n + \\ \sigma_0 Q_{10} k_s(-Q_2 + l\cos Q_4 + \rho(\cos(Q_4 - \delta) - 1))^n + mg(M_k + 2)\sin\gamma = 0\end{gathered} \tag{A.48}$$

$$\begin{gathered}k_s(-Q_2 + l\cos Q_3 + rho(\cos(Q_3 - \delta) - 1))^n + k_s(-Q_2 + l\cos Q_4 + \\ \rho(\cos(Q_4 - \delta) - 1))^n - mg(M_k + 2)\cos\gamma = 0\end{gathered} \tag{A.49}$$

$$\begin{gathered}k_s(-Q_2 + l\cos Q_3 + \rho(\cos(Q_3 - \delta) - 1))^n(\sigma_0 Q_9(l\cos Q_3 - \\ \rho(\cos(Q_3 - \delta) - 1)) + l\sin Q_3 + \rho\sin(-Q_3 + \delta)) - mgb\sin(Q_3 - \gamma) = 0\end{gathered} \tag{A.50}$$

$$\begin{gathered}k_s(-Q_2 + l\cos Q_4 + \rho(\cos Q_4 - \delta - 1))^n(\sigma_0 Q_{10}(l\cos Q_4 - \\ \rho(\cos(Q_4 - \delta) - 1)) + l\sin Q_4 + \rho\sin(-Q_4 + \delta)) - mgb\sin Q_4 - \gamma = 0\end{gathered} \tag{A.51}$$